Durham E-Theses

Thermal Alkali Vapour Spectroscopy: Buffer Gas Enhanced K Systems and Magneto-Optical Rb Applications

SHARAA AHMED S ALQARNI

How to cite:

Use policy

Thermal Alkali Vapour Spectroscopy:
Buffer Gas Enhanced K Systems and
Magneto-Optical Rb Applications

Sharaa Ahmed S Alqarni

A thesis presented for the degree of

Doctor of Philosophy

Department of Physics

Durham University

United Kingdom

November 3, 2025

Thermal Alkali Vapour Spectroscopy:
Buffer Gas Enhanced K Systems and Magneto-Optical Rb Applications

Sharaa Ahmed S Alqarni

Abstract

We present experimental and theoretical work on atomic bandpass filters and spectroscopic characterisations of alkali vapour systems for magneto-optical applications. We demonstrate a new method for generating arbitrary angle magnetic fields in atomic filters using Rb vapour. This involves a fixed of permanent magnets in a Voigt geometry combined with a solenoid. We compare this method with the previously used method of rotating the permanent magnet pair. This setup offers more precise and flexible angle control. While both methods generate similar transmission profiles, the new setup allows larger angles and supports longer vapour cells, enhancing magneto-optical filters. Next, we investigate K D1 transition in the presence of neon buffer gas, in particular the pressure induced broadening and frequency shift, and the Zeeman splitting in the hyperfine Paschen-Back (HPB) regime. We use dual-control temperature systems to independently adjust Doppler and collisional effects, and we achieve excellent agreement with literature values for potassium-neon collisions. For the first time, buffer gas effects integrate into our theoretical model ElecSus, producing accurate prediction of modified Voigt profiles. We conduct a comprehensive experimental and theoretical study into the Stokes polarimetry of potassium atomic vapour with neon buffer gas, focusing on the temperature and magnetic field effects. This work represents the first application of ElecSus to model the buffer gas polarimetry of K D1 transitions. This study provides new insights into the effects of buffer gases on Stokes parameters, and indicates advances in a theoretical framework for understanding atom-light interactions in buffer gas environments.

Supervisors: Ifan G. Hughes and Steven A. Wrathmall

Acknowledgements

First and foremost, I would like to give special thanks to my supervisor, Ifan, for being extremely helpful, supportive, and encouraging throughout my research journey. He has been excellent supervisor in every sense. I am lucky to have had the opportunity of working under his supervision. I would also like to thank Steven for considerable assistance he provided as my second supervisor.

Special thanks to Dani, who had given as much time as she could to help me teach all that I needed to do in the lab and who could explain complex things in simple terms. She was the first person who would come into consideration whenever I had something to ask advice on, either the lab work or life issues. I greatly value her advice because she would give me only what is good for me, and I am also grateful for her proofreading. I would also like to thank Fraser, Clare, and Jack for providing help throughout my PhD.

There are simply no words to express how thankful I am to my parents, who have been the best role models and have shown unwavering faith in me since I was a child. Your continuous support and encouragement have been fundamental to my success.

Thanks a lot to my brothers and sisters who have remained a source of strength and encouragement throughout. You always called me Dr.Sharaa until I did my best to make your dream come true.

I am extremely grateful to my husband. Special thanks for your unwavering support, for being a great source of motivation, and for being a great dad to our son. Your ambitions have never failed to inspire me never to give up and continue to pursue my dreams regardless of the challenges.

My endless thanks to my son, Nawaf, for his unlimited tolerance and patience during my PhD. You don't have to ask anymore when we are going back home or when you remind me of how you miss your friends there.

I would also like to thank my friends who supported me along. Your kindness and motivation have counted more than you can imagine.

Finally, I would like to acknowledge the Saudi Arabian Cultural Bureau in the United Kingdom, and Najran University for providing me with a full scholarship.

Contents

Declaration

The work in this thesis is based on research carried out at the Department of Physics, University of Durham, England. No part of this thesis has been submitted elsewhere for any other degree or qualification, and it is the sole work of the author unless referenced to the contrary in the text.

Publications

Sharaa A. Alqarni, Jack D. Briscoe, Clare R. Higgins, Fraser D. Logue, Danielle Pizzey, Thomas G. Robertson-Brown, and Ifan G. Hughes. "A device for magnetic-field angle control in magneto-optical filters using a solenoid-permanent magnet pair", *Review of Scientific Instruments*, **95**, no. 3 (2024). https://doi.org/10.1063/5.0174264 [1]

Sharaa A. Alqarni, Danielle Pizzey, Steven A. Wrathmall, and Ifan G. Hughes. "The Role of Buffer Gas in Shaping the D1 Line Spectrum of Potassium Vapour" *Journal of Physics B: Atomic, Molecular and Optical Physics*, 58, (2025). https://doi.org/10.1088/1361-6455/adea01 [2]

Sharaa A. Alqarni, Danielle Pizzey, Steven A. Wrathmall, and Ifan G. Hughes. "Experimental and theoretical characterisation of Stokes polarimetry of the potassium D1 line with neon buffer gas broadening". *arXiv Preprint*, 2507.18353, (2025). https://doi.org/10.48550/arXiv.2507.18353 [3]

List of Figures

List of Tables

CHAPTER 1

Introduction

1.1   Alkali metal thermal vapours

Alkali metals, positioned in Group 1 of the periodic table, have been of significant interest due to their physical and chemical properties. They exist in metallic form at room temperature, and can be stored in glass vacuum cells, which we heat to transfer some atoms to the vapour form. In addition, the atomic vapour pressure of these elements inside the cells is significant at room temperature, and increases exponentially with temperature, allowing an optically-dense medium to be achieved with relative ease [4]. This makes dealing with thermal vapours considerably simpler compared to working with cold atoms, which need a vacuum chamber setup and complicated laser systems for cooling and trapping atoms. As such, these alkali-metal atoms have been widely utilised in fundamental and experimental research, including studies on electromagnetically induced transparency [5], nonlinear and quantum optics [6, 7], a quantum memory for light [8, 9], orbital angular momentum transfer [10, 11], and coherent frequency up-conversion [12]. Thermal vapours have also been used for a wide range of applications, including spectroscopy [13, 14], magnetometry [15, 16], terahertz imaging [17], narrowband optical filters [13, 18], and solar filters [19].

While thermal vapours are convenient for experiments, they may also present some challenges. The thermal motion introduces a velocity distribution for the atoms, leading to Doppler broadening of absorption lines, which typically exceed the hyperfine splitting of the energy levels. This makes it harder to model the system theoretically and resolve spectral features clearly. In addition, collisions between the atoms and cell walls can also lead to changes in the spectral lines [20, 21] and other features of the vapour [22, 23]. However, these challenges can be addressed using techniques like optical pumping, where a strong circularly polarised laser field is applied to the vapour, causing all the atoms to transition into a single dark state that does not interact with the light [24]. Collisions can also be partially managed using anti-relaxation coating cells [25] and the presence of buffer gases in the cell [26] as demonstrated in Chapter 5. Another solution to deal with these effects is to apply a large magnetic field, as we will discuss later in this chapter and demonstrate in the rest of this thesis, to generate additional shifts in the atomic energy levels, improving the resolution of the spectral lines [27, 28, 29].

1.2 Large magnetic field

The spectroscopic investigation of atomic vapours in an external magnetic field is well understood. Quantitative theoretical modeling of linear atom-light interactions in magnetic fields [30, 31] has led in recent years to significant developments in fundamental physics, such as quantum nonlinear optics effects [32], as well as to novel technologies, including miniature optical isolators [33], narrowband atomic filters [34], and self-stabilised diode lasers [35].

When a magnetic field is applied to atoms, it leads to changes in the energy levels of their states, thus influencing the frequency of light required for inducing transitions among these states, to shift [31]. This change in energy caused by the magnetic field is known as the Zeeman shift. By applying a large magnetic field to our atoms, we may use this effect to solve the problem of exciting many closely spaced transitions simultaneously. At high field strengths, interaction between the magnetic field and

atoms causes nuclear and electronic spins to decouple, thus entering the hyperfine Paschen-Back (HPB) regime [4, 36]. This will be discussed in detail in Section 2.6. Under such conditions, methods like absorption spectroscopy and Stokes polarimetry [37] have been found to be effective in retrieving information about the effect of the magnetic field, as the large Zeeman shifts produce characteristic spectroscopic features such as greater symmetry [38, 39].

All potassium experiments described in this thesis are carried out in 700 G or higher. At these large fields, K enters the hyperfine Paschen-Back regime, where the Zeeman shifts exceed the natural hyperfine splittings. This ensures that the individual magnetic transitions are well resolved and identifiable, even though there is Doppler broadening in thermal vapours. Measurement of Stokes parameters [37] in this regime provides a useful tool to examine both the strength of the magnetic field and the overall atomic response under these extreme conditions, as will be discussed in detail in Chapter 6 of this thesis.

1.3   Faraday effect

In 1846, Michael Faraday observed that the plane of polarisation of light rotates as it passes through different media under the influence of an axial magnetic field [40]. This was the initial magneto-optic phenomenon found, demonstrating the interrelation between light, magnetism, and electricity.

The Faraday effect is widely used to control light, particularly in quantum optics research [41, 42, 43, 44]. Common uses of these applications are magnetometry [16, 45], laser frequency stabilisation [46], and optical isolators [33, 47].

The Faraday effect has been studied in many regimes. When the frequency of light is near the atomic resonance, the resonant Faraday effect occurs. When light is detuned far from the atomic resonance, it is known as the off-resonant Faraday effect [48]. Nevertheless, these two phenomena are frequently only examined in weak magnetic fields, where the line-broadening is greater than the Zeeman shift.

In Chapter 5, the Faraday effect is studied in the hyperfine Paschen-Back regime, where for K the Zeeman shift is much larger than the atomic line-broadening.

1.4 Applications in Solar Filtering and Magneto -Optical Devices

Large magnetic field applications extend well beyond fundamental atomic physics into practical devices. Solar filters based on the Faraday effect in thermal vapours can provide extremely narrow-band filtering with high rejection ratios, enabling precise observations of specific solar emission lines while rejecting the broadband solar continuum [19, 49, 50, 51, 52, 53, 54, 55]. These capabilities are particularly useful when observing continuous synoptic monitoring of solar oscillations, solar magnetic activity, and space weather relevant phenomena. Several number of parameters, including atomic species, vapour density, magnetic field strength and orientation, cell geometry, and optical design must be carefully optimised in order to create application-specific magneto-optical filters (MOFs) [56], rather than aiming for a single "ideal" filter design.

The method used in this work recognises that the best filter is application-specific and optimised for specific requirements such as bandwidth, transmission, field of view, or thermal stability [57]. For example, sodium has been used in resonance scattering solar spectroscopy applications [49], where potassium has been used extensively in the Birmingham Solar Oscillations Network (BiSON) and more recently robotic synoptic telescopes such as TSST and SAMM [50, 51, 52, 53, 54].

This work contributes directly to this effort by quantifying the impact of buffer gas on the potassium vapour line shapes.

The Precise measurements of the pressure-broadening and pressure-shift of the D1 line allow for an improved understanding of potassium-based filters, especially under the influence of changing temperature and pressure conditions. This is essential as the filter passband stability and transmission profile are dependent upon

the collisional nature of the alkali atoms and the buffer gas. The comparison of experimental data with theoretical modelling, illustrated in this thesis, details useful benchmark parameters that can be incorporated into future designs of MOFs, that can be used for optimised monitoring of solar phenomena.

In addition, the work on magneto-optical effects including arbitrary-field angles, presents a new methodology to modify the filter's response. This advances beyond the standard Faraday and Voigt geometries enabling a design that customises passbands for specific observational goals. Altogether, improving the functionality of alkali-metal optical filters for solar applications is essential so that the instruments in this next generation can achieve the stability, selectivity and robust design that is desired for continuous space-weather monitoring and solar oscillation studies.

1.5   Aim of this thesis

The aim of this thesis is to investigate the fundamental interactions of alkali atoms with buffer gases in controlled magnetic fields, achieved by three linked studies that advance both experimental techniques and theoretical understanding relevant to applications in precision spectroscopy and polarimetry. We present and validate a new method for creating magnetic fields at arbitrary angles through a solenoid-permanent magnet configuration. This new method allows for fast and precise adjustment of the magnetic field direction by changing the solenoid current and is more convenient and flexible than conventional techniques based on physical magnet rotation, while maintaining similar transmission properties.

We also provide a detailed experimental characterisation of buffer gas influence on the potassium D1 spectral line in the hyperfine Paschen-Back (HPB) regime. The examination investigates how buffer gas pressure and temperature affect spectral line broadening, shifting, and the overall structure of the spectrum, as well as investigating of the effects of magnetic fields on polarisation-dependent Zeeman splitting in these systems.

We also conduct comprehensive experimental and theoretical studies of Stokes polarimetry in dense potassium vapour for the D1 transition operating in the HPB regime. The research studies the effect of neon buffer gas on the polarisation properties under strong magnetic field influence using Faraday geometry and comparing the experimental results with theoretical predictions produced by *ElecSus* software. Importantly, this work represents the first application of *ElecSus* to buffer gas polarimetry for potassium D1. This theoretical framework is expected to provide new insights into collisional effects on atomic coherences and enable better predictions for polarisation dynamics in practical systems. Through these three complementary studies, this work bridges the gap between the fundamental principles of atomic physics and practical applications in magneto-optical systems, thus advancing precision measurement techniques relevant to solar filters, atomic magnetometry, and other quantum optics technologies requiring precise control of atomic vapour properties.

1.6 Thesis summary

Chapter 2 provides some of the theory relevant to the whole thesis. It shows how spectral line shapes are affected by the presence or absence of buffer gas, and introduces a collisional model based on *ElecSus* for simulating these effects, especially between potassium atoms and neon as a buffer gas. We discuss the atomic structure of rubidium and potassium atoms, which are the atoms of choice for the experiments in this thesis. The chapter also introduces the hyperfine Paschen–Back regime, which we reach by application of a large magnetic field, Stokes polarimetry, and the principles behind magneto-optical filters used in precision measurements.

Chapter 3 outlines specific experimental details relevant to the whole of the thesis, including the description of the vapour cells and magnets used, and explains laser calibration method.

Chapter 4 is based on the publication [1] and presents a new method for generating

magnetic fields at arbitrary angles using a solenoid-permanent magnet pair. This setup allows for fast and precise tuning of the magnetic field direction by adjusting the solenoid current. Experimental confirmation is obtained from Hall probe and filter transmission measurements. We compare our method to the older method of physically rotating magnets, and show how our approach offers similar transmission profiles with improved ease and flexibility.

Chapter 5 is based on the publication [2] and provides a detailed experimental study on the influence of buffer gas on the potassium D1 spectral line. The results detail how buffer gas pressure, and temperature impact broadening and shifting of spectral lines as well as the shape of the spectrum. Further analysis demonstrates the effect of magnetic fields on the spectral lines, such as polarisation-dependent Zeeman splitting.

Chapter 6 is based on the work [3] and provides both experimental and theoretical studies of Stokes polarimetry performed in dense potassium vapour for the D1 transition. The investigation shows the impact of neon buffer gas on polarisation properties under the influence of magnetic fields, using Faraday geometry for analysis. The experimental results for absorption and dispersion are compared with theoretical models produced by *ElecSus* software, marking the first application of *ElecSus* to buffer gas polarimetry for potassium D1. The results provide new insights into buffer gas collision effects on atomic coherence and polarisation, thus providing better theoretical understanding of atom-light interactions in buffer-gas environments.

Chapter 7 concludes the thesis, and presents some thoughts on further related study.

CHAPTER 2

Theory

2.1 Atomic structure of an alkali metal

This section provides a brief discussion of the electronic structure of rubidium and potassium atoms, which is important for understanding the experiments in this thesis. Rubidium (Rb) and potassium (K) are alkali metals that belong to Group I of the periodic table, with one valence electron in their outer shell.

2.1.1 Atomic structure of rubidium

Rubidium, with atomic number $Z = 37$, has a ground state electronic configuration of 5s. It has two naturally occurring isotopes: 28% ^{87}Rb, and 72% ^{85}Rb [27]. Figure 2.1 is a schematic diagram of ^{87}Rb and ^{85}Rb energy level structure. The fine structure splitting is determined by spin-orbit coupling, which is the interaction between the electron orbital angular momentum $\vec{L}$, and the electron spin $\vec{S}$ which is always 1/2 for atoms with one valence electron. These energy eigenstates have spin-orbital angular momentum $\vec{J} = \vec{L} + \vec{S}$, and are easily identified by the quantum number J, and m_{J} ,which represents the projection of onto the quantisation axis defined by a magnetic field.

The electron's spin-orbit angular momentum, $\vec{J}$, further interacts with the atom's

---
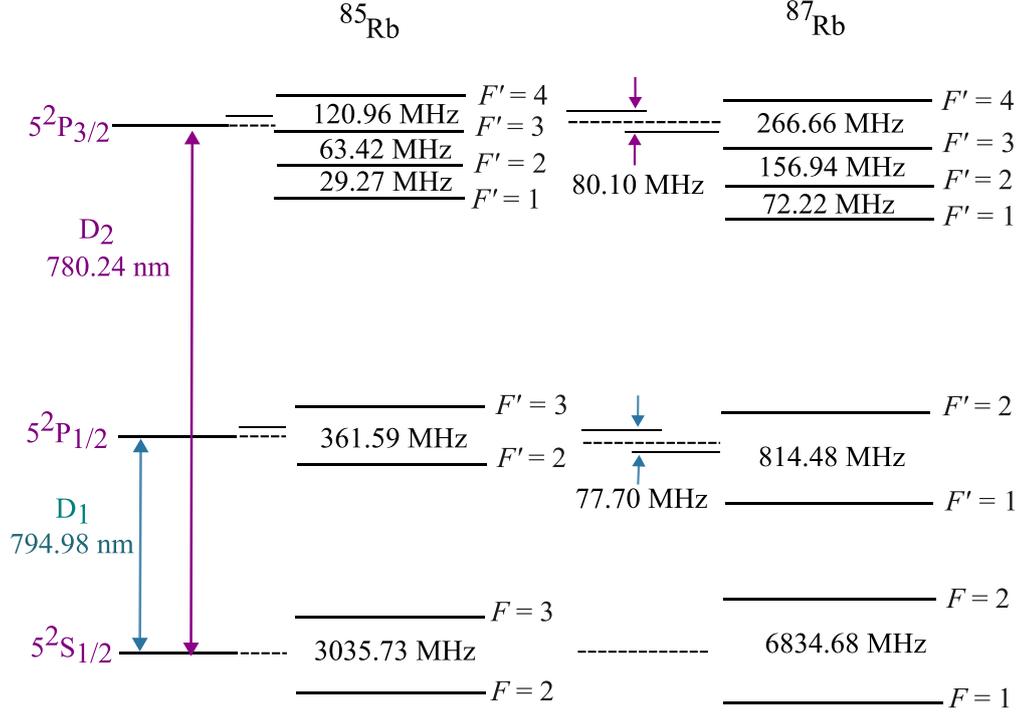
Figure 2.1: The hyperfine structure and intervals of [85]Rb and [87]Rb for the D1 ($5^2S_{1/2} \rightarrow 5^2P_{1/2}$) and D2 ($5^2S_{1/2} \rightarrow 5^2P_{3/2}$). Data taken from [27].

nuclear spin, $\vec{I}$, leading to hyperfine structure splitting. The energy eigenstates have total angular momenta $\vec{F} = \vec{J} + \vec{I}$, and the good quantum numbers now are $F = \vec{F}$, and the projection of $\vec{F}$ onto the quantisation axis, m_{F}. The atomic structure can be accurately characterised by this formulation in the absence of the magnetic field and in the presence of a small external magnetic field B. In a strong magnetic field, as will be described in section 2.6, we enter the hyperfine Paschen-Back regime, where the values of m_{J} and m_{I} become reliable quantum numbers.

2.1.2 Unique properties of potassium

Potassium, with atomic number $Z = 19$, has a ground state electronic configuration of 4s. It has three naturally occurring isotopes: [39]K, [40]K, and [41]K and the relative abundance of these isotopes in nature is 93.1%, 0.01%, and 6.9%, respectively. This
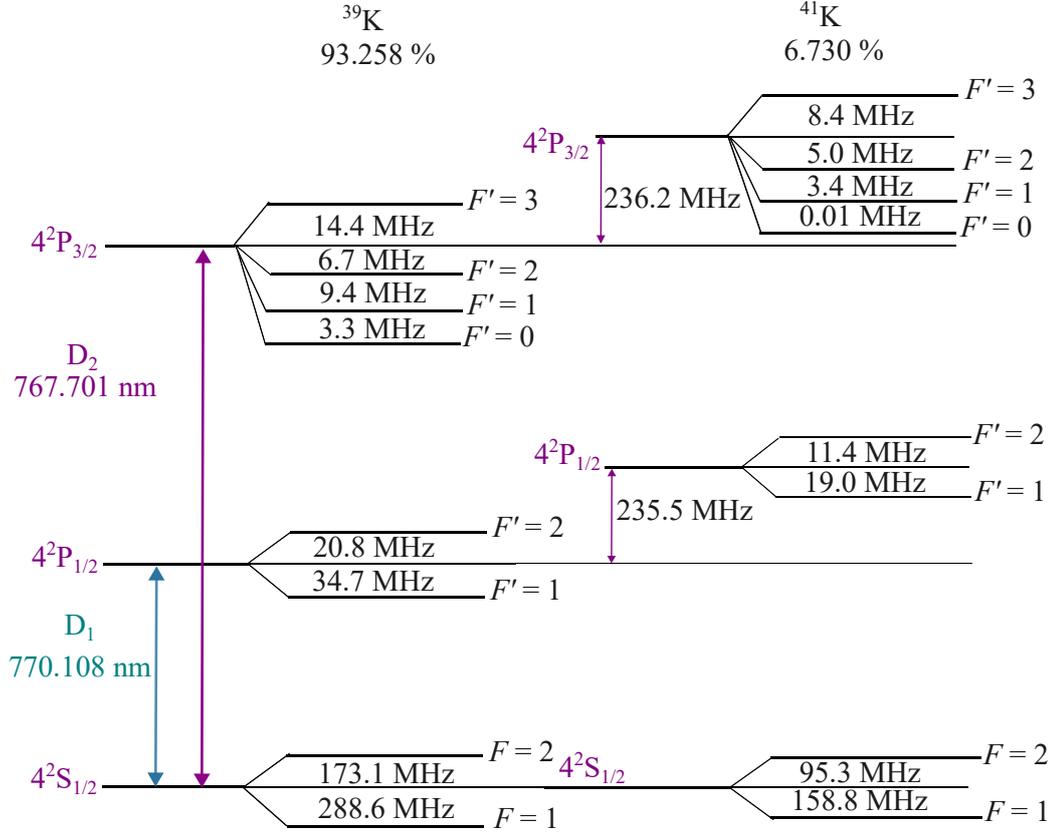
Figure 2.2: The hyperfine structure and intervals of ^{39}K, ^{41}K. We have neglected ^{40}K due to its natural abundance of 0.01%. Data taken from [58, 59, 60, 61, 62].

means that ^{39}K is the most abundant isotope in nature with nuclear spin $I = 3/2$. Figure 2.2 is a schematic diagram of ^{39}K and ^{41}K energy level structure; we have ignored ^{40}K due to the fact that it has a natural abundance of 0.01%.

K atoms have features which make them different from other alkali atoms. Notably, the ground state hyperfine splitting is smaller than the Doppler width. To achieve measurable absorption of the probe beam with a good signal-to-noise ratio, the potassium vapour cell was heated to approximately 313 K. At this temperature, there is a sufficient density of atomic vapour to absorb a significant portion of the incident beam. At 313 K, the Doppler width is ≈ 0.8 GHz, which is substantially larger than the ground state hyperfine splitting of the potassium isotopes, as illustrated in Figure 2.2. As a result, one would expect to observe a single Doppler-broadened transmission spectrum for each of the D lines, with contributions from
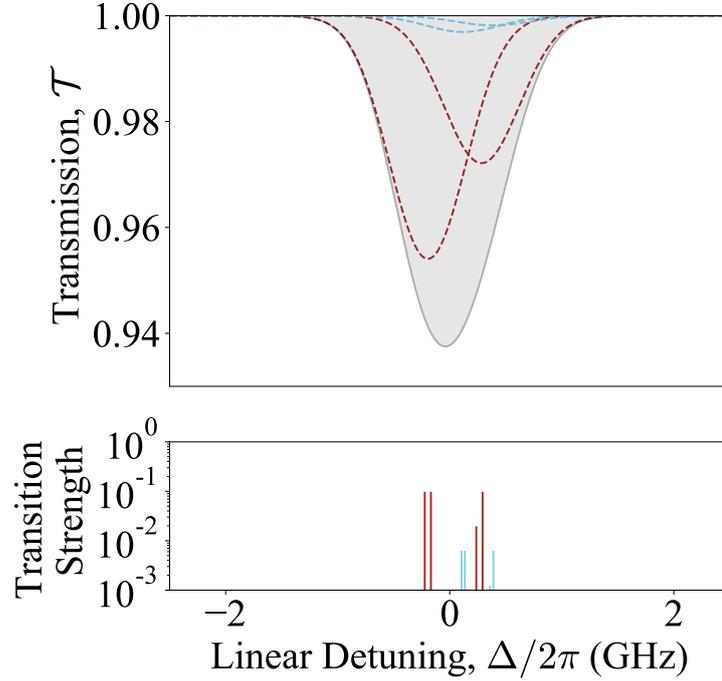
Figure 2.3: Plot illustrates the calculated contributions to the overall transmission spectrum of a probe beam resonant with the D1 transitions as it passes through a 25 mm potassium vapour cell at natural abundance. The blue (dashed) spectra represent transitions from $F = 1 \to F'$ and $F = 2 \to F'$ for ^{41}K. The red (dashed) spectra represent transitions from $F = 1 \to F'$ and $F = 2 \to F'$ for ^{39}K. The thick black line represents the total transmission spectrum. The different F transitions all overlap and we get the black curve which is total transmission spectrum. The plot below displays the transition strengths, weighted by isotopic abundance, with the blue and red lines corresponding to ^{41}K and ^{39}K, respectively. The linear detuning ($\Delta/2\pi$) is referenced to the weighted centre of the line.

both ground states, as shown in Figure 2.3 [63].

Rubidium D2 (780 nm) and potassium D1 (770 nm) are comparable in wavelength; however, ^{39}K is lighter than both isotopes of Rb, which has a mass number of 85 and 87. This means K atoms move faster than Rb at the same temperature, hence causes the Doppler width of K to increase by a factor of $\sqrt{2}$, as derived from Eqn. 2.12.
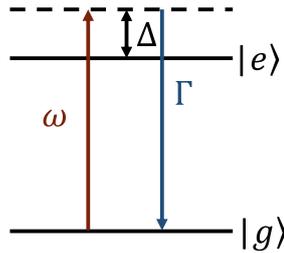
Figure 2.4: Schematic of the 2-level atom interacting with an incident optical field. The ground ($|g\rangle$) and excited ($|e\rangle$) states are coupled by an optical field with angular frequency ω detuned from the atomic resonance by Δ. Spontaneous decay from the excited state happens at rate Γ.

2.2 Atom light interactions

The primary focus of this thesis is the study of atom–light interactions. In this section, we will provide a brief overview of the semi-classical model we employ to characterise these interactions, as well as apply it to a two-level atom. More detailed descriptions are available in other sources, e.g. [64]. The energy level diagram for the interaction between a coherent light field and a hypothetical two level atom is shown in Figure 2.4. Each atom has ground state ($|g\rangle$) and excited state ($|e\rangle$), with an energy gap $= \hbar\omega_0$, where ω_0 is the resonant frequency of the transition. The light has an angular frequency, ω, which can be detuned from the resonant frequency by $\Delta = \omega - \omega_0$. The excited state decays spontaneously with a rate $\Gamma = 1/\tau$, where τ is the lifetime of the excited state, and the atom can only return to the ground state. The state of the atoms is characterised using a density matrix formalism [65]

$$\hat{\rho} = \begin{pmatrix} \rho_{\mathrm{gg}} & \rho_{\mathrm{ge}} \\ \rho_{\mathrm{eg}} & \rho_{\mathrm{ee}} \end{pmatrix}, \tag{2.1}$$

where the diagonal elements ρ_{gg} and ρ_{ee} denote the populations in the ground and excited states, respectively, while the off-diagonal elements represent the coherent combinations of states g and e.

Consider the optical field as an incident plane wave that comes in along the z direc-

tion with frequency ω, and electric field $\vec{E} = \hat{\mathbf{e}} E_0 \cos{(kz - \omega t)}$, where $k = 2\pi/\lambda$ is the wavenumber, $\hat{\mathbf{e}}$ is the polarisation vector, E_0 the amplitude of the electric field, and t is time. Because the spatial extent of atomic wavefunctions is significantly smaller than the wavelength of light, we can apply the dipole approximation [66], and simplify the electric field expression as:

$$\vec{E} = \hat{\mathbf{e}} E_0 \cos{\omega t} = \hat{\mathbf{e}} E_0 \frac{(\mathrm{e}^{i\omega t} + \mathrm{e}^{-i\omega t})}{2}. \tag{2.2}$$

In the dipole approximation, the interaction Hamiltonian is expressed as:

$$\hat{H}_{\mathrm{int}} = -\hat{d}.\vec{E}, \tag{2.3}$$

where $\hat{d} = \mathrm{e}\hat{\mathbf{r}}$ is the dipole operator, e is the electron charge while $\hat{\mathbf{r}}$ is the displacement vector. The dipole operator consists of off-diagonal elements only where the diagonal elements are zero as a result of the parity of the states.

The time evolution of the density matrix is discribed by the von Neumann equation [65]

$$\frac{d\hat{\rho}}{dt} = -\frac{i}{\hbar}[\hat{H}, \hat{\rho}], \tag{2.4}$$

where $\hat{H}$ is the total Hamiltonian. Using well-established procedures for atom-light interactions [32, 67], we arrive at the well-known atom-light interaction model, which includes the electric field and spontaneous emission processes. This forms the foundation of the *ElecSus* theoretical model.

2.3 Absorption spectra

In the laboratory, we characterise the interaction between atoms and light using atomic spectroscopy, where we measure the transmission of a laser beam through an atomic medium. To model these spectra, we need to relate the macroscopic polarisation of the medium to the individual electric dipole moments of the atoms [67].

For an ensemble, we take the average dipole moment and obtain the overall polarisation [68]. This relationship is expressed through the coherences of our density matrix, which connect the microscopic properties of the atoms to the macroscopic behavior of the medium as following:

$$\vec{P} = N\langle\hat{d}\rangle = \mathrm{Tr}[\hat{\rho}\hat{d}]N = N(\vec{d}_{\mathrm{ge}}\rho_{\mathrm{eg}}e^{-i\omega t} + \mathrm{c.c.}), \tag{2.5}$$

where P is the polarisation, N the number density of dipoles, $\langle\hat{d}\rangle$ the average dipole moment and c.c. the complex conjugate. The polarisation of the macroscopic medium can also be written as [68]:

$$\vec{P} = \epsilon_0\chi(\omega)\vec{E} = \frac{1}{2}\epsilon_0\chi\vec{E}(\chi e^{-i\omega t} + \mathrm{c.c.}), \tag{2.6}$$

where $\chi(\omega)$ is the electric susceptibility of the medium which is a quantity with complex value dependent on the frequency and ϵ_0 is the vacuum permittivity.

The susceptibility, which characterises how the vapour responds to the electric field, can be described in terms of ρ_{eg} using equations 2.5 and 2.6 as:

$$\chi(\omega) = -\frac{2d_{\mathrm{ge}}^2}{\epsilon_0\hbar\Omega^*}N\rho_{\mathrm{eg}}. \tag{2.7}$$

The refractive index of the medium, denoted as n, is determined by $n = \sqrt{1 + \chi}$. In our systems, where $|\chi| \ll 1$, this can be approximated as $n \approx 1 + \chi/2$. The refractive index is complex, $n = n_{\mathrm{R}} + in_{\mathrm{I}}$, where the real part describes the dispersive properties of the medium while the imaginary part describes the absorptive properties of the medium using the Beer-Lambert law [4]:

$$I = I_0 e^{-l\alpha}, \tag{2.8}$$

where I is the intensity of the output, I_0 is the incident intensity of light, l is the length of the medium, and α is the absorption coefficient which is directly proportional to the imaginary part of the refractive index $2kn_I$.

The equations enable us to compute the absorption of the medium for a specific driving frequency. We compute the absorption across a range of driving frequencies in order to construct a spectrum similar to what would be observed in an experiment.

2.4 Profiles of Spectral Lines

In this section, we discuss the transmission profiles through the atomic medium, in particular potassium, in the absence and presence of a buffer gas medium.

2.4.1 Profile without Buffer Gas

In the weak excitation limit [24], the steady-state solution is expressed as [67]

$$\lim_{\Omega \to 0} \frac{\rho_{\text{eg}}}{\Omega} = \frac{1}{2\Delta + i\Gamma_0}.$$ (2.9)

The macroscopic polarisation, and therefore the electric susceptibility is proportional to ρ_{eg}. The absorption coefficient is determined from the imaginary part of $\chi(\omega)$, which yields the characteristic Lorentzian lineshape:

$$\alpha(\Delta) \propto \frac{\Gamma}{4\Delta^2 + \Gamma^2}$$ (2.10)

Up to this point, we have discussed the interaction between light and stationary atoms. However, the experiments in this thesis involve a thermal atomic vapour. Since the atomic velocities are distributed in all directions, their motion can be described by a Maxwell-Boltzmann distribution. This motion causes a Doppler shift in the frequency of the light absorbed by the atoms.

$$\Delta_D = -\mathbf{k} \cdot \mathbf{v} = -k \, v_z,$$ (2.11)

where $\mathbf{k}$ is the wavevector of the incident laser beam, which is assumed to be aligned with the z-axis. It is evident from this relation that a frequency shift occurs only when there is a component of the atom's velocity along the z-axis. The velocity

distribution $f(v_z)$ along this axis follows a Gaussian distribution [69], given by

$$f(v_z) = \frac{e^{-v_z^2/u^2}}{u\sqrt{\pi}}, \tag{2.12}$$

where the quantity $u = \sqrt{2k_{\mathrm{B}}T/m_a}$ defines the width of the distribution, k_{B} is the Boltzmann constant, T the temperature of the vapour, and m the mass of an atom.

The overall susceptibility of the medium is determined by summing the contributions from all velocities, each weighted by $f(v_z)$. Due to the Doppler shift, moving atoms return to resonance and thus absorb the light. The resonance condition is met when $\Delta + kv = 0$. This results in an inhomogeneous broadening of the absorption line, characterised by a Doppler width $w_{\mathrm{D}} = ku$, is approximately 600 MHz for the Rb D2 line and 800 MHz for the K D1 line at T= 373 K [4]. For hot atoms, this Doppler width is significantly larger than the natural linewidth, which is around 6 MHz for both the Rb D2 [70], and K D1 lines [71]. In this case, the lineshape is represented by a Voigt function [4], which approximates a Gaussian profile at low detunings ($\Delta \ll w_{\mathrm{D}}$) and a Lorentzian profile at high detunings ($\Delta \gg w_{\mathrm{D}}$) [72].

The Lorentzian part of the spectral lineshape has a width, Γ, which comes from a combination of different broadening effects. This total linewidth can be written as:

$$\Gamma = \Gamma_0 + \Gamma_{\mathrm{c}}. \tag{2.13}$$

Here, Γ_0 is the natural linewidth, set by the rate of spontaneous emission, while Γ_{c} accounts for extra broadening caused by collisions between atoms in different energy states. The value of Γ_c increases linearly with the atomic number density N, as noted in reference [73]. We will discuss how N depends on temperature later in the chapter. In this investigation, we employ cells both with and without buffer gas, allowing us to study collisional broadening effects in effects across different regimes. The collisional broadening Γ_{c} can range from essentially zero (in cells without buffer gas) to around 800 MHz, depending on temperature and buffer gas pressure. This will be discussed in more detail in Chapter 5.
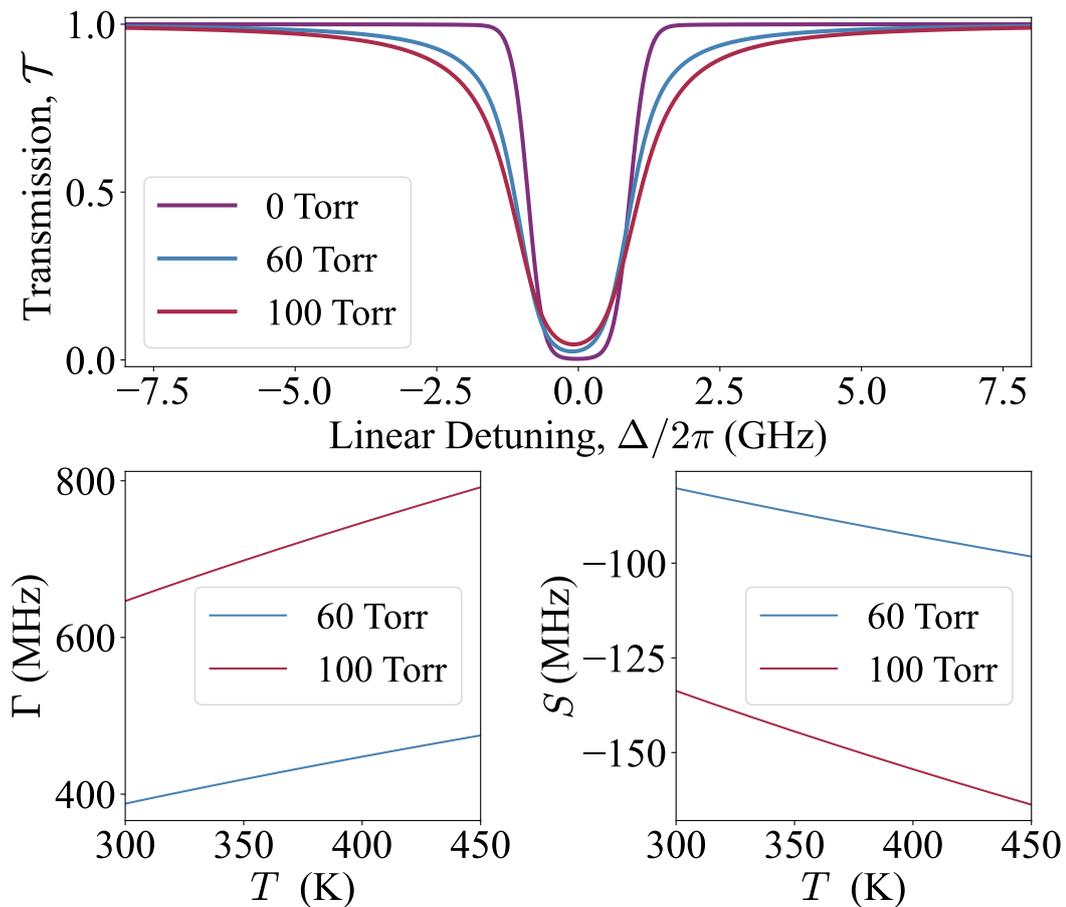
Figure 2.5: Theoretical predictions for the potassium D1 line, passing through a 75 mm natural-abundant vapour cell. The purple, blue and red spectra correspond to the vapour cell with no buffer gas, 60 Torr, 100 Torr of neon respectively which is what we will use in Chapter 5, at $T = 363$ K. The lower plots display how the buffer gas broadening (left panel) and spectral shift (right panel) depends on temperature.

2.4.2 Profile with Buffer Gas

Adding buffer gas to the vapour cell induces significant changes to the spectral profile of alkali atoms, which is why we need to study their effects in detail when introducing them into experiments. This is particularly relevant for applications such as solar filters [50, 51, 52, 53, 54] and magnetometers [74, 75], where buffer gases are commonly incorporated.

2.4.3 Collisional Model for Buffer Gas Effects in *ElecSus*

Adding buffer gas to the vapour cell lead to frequent collisions between alkali atoms and noble gases, shorten the effective lifetime of an excited state, pressure broadening, and a shift in the central frequency of the spectral line. Prior to our study [2], *ElecSus* accurately simulated Doppler and natural broadening mechanisms, as well as magnetic field effects, but it did not consider buffer gas effects [31, 76, 77, 78]. We have implemented a collisional model for buffer gases into *ElecSus* which allows for accurate simulations of pressure broadening and shift of the potassium D1 line. The effect of including neon buffer gas is especially crucial from the perspective of tuning the filter's spectral profile via control of these broadening and shifting effects. We specifically refer to neon here as it is the buffer gas used in our experimental studies described in Chapters 5 and 6.

According to the theory of collisional broadening, collisional effects are temperature-dependent [79, 80, 81, 82]. Hence, the gas broadening γ_j and shift rates δ_j as a function of temperature T and can be derived with the following equations:

$$\gamma_j = \gamma_r \left(\frac{T_r}{T_j}\right)^{\eta} \tag{2.14}$$

and

$$\delta_j = \delta_r \left(\frac{T_r}{T_j}\right)^{\eta}, \tag{2.15}$$

where γ_r and δ_r are the gas broadening and shift rates at a reference temperature T_r, and η is the temperature-dependent coefficient. For potassium D1 with neon at $T_r = 328$ K, the values of γ_r and δ_r are 6.14 and -1.27 MHz/Torr, respectively [80]. According to [79, 80, 83], the theoretical value for η is projected to be 0.5 for neon.

To relate this to the pressure inside the cell, we use the ideal gas law. The pressure P_j at any temperature T_j is:

$$P_j = P_i \left(\frac{T_j}{T_i}\right), \tag{2.16}$$

where P_i is the initial fill pressure at an initial temperature of $T_i = 298$ K, since the cells were filled at room temperature.

Using the temperature dependence stated in Eqn. 2.16, we can express the gas broadening, Γ_j, and the shift, S_j, as functions of the buffer gas pressure, P_j:

$$\Gamma_j = \gamma_j P_j \tag{2.17}$$

and

$$S_j = \delta_j P_j \ , \tag{2.18}$$

where γ_j represents the gas broadening rate as described in Eqn. 2.14, δ_j is the shift rate as described in Eqn. 2.15, and P_j is the buffer gas pressure inside the prefilled cell at temperature T_j as described by Eqn. 2.16.

K–K interactions also result in Lorentzian broadening [73]. For potassium, temperatures must exceed 440 K for the collisional broadening to become comparable to the natural linewidth [4]. In our K study in Chapter 5, the temperature is below this value, so K–K collisional broadening is insignificant.

Figure 2.5 illustrates theoretical potassium D1 transmission spectra, derived using *ElecSus* and Eqns. 2.14 - 2.18, at $T = 363$ K. The purple, blue and red spectra correspond to the vapour cell with no buffer gas, 60 Torr, 100 Torr of neon respectively, which are the same conditions that will be used in Chapter 5. At 0 Torr, the spectrum displays a dominant Doppler-broadened profile with a Gaussian shape, owing to the fact that the Doppler width exceeds the natural broadening contribution by two orders of magnitude. The near-zero transmission at line centre reflects the high optical depth of the potassium vapour, with the probe light being almost completely absorbed on resonance. Since the ground state hyperfine splitting and isotope shift are smaller than the Doppler width, only one absorption line is observed. It is important to note that the optical transmission for a 0 Torr vapour cell will return to 1 within a few GHz of the atomic reference frequency, which shows a narrow spectral feature. As the fill-pressure rises to 60 Torr, collision-induced effects become clearly observable, this effect appears as a broadening ($\Gamma \approx 430$ MHz) and shift ($S \approx -89$ MHz) of the line centre, leading to a Voigt lineshape. In comparison with the buffer-gas-free cell, for the 60 Torr and 100 Torr cells the

optical transmission does not return to 1 until about ± 5 GHz which shows the Lorentzian component of the pressure broadening is predominant in the Voigt profile, particularly in the wings. At a temperature of 314 K, the Doppler width is around 800 MHz, which is comparable to the pressure broadening observed in the 100 Torr cell. This indicates that collisional effects are significant at this pressure. Investigation temperatures higher than 314 K allows the study of a regime where pressure broadening becomes more dominant than thermal (Doppler) effect. At 100 Torr, these effects become more pronounced, with Γ reaching around 704 MHz and the S approximately -145 MHz. The lower plots illustrate how Γ and S vary with temperature at pressures of 60 and 100 Torr. The broadening Γ increases with temperature, more steeply at 100 Torr, due to the higher collision rate. The shift S remains negative and its magnitude increases with temperature. These results highlight the strong dependence of the spectral line shape, broadening, and shift on both temperature and pressure, highlighting the impact of collisional dynamics on potassium vapour's optical properties.

2.5   Number density and temperature

In many experiments with atomic vapours, optical depth is an important parameter which determines the strength of light-atom interaction. In order to achieve a high optical depth in a dense setup, it is necessary to increase the absorption coefficient and it is best achieved by raising the atomic number density.

The number density of alkali-metal vapours is largely controlled by the vapour pressure, which is highly sensitive to changes in temperature. As can be seen in Figure 2.6 (left panels), the number density for both rubidium (Rb) and potassium (K) increases nearly exponentially with temperature, with Rb having a much higher number density at lower temperatures compared to K. For example, a temperature increase of $10\,°C$ around room temperature can almost triple the number density for Rb. More generally, an order of magnitude increase in number density is normally achieved through a temperature increase of $20-40\,°C$, depending on the
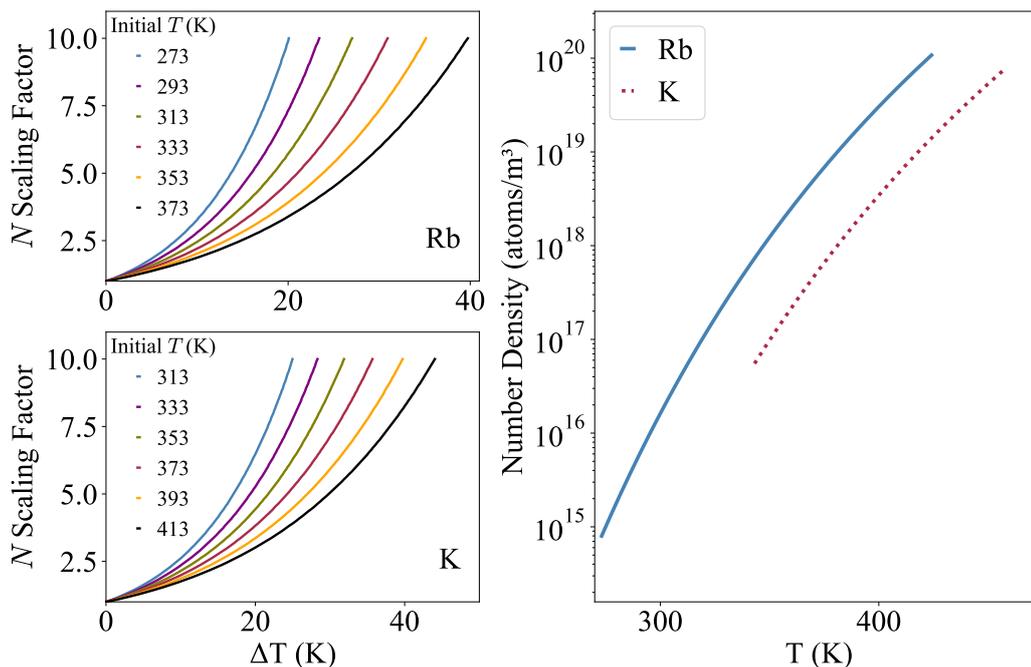
Figure 2.6: Right: vapour pressure curves for the alkali-metal atoms Rb and K. Note that the y-axis is plotted on a log scale. Left: temperature dependence of Rb and K number density [4].

particular species and starting temperature. This property is especially beneficial for Rb which already possess high number density at or near room temperature, thus making it better suited for a variety of quantum optics and atomic physics experiments.

By contrast, elements such as K, which has lower vapour pressures at room temperature, generally require heated vapour cells to achieve suitable optical depths for experiments. As shown in the lower left panel of Figure 2.6, significant increases in K number density require correspondingly higher starting temperatures than for Rb. The right-hand panel of Figure 2.6 shows an obvious comparison of Rb and K, highlighting the result that Rb achieves higher number densities at a given temperature compared to K.

The rapid increase in number density with temperature is also evident from the absorption spectra of these vapours. Figure 2.7 illustrates the observed transmission spectra of rubidium (Rb) and potassium (K) vapours as a function of laser

detuning from the D1 transition. The Rb spectrum represented by the blue trace shows complex and deep absorption features that are indicative of an extremely high optical depth due to the high number density. In contrast, the K spectrum represented by the red trace shows much weaker absorption under similar conditions but at lower number density at the corresponding temperatures. In addition, for Rb a vapour cell that is a few cm long at room temperature has a high enough number density to detect notable absorption features. However, in potassium, the vapour cell must be heated due to its higher melting point [84], ensuring a sufficient atomic vapour number density to get observable absorption properties.
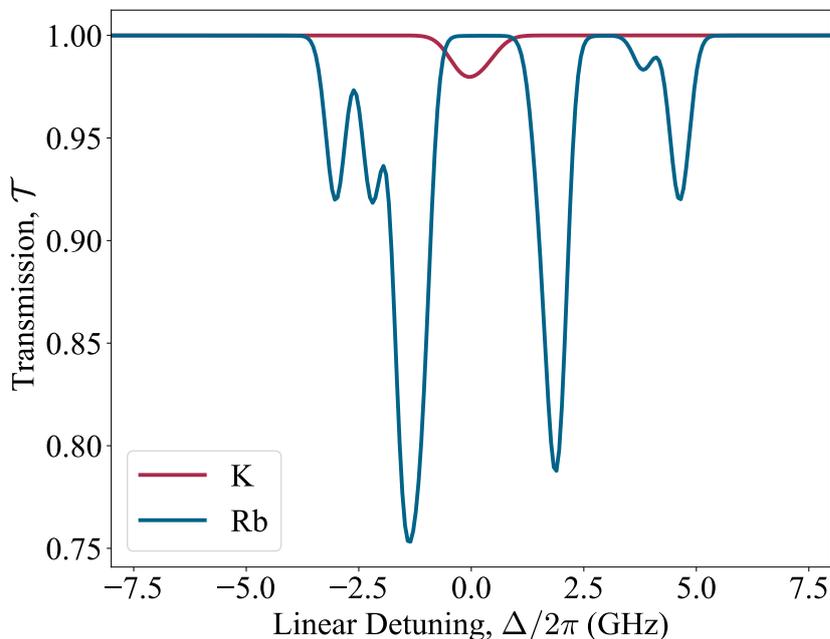
Figure 2.7: Comparison of Rb (blue line) and K (red line) D1 theoretical spectra predicted by *ElecSus* at room temperature as a function of detuning . The transmissions are for 75 mm a natural abundance rubidium and potassium vapour cell.

2.6   The hyperfine Paschen-Back regime

Placing atoms in a magnetic field $\vec{B}$ leads to a shift in the energy of their states, and consequently in the frequency of the light required to excite transitions between them [85]. This phenomenon knowns as the Zeeman effect. This shift occurs due to the interaction of the magnetic field with the electron's orbital motion, the
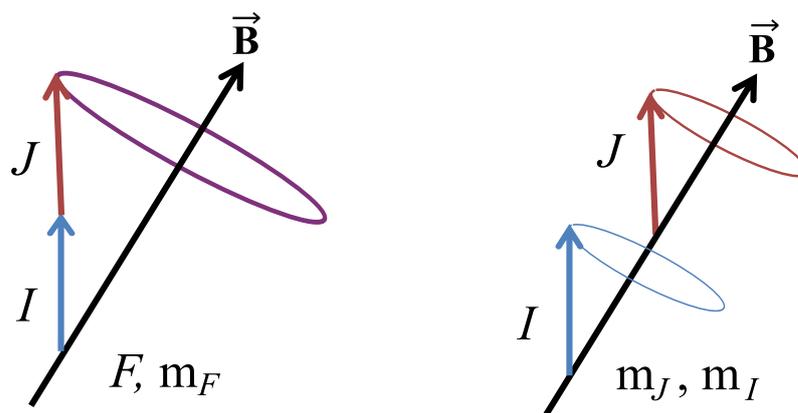
Figure 2.8: A diagram illustrating the motion of different angular momenta in an atom under an external magnetic field $\vec{B}$. On the left, at low magnetic field strength, the electron's total angular momentum J and the nuclear spin I couple to form the total angular momentum F, which then precesses around B, with (F, m_F) being the appropriate quantum numbers in this regime. On the right, at higher magnetic field strengths, the Zeeman shift becomes comparable to or exceeds the atom's hyperfine structure, making (F, m_F) no longer suitable for describing the energy states. Instead, in the hyperfine Paschen-Back regime, the energy states are characterised by the quantum numbers (J, m_J) and (I, m_I), with J and I precessing independently around B.

electron's spin, and the nuclear spin. This behavior is described by the Hamiltonian [66]

$$\hat{H}_{\text{Zeeman}} = -\frac{\mu_{\text{B}}}{\hbar}\left(g_L\vec{L} + g_S\vec{S} + \frac{m_{\text{e}}}{m_{\text{p}}}g_I\vec{I}\right)\cdot\vec{B}, \qquad (2.19)$$

where g_L, g_S, and g_I are the Lande g-factor for L,S, and I, respectively. μ_{B} is the Bohr magneton and m_{e} and m_{p} are the masses of the electron and proton, respectively. At low magnetic field strengths, the atom-magnetic field (Zeeman) interaction is weaker than all the hyperfine ones. In this regime, (F, m_F) are good quantum numbers in the ground and excited states as shown in Figure 2.8. In this case, the Zeeman effect can be expressed as:

$$\hat{H}_{\text{Zeeman}} = -\frac{\mu_{\text{B}}}{\hbar}\left(g_F\vec{F}\right)\cdot\vec{B}, \qquad (2.20)$$

where g_F is the Lande g-factor for F [86]. The energy levels shift is linearly proportional to the strength of B. As a result, the energy levels will see their energy shifted due to the Zeeman effect by an amount $\Delta E = g_F m_F \mu_{\text{B}} B$, with

$m_F = -F, -F + 1, ..., F - 1, F$; this is called the hyperfine linear Zeeman regime. As the magnetic field increases (~ 0.1 T in Rb), the Zeeman interaction is comparable to the excited state hyperfine interaction. In this regime (F, m_F) remain valid quantum numbers for the ground state, while (m_J, m_I) are more convenient to use in the excited state. This difference in the preferred quantum numbers makes it challenging to obtain analytical results in this regime. At very large magnetic field where the strong B decouples the total angular momentum of the electron $\vec{J}$ from the nuclear spin $\vec{I}$, the system reach the hyperfine Paschen-Back (HPB) regime. In this regime, the Zeeman energy shift becomes larger than the hyperfine splitting and the energy levels shift linearly with the magnetic field, according to $\Delta E = g_J m_J \mu_B B$, where g_J is the Lande g-factor for J. Here, the splitting of atomic levels is described by the quantum number projections (m_J) and (m_I) instead of F and m_F as shown in Figure 2.8. We have neglected the energy shift from the nuclear magnetic moment, as it is three orders of magnitude smaller than the Bohr magneton and therefore has a negligible effect in this regime [86].

The magnetic field required to enter the HPB regime can be estimated using the formula: $B_{HPB} = A_{hf}/\mu_B$, where A_{hf} is the magnetic dipole constant for the ground term; this is calculated to be around 700 G for ^{85}Rb and 2000 G for ^{87}Rb [39, 87]. However, the corresponding field for potassium is significantly lower (165 G) because it has a smaller hyperfine splitting constant, leading to a reduced field required for the Zeeman energy shift to dominate over the hyperfine splitting [4, 88].

Figure 2.9 compares the theoretical absorption spectra for the Rb D2 line as the magnetic field strength is increased. In panel (a), with no magnetic field, the total angular momentum F and its projection m_F are effective quantum numbers. The spectra are clear, however, there are several unresolved close lying transitions within each absorption feature. In panel (b), at 1 kG, the system is in a regime where F and m_F are no longer well defined, producing a more complicated spectrum. In Figure 2.9 (c), the field is at 3 kG, individual transitions begin to resolve, although some overlapping still remain, whereas (d), at B = 6 kG, the system is in the

hyperfine Paschen-Back regime, where m_I and m_J are good quantum numbers. In this regime, the transitions are separated by more than their Dopper width, allowing clear identification of individual transitions.

Figure 2.10 illustrates the theoretical transmission spectra of the potassium D1 line at $T = 343$ K for a 25 mm vapour cell and five different magnetic field strengths: 100 G (red), 300 G (blue), 500 G (purple), 700 G (olive), and 1 kG (black). At lower magnetic field such as $B = 100$ G, the system remains below the hyperfine Paschen-Back (HPB) regime. In this regime, the total angular momentum F remains a good quantum number, whereas the Zeeman effect is relatively small. As a result, the individual absorption features remain not resolvable, and the transmission spectrum exhibits a single dip centred around zero detuning. At $B = 300$ G, the Zeeman splitting is small but clearly visible, with absorption peaks showing significant overlap. As B increases further, the splitting continues to grow and the features are well-resolved. At the highest magnetic field, the spectrum shows the largest splitting, with the central dip becoming less pronounced.
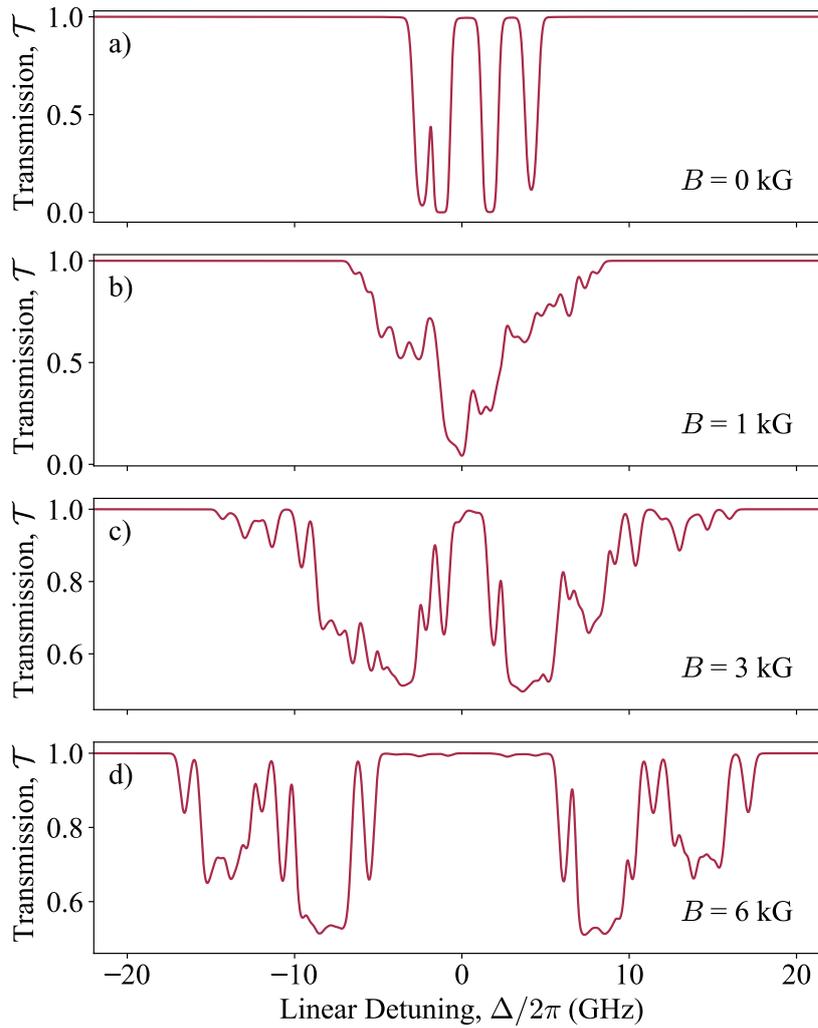
Figure 2.9: Theoretical D2 transmission spectra of a 25 mm Rb vapour cell at 323 K calculated at different magnetic field strengths using *ElecSus*. At higher magnetic field strength, the number of transitions increases but their intensity decreases. When the magnetic field strength is 6 kG, the transitions are split by more than their Doppler width.
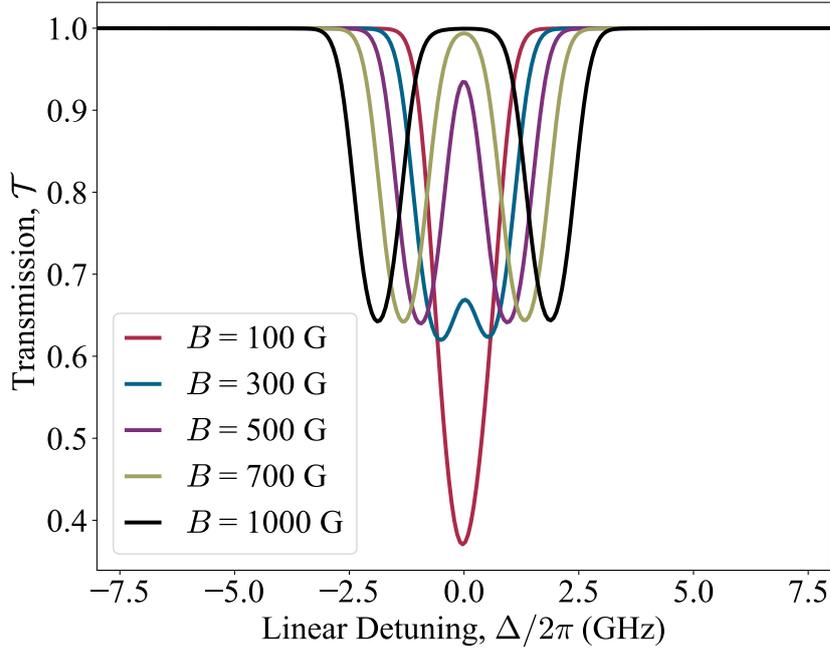
Figure 2.10: Theoretical D1 spectra for a potassium vapour cell of length 25 mm at $T = 343$ K and the magnetic field is 100 G (red), 300 G (blue), 500 G (purple), 700 G (olive) and 1 kG (black).

2.7 Stokes polarimetry

The polarisation state of transmitted light can be described using the Stokes parameters [89, 90]. These parameters are particularly well-suited for studying the interaction between atoms, light, and magnetic fields because the geometry of this interaction leads to propagation eigenmodes that can easily be expressed in terms of the polarisation of light. By measuring the intensity of the beam in orthogonal polarisation bases, we can gather information not only about the medium's absorption but also about the optical rotation it induces.

We can measure the four Stokes parameters, where the total transmitted intensity is independent of the measurement basis:

$$I_{\mathrm{T}} \equiv I_{\mathrm{H}} + I_{\mathrm{V}} = I_{\nearrow} + I_{\searrow} = I_{\mathrm{RCP}} + I_{\mathrm{LCP}} \ . \tag{2.21}$$

We define the normalised Stokes parameter S_0 as the ratio of the light transmitted by the medium to the incident light, $S_0 = I_{\mathrm{T}}/I_0$.

The remaining Stokes parameters, normalised with respect to the intensity of the transmitted light, S_1, S_2 and S_3, are defined as,

$$S_1 \equiv (I_{\mathrm{H}} - I_{\mathrm{V}}) / (I_{\mathrm{H}} + I_{\mathrm{V}}), \tag{2.22}$$

$$S_2 \equiv (I_{\nearrow} - I_{\searrow}) / (I_{\nearrow} + I_{\searrow}), \tag{2.23}$$

$$S_3 \equiv (I_{\mathrm{RCP}} - I_{\mathrm{LCP}}) / (I_{\mathrm{RCP}} + I_{\mathrm{LCP}}). \tag{2.24}$$

S_1 represents the intensity difference between linearly polarised light that is horizontally and vertically oriented. S_2 represents the intensity difference between the linearly polarised light at an angle $+\pi/4$ and $-\pi/4$. The fourth parameter which is S_3 describes the variations in intensity between right and left hand circularly polarised light.
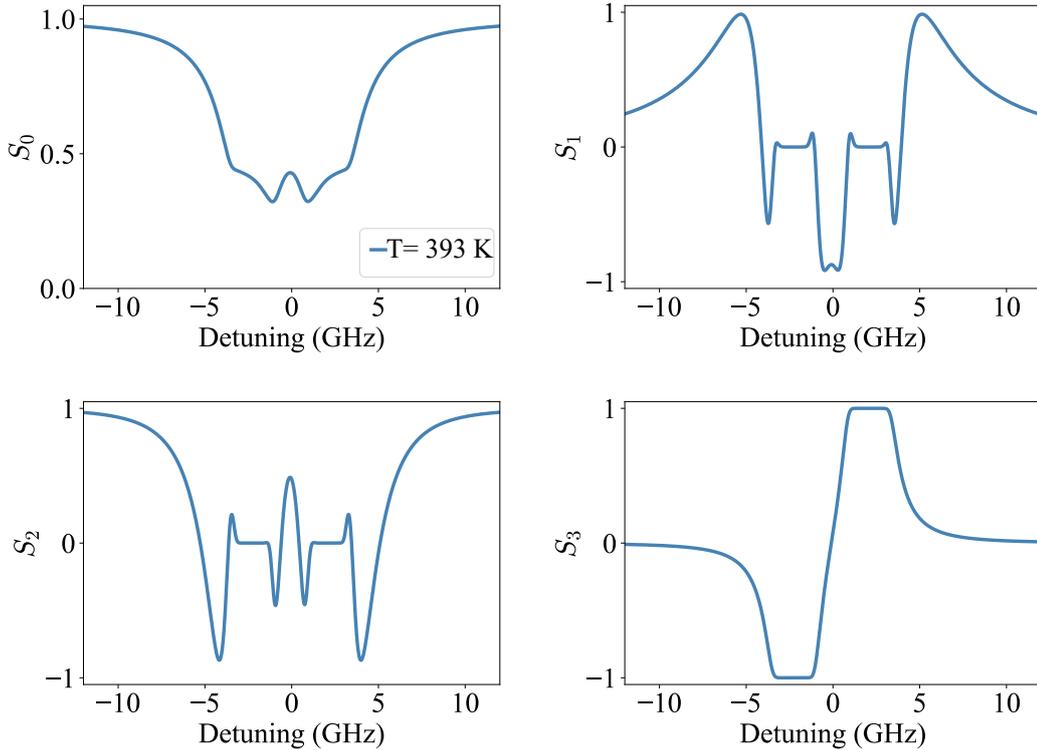
Figure 2.11: Theoretical normalised Stokes parameters – (a) S_0, (b) S_1, (c) S_2 and (d) S_3 – for a potassium vapour cell of length 25 mm containing 60 Torr of neon buffer gas. The temperature is set to 393 K and the magnetic field is 1160 G.

Figure 2.11 presents the theoretical predicted Stokes parameters (S_0, S_1, S_2, S_3) as a function of linear detuning for a 25 mm potassium vapour cell containing 60 Torr of neon buffer gas at an applied magnetic field of 1160 G in a Faraday configuration which is the maximum field that we could achived in our investigation [2]. We use *ElecSus* to produce these perdictions under the weak-probe regime and the temperature is at 393 K. The input light is linearly polarised at 45° to the axis of polarisation, ensuring equal contributions of left- and right-circularly polarised light incident on the atomic medium. Figure 1 (a) shows S_0, which represents the total transmitted light intensity. Its value never exceeds 1 because it is normalised to the output light intensity. Figure 1 (b) and (c) represent S_1 and S_2, respectively, which describe how the linear polarisation state changes as light passes through the atomic medium. Panel (d) displays S_3, the circular polarisation component. This parameter is particularly sensitive to the magnetic field. The circular birefringence (Faraday rotation) and circular dichroism create the distinctive dispersive shape, with its sharp zero-crossing near 0 GHz detuning which is indicative of the strong Faraday rotation effect.

However, recent research has shown that optimal filter performance can be achieved using arbitrary magnetic field angle setups where the magnetic field is oriented at neither 0 or 90° relative to the light propagation direction [1, 91]. In this configuration, the eigenmodes become elliptically polarised light, combining characteristics of both circular and linear polarisations. This configuration can provide narrower transmission linewidths and higher peak transmission compared to the traditional Faraday and Voigt configurations, especially when optimised for specific applications. While this configuration offers high filter performance, it requires precise control of the magnetic field angle which is typically within 1° accuracy over the vapour cell length. Traditional methods using rotating permanent magnets can not be used for longer vapour cells due to mechanical constraints and field non-uniformities. This has motivated the development of new magnetic field generation method, as will be discussed in detail in Chapter 4.

CHAPTER 3

Experimental details

This chapter will briefly summarise some of the details of the experimental setup which are general to most of this work. In particular it will describe the vapour cells, heating systems, magnetic field control apparatus, and the laser frequency calibration procedures that enable quantitative comparison between experimental measurements and theoretical predictions.

3.1 Vapour cells and heaters

We use different vapour cells – containing either rubidium or potassium (with or without buffer gas) of various lengths – throughout this thesis depending on the scientific investigation.

In Chapter 4, where we investigate arbitrary angle rubidium magneto-optical filter experiments, we use a commercially-sourced 75 mm length natural abundance Rb cylindrical vapour cell. This extended cell length was specifically selected because it allowed for operation at lower temperatures compared to the 5 mm length vapour cells used in previous arbitrary-angle filter studies [56]. Working at a lower vapour temperature reduces the effects of self-broadening and generally improves the efficiency of the filter [57]. With the cell positioned centrally within a solenoid
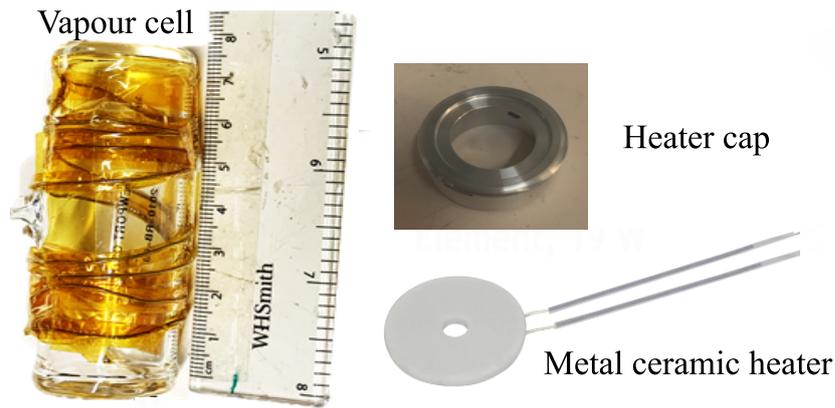
Figure 3.1: Components used for heating the vapour cell. The vapour cell (left) that contains Rb atoms is wrapped with a heating wire and a metal ceramic heater (bottom right) is used to enable sufficient atomic number density and provide uniform heating. Moreover, a heater cap (top right) helps maintain thermal stability and reduce heat loss to ensure the cell can reach necessary temperatures for required filter performance.

(to generate the axial (or Faraday) component of the magnetic field) a compact heater was required. Temperature control of the rubidium vapour cell was achieved using a heating wire, wrapped around the cylindrical body of the cell, and two ceramic heaters with one on each vapour cell flat window face (referred to as "end cap heaters"). Figure 3.1 are photographs of the heating wire (left) and end cap heaters (right). The white disc with a central hole is the ceramic heater and the aluminium heater cap is a bespoke, and machined in-house, to hold the ceramic end on the end of the vapour cell window. The central hole permits the laser beam to transverse the centre of the vapour cell. Before insertion into the solenoid, the vapour cell and heaters are wrapped in fibre-glass insulation to aid thermal stability.

In Chapter 5, we investigate potassium spectroscopy in the presence of buffer gas. The experiments were initially performed using commercially-sourced bespoke 25 mm cylindrical vapour cells without anti-reflection (AR) coated windows from Precision Glassblowing (referred to as "Cell 1"). They were sealed at room temperature either under vacuum (no buffer gas) or with neon gas at pressures of 60 Torr and 100 Torr. During the investigation in Chapter 5, we discovered experimental

difficulties, which led to new vapour cell design being adopted (referred to as "Cell 2").

Cell 1: Cylindrical non-AR coated cells

As a consequence of the "Cell 1" vapour cells having no AR coating, we noticed significant background fluctuations when the cell windows were orthogonal to the laser beam propagation axis; this was due to internal reflections (etalon fringes) as shown in the left of Figure 3.2. Here, we would expect the off-resonance background to be at a constant value[4], but instead varies with changing vapour cell temperature. To solve this problem, the vapour cells were tilted slightly off normal incidence, reducing back reflections, as shown in the right of Figure 3.2. Here, we observed the expected flat signal background. However, setting up the vapour cell this way caused additional problems, especially upon inclusion of the magnetic field where the laser propagation axis was no longer aligned with the magnetic field axis (i.e. no longer Faraday configuration).

Another difficulty with using these vapour cells was controlling a uniform temperature of the vapour cell. As discussed in Chapter 2, and shown in Figure 2.7, potassium has a lower vapour pressure than rubidium at room temperature, therefore requires a higher temperature to achieve similar optical depths. Additionally, since the purpose of investigating potassium spectroscopy in the presence of buffer gas was to study the filter profiles required for solar studies [19], where the full solar disc is imaged through the potassium magneto-optical filter, a clear aperture of 20 mm, across the face of each vapour cell, is required. For the solar filter to have the correct filter profile, each vapour cell needs to be heated to approximately 423 K. With such a large area on the face of each vapour not being actively heated, the coldest region within the vapour cell tended to be the flat windows; consequently potassium condensed on these windows, as shown in Figure 3.2 c), which significantly reduced the image quality and made on-axis imaging very difficult.

Consequently, a different heater to the one used in Chapter 4 was required since
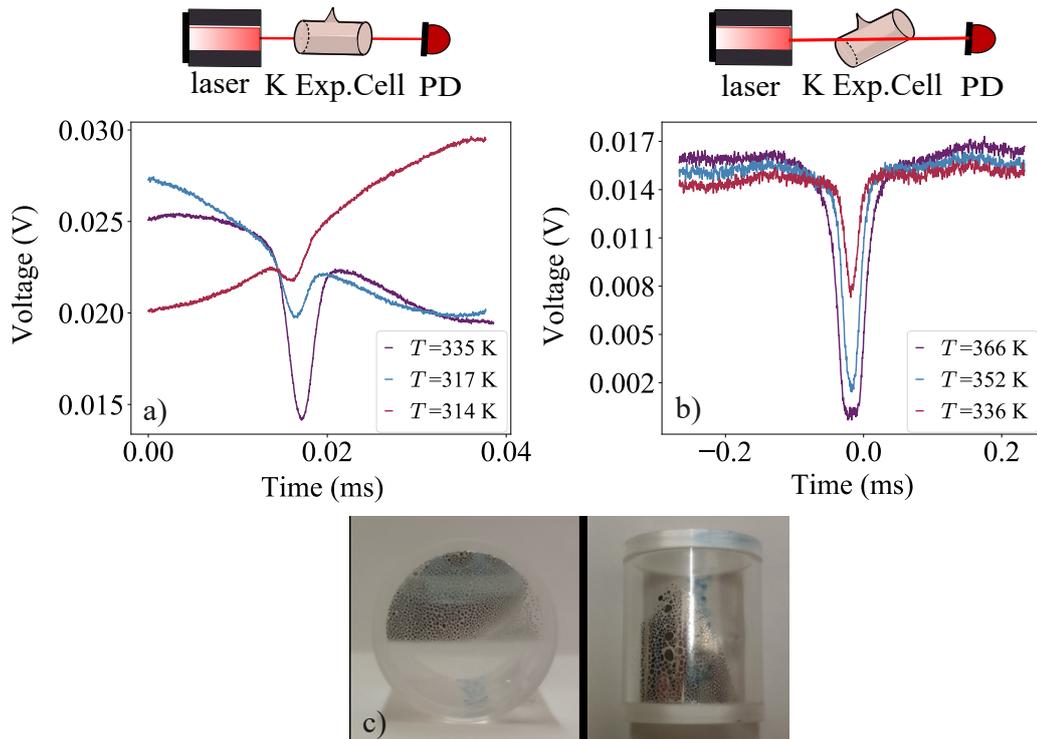
Figure 3.2: Spectra of potassium vapour using 25 mm cells without anti-reflection (AR) coating for various temperatures. a) the cell at normal incidence, exhibiting significant background variation due to etalon fringes. b) the same cell tilted for reduction of reflection which leads to better background. c) photos show potassium condensed on the uncoated cell windows, particularly problematic when using large beam diameters at high temperatures. The spectra shown here are raw data recorded directly from the oscilloscope; hence the x-axis is time (ms) rather than detuning. Setup diagrams above illustrate the measurement configuration.

the small hole in the ceramic heater was too small. Instead, the vapour cells were heated using two end caps, each with a resistive cartridge heater inserted into the body of the cap, to control the temperature. A thermocouple was attached to the cell body for monitoring the temperature, and the temperature is regulated by controlling the current supplied to the resistive cartridge heaters.

Cell 2: T-shaped AR-coated vapour cells

In order to address these concerns, we used bespoke T-shaped vapour cells that had AR-coated, flat, parallel windows. A photograph of this cell is shown in Figure 3.3 (a). These, too, were manufactured by Precision Glassblowing. The T-shaped cell featured a 75 mm long, 25 mm cylinder with a 40 mm long, 6 mm diameter stem (or potassium reservoir), which was included to create a temperature gradient. These cells were also sealed under vacuum (no buffer gas) or with neon gas at 60 and 100 Torr at room temperature. We also purchased a 25 mm long cell having similar stem to the longer cells, with 60 Torr of neon gas, so that spectroscopy in a large magnetic field (well into the hyperfine Paschen-Back regime) in Faraday configuration could be investigated.

For the first part of the study investigating the effects of buffer gas on the potassium D1 line (broadening, shift, and temperature dependence), we used 75 mm length vapour cells (with a stem). However, for the study of spectral line shape evolution in the presence of a magnetic field, we employed 25 mm vapour cells (with a stem) to ensure that all of the atomic vapour was contained within the magnetic field region.

3.1.1 Temperature control of T-shaped cell

As illustrated in Figure 3.3, the extended stem creates the requirement for the control of two distinct temperatures: one for the main body of the cell and one for the stem. If the cell body is too hot with respect to the stem, potassium atoms can migrate into the stem, whereas they can condense on the inner cell windows if the stem is heated excessively, which would reduce the optical transmission. Thus, in order to maintain a stable atomic vapour profile, minimising the temperature gradient between the stem and the cell body is critical.

To overcome this problem, we developed a dual-zone heating system, as shown in Figure 3.3. We optimise the heating system to provide independent and stable
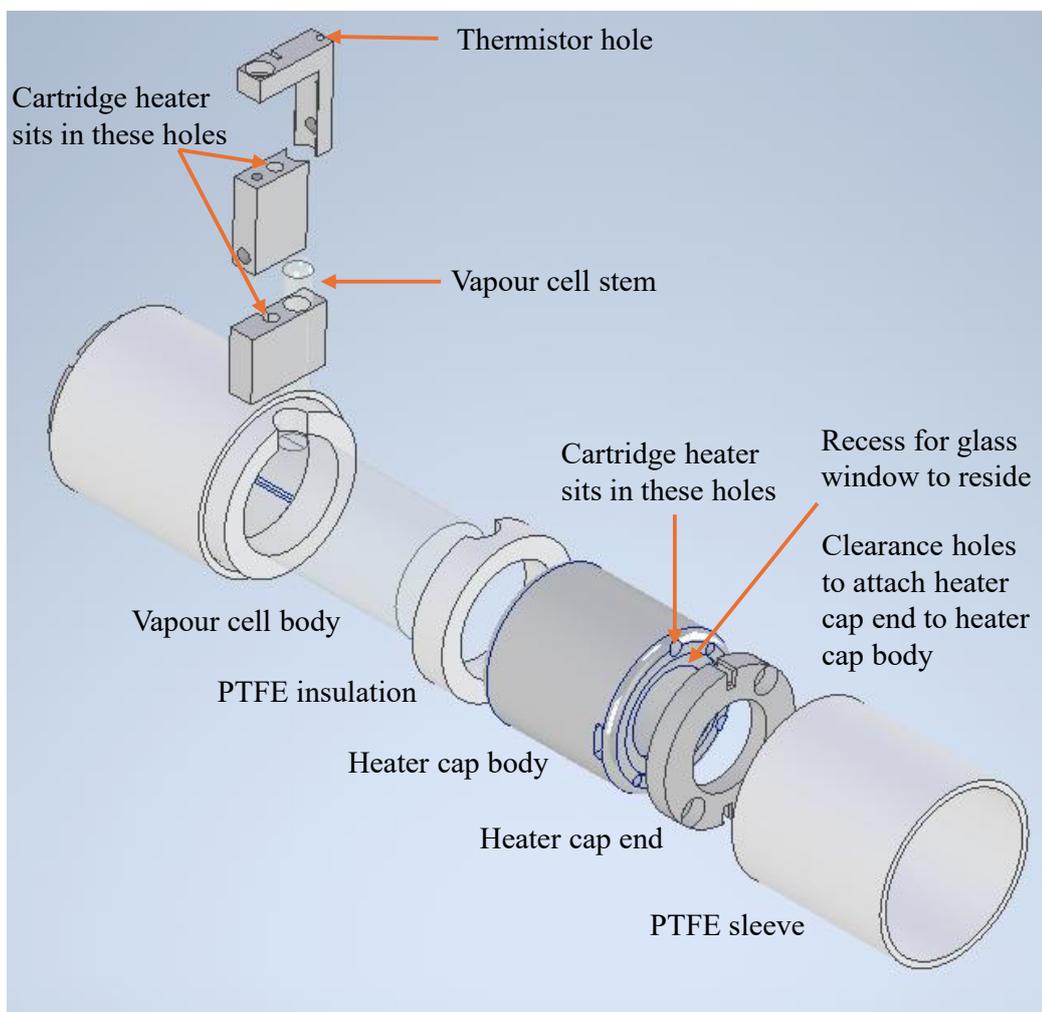
Figure 3.3: Schematic representation of the T-shaped vapour cell heater assembly. The figure illustrates the vapour cell body and stem, PTFE sleeve, heater cap body and heater cap end, PTFE insulation, cartridge heater holes, thermistor hole, recess for the glass window, and clearance holes used to attach the heater cap end to the heater cap body. The design provides uniform heating of the vapour cell while maintaining mechanical stability and thermal insulation.

temperature control for both the cell and the stem. One of the key design challenges was preserving optical access while fitting the vapour cell and heater inside the magnet holder of the solar filters, which only provided a 6 mm clearance for the stem. Thus, two independent resistive cartridge heaters was developed: one segment for the main cell body and one for the stem, allowing for independent control of the stem temperature (T_s) and the cell body temperature (T_c). This arrangement maximises both thermal isolation as well as light transmission through the cell. Thermocouples were attached to the stem and cell body to monitor overheating. The T_c was approximately 20 K above the T_s during the experiments. We utilise a modified version of the *ElecSus* where the stem and cell temperature are controlled independently. This feature was critical for our studying of the thermal effects on the transmission spectrum.

Figure 3.4 illustrates how the transmission spectrum changes when independently varying T_s and T_c. When the T_c is increased while the T_s remains fixed, as in Figure 3.4 (a), the Doppler broadening of the spectral lines increases due to the higher thermal velocity of the atoms. In spite of the broadening, the integrated absorption, which is identified as the area under the curve, remains roughly invariant which suggests that the total number of absorbing atoms is not changing significantly.

In contrast, when T_s is increased while keeping T_c fixed, as in Figure 3.4 (b), the line depth becomes noticeably deeper, whilst the Doppler width stays unchanged. This is indicative of an increase of atomic number density in the cell, likely as a result of increased vapour flow from the hotter stem into the cell body, evaporating without changing the velocity distribution. These observations highlight the importance of independent control of T_c and T_s when optimising the vapour density and spectral profile for precision spectroscopy applications.
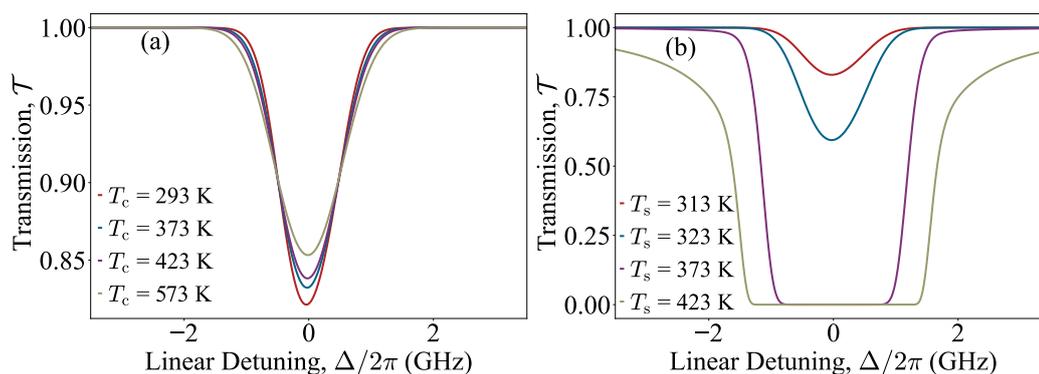
Figure 3.4: Simulated potassium D1 line transmission spectra using *ElecSus* under two conditions: (a) varying T_c while keeping T_s constant at 313 K; and (b) varying T_s while keeping T_c constant at 353 K.

3.2 Magnets

The experiments described in Chapter 4 – which investigates Rb magneto-optical filters – require the application of both axial and transverse magnetic fields to the vapour cell. To achieve this, a combination of permanent magnets and a solenoid was implemented, with each component designed to provide precise control over the direction and magnitude of the magnetic fields as shown in Figure 3.5. The transverse component of the magnetic field is generated using commercially available strontium ferrite permanent magnets of grade Y30BH. These grades were selected due to their ready availability and particular suitability for this application. Each magnet is cuboidal with dimensions of 15 mm x 20 mm x 60 mm along the x, y, and z axes, respectively. The magnets are magnetised along the x-axis and each magnet varies in strength. The difference between the weakest and strongest magnet is approximately 5%. To ensure uniform magnetic field coverage across the 75 mm length of the Rb vapour cell, three magnets were stacked along the z-axis for each half of the setup. This resulted in a total of six magnets which form the Voigt permanent magnet configuration. Each three set of magnets was mounted using 3D printed plastic holders. The complete Voigt permanent magnet geometry was formed using symmetrical pairs of holders, with adjustable spacing between the magnets along the x-axis.
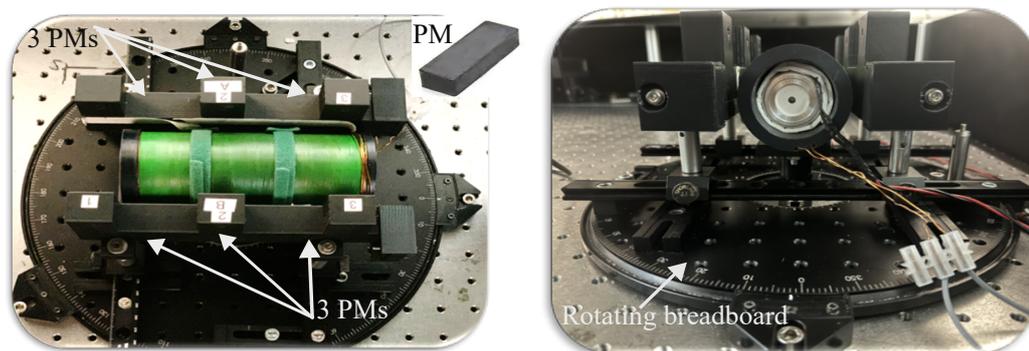
Figure 3.5: The photographs display the solenoid-plus-permanent magnetic field device mounted on a Thorlabs rotating breadboard with a removable centre for testing with or without the solenoid. The devices required for converting the setup into a filter are not included. In the top view (left), the solenoid, shown as a green cylinder, is placed between permanent magnets (PMs), whose positions are indicated by arrows. An inset shows the shape of a single PM for clarity. The right on-axis view shows the temperature control for the vapour cell which consists of two ceramic heaters. One of them, a white disc with a hole in the middle, is positioned in such a way that the laser beam can traverse the vapour cell.

For the purposes of these experiments, the separation between the magnets was configured to 74 mm along the x-axis, generating a magnetic field strength of $|B|$ = 190 G along the propagation axis ($x = 0$, $y = 0$, $z = z'$). A rotating Thorlabs breadboard with a removable central part (RBB300A/M) housed the setup for the Voigt permanent magnet. This arrangement kept the vapour cell fixed along the *z*-axis which is the direction of the laser beam axis while allowing the rotation of the Voigt magnets to easily produce the angles of the imposed arbitrary magnetic fields. To provide a uniform axial field, a solenoid was designed based on simulations using *Magpylib*. The solenoid is 140 mm long with an inner diameter (ID) of 45 mm accommodating the vapour cell and its heater. It consists of 156 turns of 0.9 mm thick copper wire arranged in two layers around a PTFE cylindrical form, which also serves as thermal insulation between the vapour cell and the solenoid. This ensures that the temperature of the vapour cell can be controlled without interference from the magnetic field setup. The configuration yields the required axial field of 13 G with current less than 1 A to prevent overheating of the solenoid wires. The solenoid is fixed to the centre of the rotating breadboard,
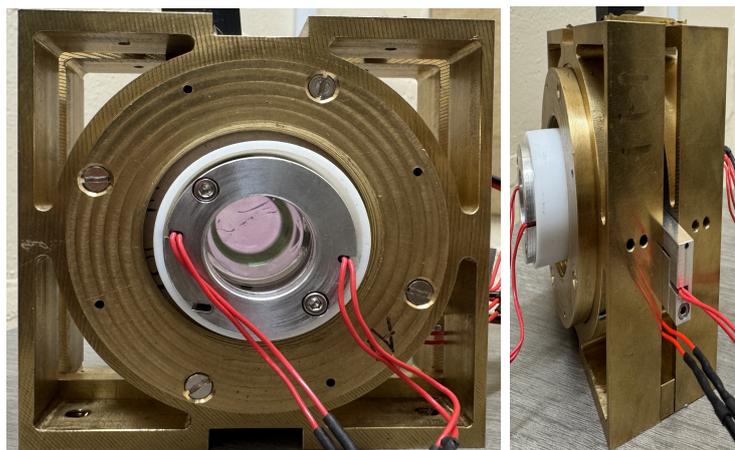
Figure 3.6: Annular permanent magnets in Faraday configuration create an axial magnetic field parallel to the light's k-vector. The adjustable magnet separation allows field strength control up to 1.1 kG with 3% RMS variation along 25 mm vapour cell with 6 mm stem.

creating a structure in which the vapour cell and solenoid remain stationary, while the permanent Voigt magnets are rotated to generate the magnetic field.

For the experiments in Chapters 5 and 6, the magnetic field was created using axially magnetised annular permanent magnets, similar to those described in [92] and shown in Figure 3.6. This magnet configuration consists of layered concentric off-the-shelf N42 neodymium-iron-boron (NdFeB) axially magnetised ring magnets. The magnets are organised into four cylindrical brass holders and two square brackets are used to mount the cylindrical brass holders, containing the magnets, and to secure the magnet holder to the optical table. Each square bracket holds two cylindrical brass holders and the square bracket sit either side of the T-shaped vapour cell stem. The relative separation between the four brass cylinders enables the magnetic field strength to be controlled. Reducing separation of the cylindrical brass holders, increases the axial magnetic field strength.

3.3 Transmission Spectra Calibration

This section describes the calibration procedure for transmission spectra to obtain normalised transmission as a function of linear detuning, ensuring excellent

agreement between theoretical models and experimental measurements.

In our lab, atomic spectra are recorded using an oscilloscope that presents the data as voltage (signal) during the time period of laser frequency scanning. To fit the experimental data with theoretical (*ElecSus*) models, the raw spectra must be calibrated to yield normalised transmission as a function of linear detuning, where this is frequency difference between the laser and the weighted-line centre of the resonance. The experimental setup illustrated in Figure 3.7 has most relevant components of the optical setup used for data calibration and for fitting experimental results to theoretical predictions in this thesis. Light from an external cavity diode laser with a centre wavelength of 780 nm for Rb experiments (diode laser (DL)), or with a centre wavelength of 770 nm for K experiments, passes through an optical isolator (OI) and is then split into two beams using a polarising beam splitter (PBS) and a half-wave plate ($\lambda/2$). A fraction of the output beam is directed to the main experimental setup, while the other is used to calibrate the frequency axis [4, 93] . We use a combination of a Fabry–Pérot etalon (FP) for linearisation and a natural abundance Rb (K) reference cell for defining zero-detuning, which is chosen to be the weighted centre of the line [94]. The reference cell, operated at a temperature that produces at least 50% transmission (for either Rb or K) and in zero magnetic field, utilised a sub-Doppler atomic reference technique with counter-propagating probe and pump beams to provide well-defined spectral features [4]. For the calibration method described in this chapter, Rb cells are used; however, the setup is adaptable for K atoms using cells of different lengths depending on the specific experimental requirements.

The calibration process resolves three issues we have in the raw measurements. Initially, we convert the time axis into a frequency axis using a Fabry–Pérot etalon. The etalon transmission peaks additionally can be used to remove non-linearities from the laser scan. Second, the method eliminates optical power fluctuations occurring during laser scan and normalises the transmission values to be between 0 and 1. Finally, pump–probe Doppler-free spectroscopy can be used to provide
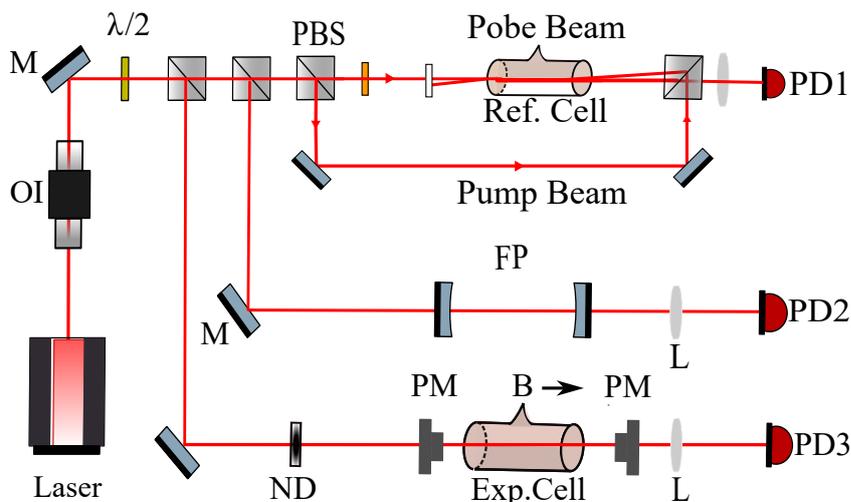
Figure 3.7: Schematic of the most relevant components of the optical setup used for acquiring experimental data in this thesis. Light from an external cavity diode laser passes through an optical isolator (OI) and is split into two components using polarising beam splitter (PBS) cube. One component of the light is used for a reference optical system that linearises and calibrates the laser frequency [4]; the system consists of a room temperature 5 mm natural abundance Rb reference cell (Ref. Cell) and a Fabry–Pérot etalon (FP) made with two mirrors (M) where the transmission through them are monitored on photodetector PD1 and PD2, respectively. The rest of the light is sent to the main experimental setup which consists of neutral-density (ND) filters to control the beam power before passing through a heated experiment cell (Exp. Cell) of length 75 mm contains natural abundance Rb, and is placed between the magnets (PM). For the calibration method described in this chapter, Rb cells are used; however, the setup is adaptable for K atoms using cells of different lengths depending on the specific experimental requirements.

an absolute frequency reference to determine the zero detuning position within the measurement trace.

Three datasets are recorded for each experiment: a Fabry-Pérot etalon signal, a reference signal that distinguishes the various hyperfine peaks, and a transmission signal. The calibration process involves three main steps: (1) laser scan linearisation; (2) transmission normalisation; and (3) absolute frequency calibration.

3.3.1 Laser Scan Linearisation

The first step is to remove non-linearities in the laser scan. To do this, we require an accurate time-to-frequency calibration using transmission peaks from a Fabry-

Pérot etalon. A Fabry–Pérot etalon consists of two highly reflective mirrors that are placed parallel to one another, separated by a distance L. The frequency difference between two normalised etalon peaks is called the free spectral range (v_{FSR}) [4]. Our 10 cm-long cavity that we used in our study [1] has a standard (v_{FSR}) of 750 MHz while the cavity we used in [2] has (v_{FSR}) of 370 MHz.
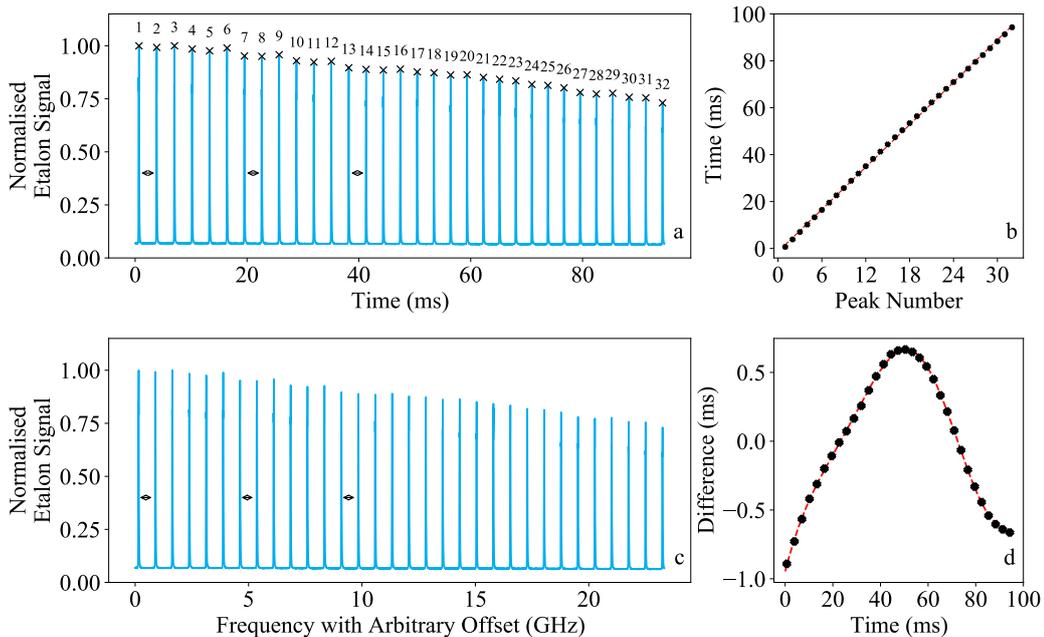
Figure 3.8: a) Transmission spectra for normalised etalons. The find peaks function in the scipy Python package is used to locate the etalon peaks (black crosses, peaks numbered). Peak detection is aided by using minimum peak height and distance. b) Time position of each peak on the etalon scan, numbered from left to right, with the expected linear fit (red, dashed line). c) Nonlinearities in the laser scan have been eliminated and the time axis has been converted to a relative frequency. d) The difference between each etalon peak time position and the linear fit. A high order of polynomial is fit to the deviation in order to stretch the horizontal which leads to a linear relationship between the horizontal axis and laser frequency.

For a linear piezoelectric transducer response in the external cavity laser, the measured etalon peaks should be evenly spaced in time. By measuring the time difference between etalon peaks and comparing it to the known (v_{FSR}), we can identify and correct scan non-linearities.

Figure 3.8 a) shows the subroutine that normalises etalon peaks and selects all the peaks in the trace with their exact positions. The precise location of each
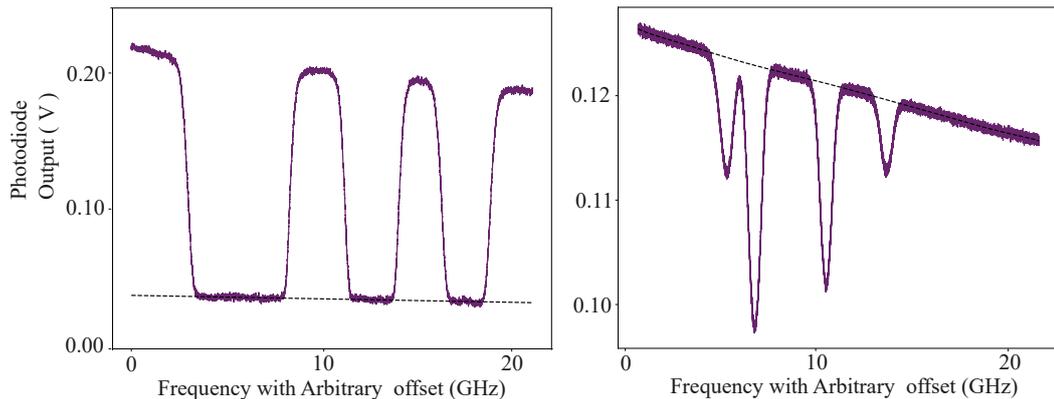
Figure 3.9: Left: Doppler-broadened spectrum from a heated vapour cell. The dark dashed line shows that the photodiode output clearly has an offset. The zero line ($\mathcal{T} = 0$) is defined by fitting a first order polynomial to the data that sit on the black dashed line. Right: Sub-Doppler spectra at room temperature showing variations in laser power with scanning laser frequency (shown as a black dashed line). The one line ($\mathcal{T} = 1$) is defined by choosing the non-resonant regions of the spectra and fitting them to a fifth order polynomial.

etalon peak is plotted as a function of the number of the peaks in Figure 3.8 b). Using the `scipy.optimize` Python module, a least-squares fit determines a linear relationship between peak positions and peak numbers. This module illustrates the conversion of linear time to frequency.

By adding a linear fit to the position of peaks we will see that the scan has a very small non-linear contribution which is the non-linearity that we want to eliminate from the scan. This deviation is plotted a function of the precise peak positions in Figure 3.8 (c). This deviation is fitted with an nth-order polynomial, creating a correction function that is subtracted from the original etalon signal to linearise the time axis. To convert linearised time to frequency we use the known (v_{FSR}) and the fixed separation between adjacent etalon peaks.

Figure 3.8 (d) demonstrates that after linearisation, the separation between adjacent etalon peaks is constant and equivalent to the free spectral range.

3.3.2 Transmission normalisation

To compare transmission scans with theoretical curves, the photodiode output data must be normalised between 0 and 1. This requires defining both zero and unity

transmission levels.

To define zero, the non-zero photodiode offset, caused by optical power fluctuations of the scanning laser, must be removed from sub-Doppler spectra. The atomic vapour is made optically thick by setting the cell heater to a high temperature where there is no resonant laser light that can pass through the medium. The regions with the highest absorption are selected and fitted to a polynomial function, which is then subtracted from the photodiode output data to obtain minimum transmission, as demonstrated in the left panel of Figure 3.9. The right panel of Figure 3.9 represents the Doppler spectrum with laser power variations indicated by the black dashed line. The one line is defined by selecting non-resonant spectral regions and fitting them to a high-order polynomial. The photodiode output data is then divided by this function to achieve maximum transmission normalisation.
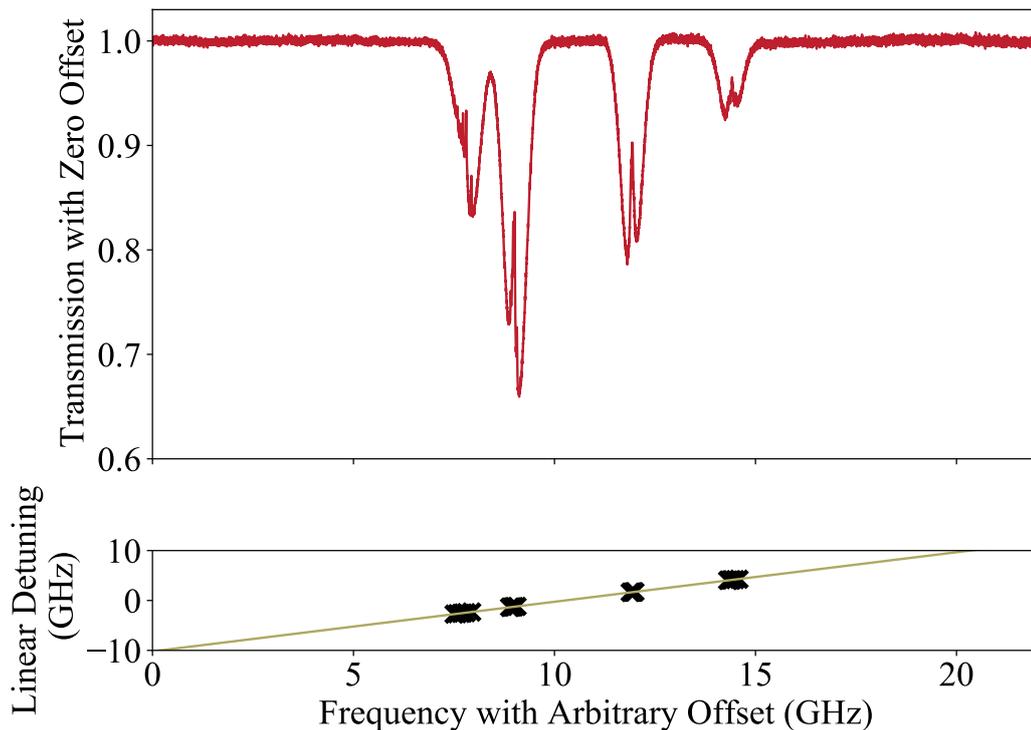
Figure 3.10: The top panel displays the normalised transmission as a function of calibrated relative frequency axis. The below panel shows expected linear detuning values as a function of the frequency with arbitrary offset (black crosses). The relative frequency axis can be transformed into an absolute frequency axis using a linear fit (gold solid line).
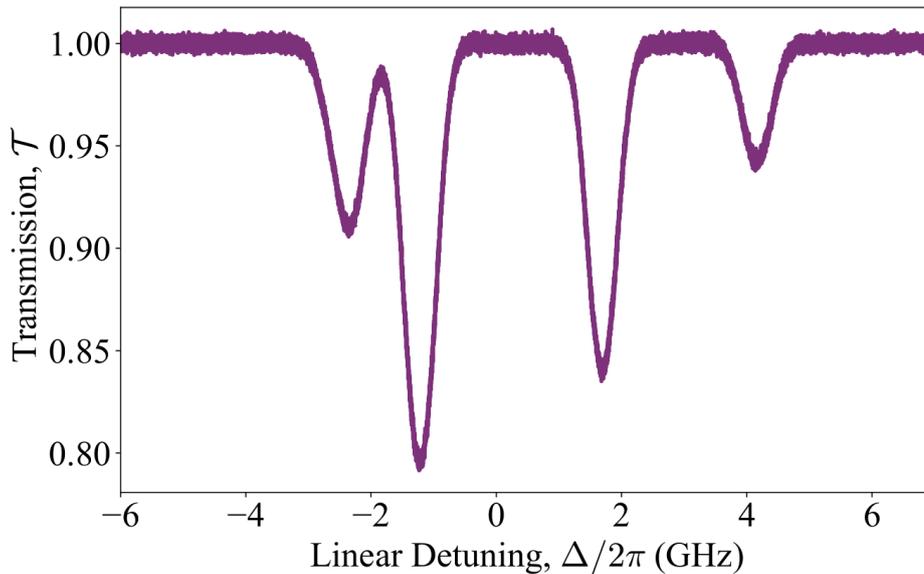
Figure 3.11: Normalised transmission after completing the calibration process as a function of linear detuning. The spectrum is ready to be fitted to the theoretical model which is *ElecSus* in our case.

3.3.3 Absolute Frequency Calibration

Converting the linearised time axis to absolute frequency (linear detuning) requires the sub-Doppler reference spectrum. Details of sub-Doppler spectroscopy can be found in [95] and [4]. The known detuning values for the twelve peaks of the sub-Doppler spectrum which represent resonant transitions or crossovers, are used as frequency markers (Figure 3.10). The absolute detuning values are fitted as a function of detected sub-Doppler peak. We fit a linear to the data, then we extract the slope which should equal to one, confirming successful non-linearity removal, while the intercept indicates the frequency axis shift needed to set zero detuning which typically has been chosen to be the weighted centre of the line [94].

After completing the data processing as shown in Figure 3.11, the experimental spectra can be fitted to our theoretical model which is *ElecSus*.

3.4 Stokes Polarimetry Setup

As discussed in Section 2.7, the polarisation state of light can be described using the Stokes parameters and measured via Stokes polarimetry. Stokes polarimetry not only measures the polarisation state through the atomic medium, but it is also sensitive to any polarisation changes induced by the optical components that are used in the experimental setup.

In Chapters 4 and 6 we investigate the optical rotation through a rubidium vapour and a potassium vapour, respectively. We characterise the optics using Malus's law and find our experimental data agrees very well with theory for our rubidium setup using optics coated for 780 nm (as evidenced by our publication [1]). We tried using standard rubidium optics as the optical elements in the potassium Stokes polarimetry experiments, but found the polarisation purity to be less than ideal, with our potassium Stokes measurements detecting this. In this preliminary experiment of measuring the potassium Stokes parameters, we used a 780 nm half-wave plate ($\lambda/2$) before the experimental vapour cell, and a 780 nm quarter-wave plate ($\lambda/4$) and polariser beam splitter after the experimental cell; this setup allowed us to measure the corresponding components – I_{H} and I_{V}, $I_{\nearrow}$ and $I_{\searrow}$, and I_{RCP} and I_{LCP} – simultaneously, as demonstrated in previous studies [96]. However, since these calibrated optics were designed for 780 nm, we found that these components introduced systematic errors that disagreed with theoretical predictions. For example, when we tested our 780 nm quarter-wave plate we observed an extra feature that was not predicted by theoretical models (see Figure 3.12). Figure 3.12 illustrates the transmission spectra for right- (a) and left-hand (b) circular polarisation using the 780 nm quarter wave plate. Although, the K D1 line is only 10 nm away from 780 nm, we observe a noticeable additional dip at ± 1 GHz, as well as the ^{41}K absorption dip. We fit the data to *ElecSus* and float the electric field vector E and find that the beam is elliptically polarised upon entering the vapour cell as a result of the 780 nm quarter waveplate. This preliminary investigate demonstrated that it is critical to use optical components designed for the correct wavelength to

avoid any polarisation distortions.

It is for these reasons why we used a sequential measurement design with two Glan-Taylor polarisers (labelled "GT1" and "GT2" in Figure 3.13 to represent the polariser before and after the vapour cell, respectively) and an additional 770 nm $\lambda/4$ waveplate, when measuring the S_3 parameter. Due to the way in which GT polarisers work, only the transmitted beam has extremely pure linear polarisation (with the GT having a high extinction ratio for the output beam of 10^4: 1). Linearly polarised light was incident on the first polariser and GT1 was oriented to rotate the plane of polarisation by 45°, as represented by the blue arrows in Figure 3.13. Linearly polarised light at this orientation has equal components of both horizontal and vertical linear light, as well as left- and right-hand circular light, making this the ideal polarisation state to measure all four Stokes parameters. The light passes through a 25 mm T-shaped AR-coated vapour cell, described in section 3.1, that contains potassium atoms with neon buffer gas and is subjected to a magnetic field produced by an axially magnetised annular permanent described in section 3.2. As the polarised light exits the vapour cell, it encounters second Glan-Taylor polariser (GT2). To measure the different intensity components for a particular Stokes parameter, GT2 is rotated and the light is detected on a photodiode (PD). For example, to measure the S_1 parameter, as defined in Eqn. 2.24, GT2 is set to 0° when measuring I_H and rotated through 90° when measuring I_V. Table 3.1 summarises the GT2 angle orientations and quarter-wave plate configurations required for each Stokes parameter measurement, while Figure 3.13 shows the GT2 angle orientations for each of the Stokes parameter measurements.

Figure 3.14 (a) and (b) show the individual intensity measurements of the linear polarisation states that are used to form the normalised Stokes parameters S_1 and S_2, respectively. Panel (a) presents the horizontal (I_H) and vertical (I_V) intensity components, where their difference (I_H - I_V) normalised by their transmitted intensity yields S_1. Panel (b) shows the diagonal ($I_\nearrow$) and anti-diagonal ($I_\searrow$) intensity measurements whose normalised difference describes the rotation of the
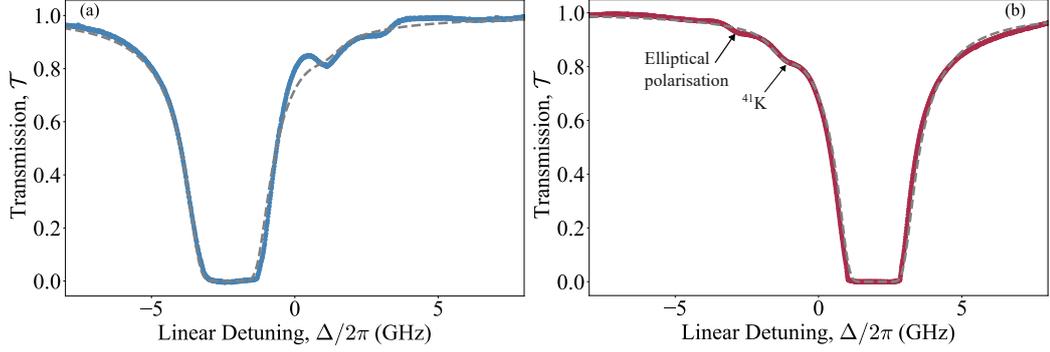
Figure 3.12: Transmission spectra for (a) right and (b) left polarisation using quarter wave plate at 780 nm. Two distinct dips near +1 GHz can be observed: one caused by ^{41}K, and the other due to elliptical polarisation. These are marked with arrows in panel (b).
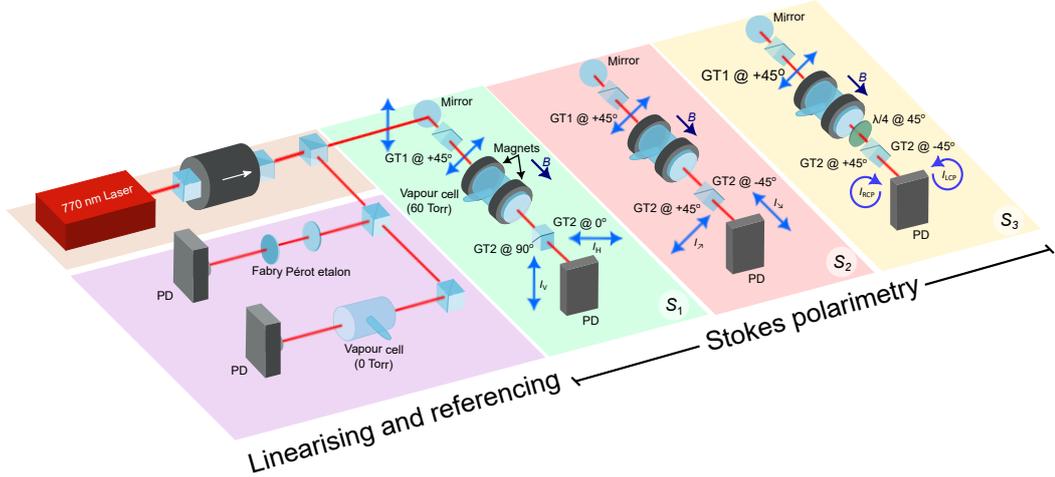
Figure 3.13: Schematic of the experimental apparatus or potassium Stokes polarimetry. 770 nm light (K-D1) from a diode laser (DL) passes through an optical isolator (OI) and is split into two paths using a polarising beam splitter (PBS) cube. The first path is directed towards the reference optics including Fabry-Perot etalon for relative frequency calibration, and 100 mm length buffer-gas free potassium reference vapour cell for absolute frequency calibration. The other fraction of the beam is used to measure Stokes polarimetry in a heated 25 mm potassium vapour cell containing 60 Torr of neon buffer gas. The vapour cell is subjected to a magnetic field that is in Faraday configuration, which can be tuned between 700-1200 G. The experimental setups for measuring S_1, S_2, and S_3 are shown in the corresponding boxes labelled S_1, S_2, and S_3, where the first Glan-Taylor polariser (GT1) defines the input polarisation state and the second Glan-Taylor polariser (GT2) measures the output polarisation state on a photodetector (PD). The polarisation state of light is depicted by blue arrows. For each Stokes parameter, two polarisation measurements are taken with the difference resulting in either S_1, S_2, or S_3. S_0 is determined by summing the two polarisation measurements
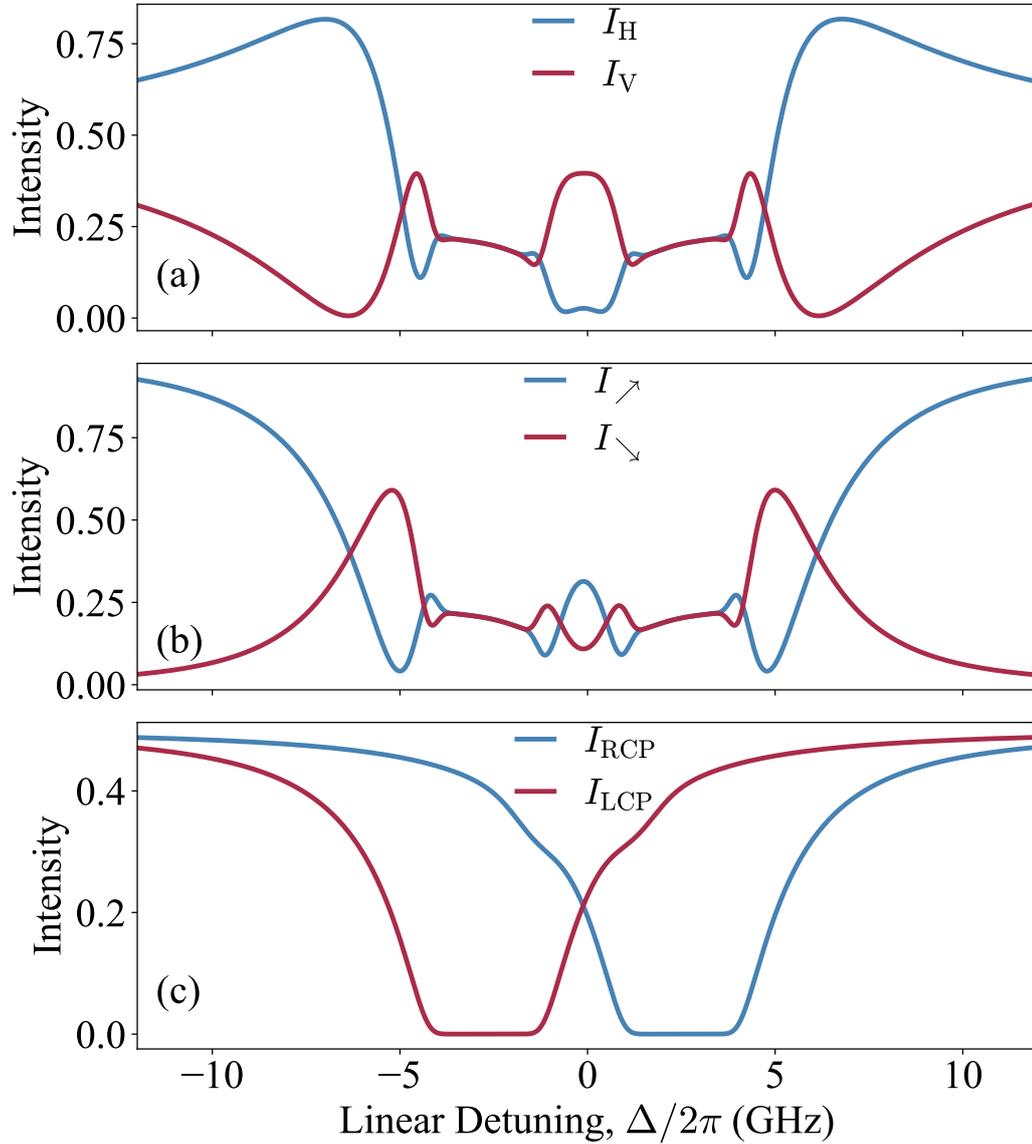
Figure 3.14: Calculated transmission spectra for Stokes parameter measurements in K D1 vapour cell at $B=$ 1160 G and $T=$ 393 K. (a) Linear H/V polarisations, (b) diagonal/anti-diagonal components, and (c) RCP/LCP polarisations.

Stokes parameter	GT2 angle (°)	Intensity measurement	$\lambda/4$ present
S_1	0	I_{H}	No
S_1	90	I_{V}	No
S_2	+45	$I_{\nearrow}$	No
S_2	−45	$I_{\searrow}$	No
S_3	+45	I_{RCP}	+45
S_3	−45	I_{LCP}	+45

Table 3.1: A summary of the polarisation analyser configurations required to measure each Stokes parameter component. The GT2 angle indicates the measured angle of the Glan-Taylor polariser with respect to the horizontal axis. The insertion of a quarter-wave plate ($\lambda/4$) at a +45° orientation is only required for the measurement of the circular polarisation (S_3) in order to convert circular polarisation to linear for subsequent analysis.

light polarisation plane along the ± 45° axis as it propagates through the atomic medium. The complicated and oscillatory transmission profiles of these linear components about resonance ($\Delta/2\pi = 0$ GHz) represent the birefringence (and to some extent dichroism) within the vapour, which is induced by the external magnetic field, which causes the differential phase shifts and absorption for orthogonal linear polarisations. Panel (c) illustrates the left (I_{LCP}) and right (I_{RCP}) circular polarisation intensity components, where the normalised difference gives S_3, a measure of circular dichroism in the medium. The strong asymmetry between I_{LCP} and I_{RCP} exhibits the difference in absorption of the circular polarisation states induced by the magnetic field. The strong suppression of I_{LCP} while maintaining the transmission of I_{RCP} and vise versa reflects the extinction characteristics of the $\sigma^{\pm}$ transitions which are described by the imaginary components of the magnetic susceptibility.

CHAPTER 4

Magnetic-Field Angle Control in Rubidium Magneto-Optical Filters

4.1   Introduction

Control of magneto-optical effects have become increasingly important tools for controlling light-matter interactions, particularly in quantum optics research [41, 42, 43, 44]. Common applications of these effects include magnetometry [45, 16], laser frequency stabilization [46], optical isolators [33, 47]. One primary use is creating narrowband magneto-optical bandpass filters [97, 98, 99, 100, 34, 101, 77]

that only allow transmission of light near atomic resonances in the spectrum. Due to their narrow bandwidths and high transmission at specific frequencies, these magneto-optical filters are highly useful in various fields of study including solar monitoring [102, 103, 104, 105, 106], atmospheric LIDAR [107, 108, 109], and ghost imaging [110]. These filters consist of an atomic vapour cell positioned between two crossed polarisers subjected to a magnetic field that causes the polarisation of light to be rotated as it passes through the cell [40], leading to transmission through a second polariser. These atomic filters use atom-light interactions in various configurations, with the most common ones being Faraday [40, 111, 49] where the magnetic field, and light propagation direction, k, are parallel as showing in Figure 4.1, and Voigt filters [37, 112, 113, 114, 115, 116, 117, 118, 119] where the magnetic field and k are perpendicular. Atomic media under these conditions display several propagation eigenmodes, leading to alterations in the profiles generated by these filter geometries. In the Faraday geometry, the eigenmodes are left-hand and right-hand circularly polarised light, whereas in the Voigt geometry, they are linearly polarised light oriented horizontally and vertically.
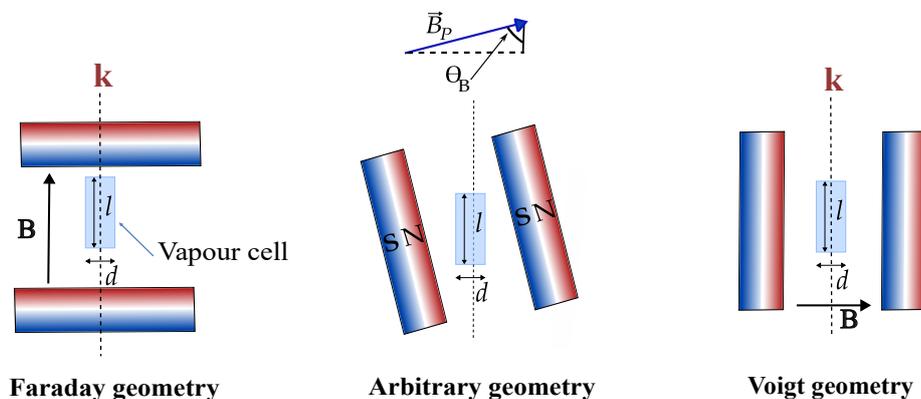
Figure 4.1: A schematic representing the relative orientation of the light propagation direction k and the magnetic field B of (Left) Faraday geometry with magnetic field parallel to k ($\theta_B = 0°$). (Middle) arbitrary angle geometry with magnetic field angle at neither 0 or 90°. (Right) Voigt geometry where B is perpendicular to k light ($\theta_B = 90°$).

The general case with an arbitrary angle between the magnetic field and the axis of propagation is more difficult to treat mathematically – and to optimise exper-

imentally – as the working angular range of the magneto-optical filter is limited and slight deviations from the optimum angle lead to reduced filter efficiency and spectral distortion. Consequently, there are far fewer experimental studies of this case owing to difficulties in setting and controlling the magnetic field angle without encroaching the line-of-sight propagation [120, 121, 122]. Nevertheless, there has been a recent burgeoning of interest in this geometry, as it offers the possibility of realising better magneto-optical filters, when compared to Faraday and Voigt geometries [56, 122]. In particular, the arbitrary angles that have, to date, provided the best single pass magneto-optical filter performance are within the range 80° to 90° with a magnetic field magnitude of several hundred Gauss [56, 123, 124]; this is why we have optimised our device to operate within this parameter range. Ongoing research and development efforts aim to address the experimental challenges and improve the performance, stability, and cost-effectiveness of these devices.

In our previous work involving Rb arbitrary-angle filters [56] the vapour cell length was 5 mm and the magnetic field was controlled using a pair of permanent magnets positioned on either side of the vapour cell, like those used in a Voigt geometry setup, but rotated relative to the beam axis. The field strength was set by the magnet remanence field and separation, while the angle was set by physically rotating the magnets with respect to the k-vector of the laser beam; this concept is illustrated in Figure 4.2 (a).

Ensuring a magnetic field angle (θ_{B}) accuracy of greater than 1° over millimeter-scale vapour cell lengths and maintaining magnetic field homogeneity at the 1% level is considered straightforward [67]. However, the use of these short cells requires increased operating temperatures to create sufficiently high atomic vapour densities that lead to the self-broadening of spectral lines [73] and eventually a decrease of the magneto-optical filter performance [57]. The availability of open-source magnetic field computation programs [125] has made it possible to design bespoke magnetic field profiles with field and θ_{B} homogeneity extending tens of millimeters [92]. This enables the use of standard "off-the-shelf" vapour cells, which
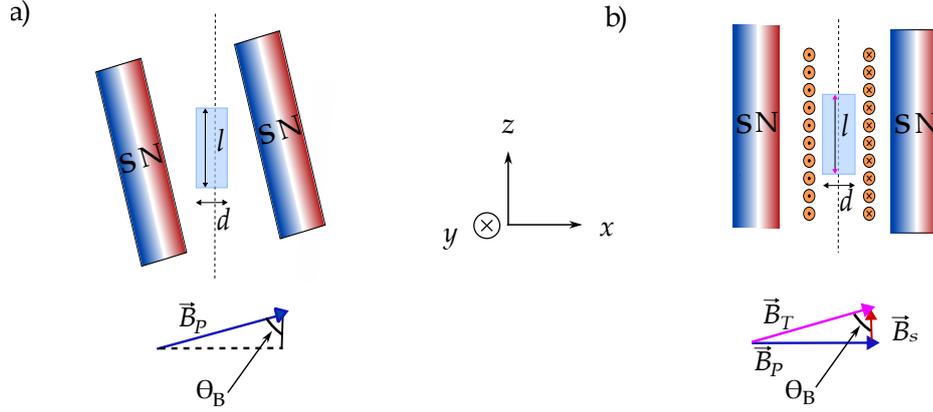
Figure 4.2: An arbitrary magnetic field angle with respect to the axis of the laser beam (i.e. along z), represented by the vertical, black, dashed line, can be produced by either: a) A Voigt magnetic field ($\vec{B_P}$) set-up rotated by θ_B about the y-axis, as shown by the blue vector arrow or; b) A fixed Voigt magnetic field ($\vec{B}_P$, blue arrow) and a tuneable solenoid magnetic field ($\vec{B}_S$, red arrow) produce a combined magnetic field ($\vec{B}_T$, pink arrow) at an angle of θ_B with respect to the z-axis. The red-blue rectangles represent a N-S permanent magnet, while the orange circles represent the solenoid, with either a dot or cross showing the current direction. The light blue rectangle shown in the centre of the magnet arrangements represents a cylindrical atomic vapour cell of length l and diameter d.

have a length of tens of millimeters, and require lower operating temperatures. However, the challenge remains in the precise alignment of the magnetic field vector with the k-vector of the laser beam along the atomic interaction lengthscale, which is defined by the length of the vapour cell. When employing mirror mounts with three-axis control to direct the laser beam and setting up the filter, this complexity is further emphasised. The angular range of an arbitrary-angle filter that employs permanent magnets is physically limited due to the fact that a longer vapour cell needs precise alignment over longer lengthscales and may obstruct a pair of permanent magnets when they are rotated. This limitation becomes greater as the cell's length increases. While it is possible to create custom hardware solutions that achieve a static alignment between the laser beam axis and the magnetic field vector at the optimal angle, this method has its limitations. It restricts the configuration to a fixed set of filter operating parameters and sacrifices tunability.

To resolve these challenges, we propose and implement a novel approach to cre-

ating an arbitrary magnetic field angle while maintaining the same field strength. Our approach involves incorporating an air-core solenoid between a pair of Voigt geometry permanent magnets producing a strong transverse magnetic field, with the vapour cell positioned within the bore of the solenoid. A weak axial magnetic field is generated by the solenoid, and by adjusting the current, both the strength of this field and consequently the angle of the total field can be controlled. This concept is illustrated in Figure 4.2 (b).

In this chapter, we show that combining Voigt-geometry permanent magnets and a Faraday-geometry solenoid successfully addresses the experimental challenges related to accurate control of small magnetic field angles. We will refer to this new method as 'solenoid-plus-permanent', and the old method as 'rotated-permanent'.

4.2 Requirements of the magneto-optical filter

In the magneto-optical filter, the magnetic field vector within the vapour cell lies in the x-z-plane at an angle θ_B to the z-axis. When θ_B is 0° and 90°, the configurations correspond to the Faraday and Voigt geometries, respectively. The vapour cell is placed between two high-extinction crossed polarisers (as shown in Figure 4.3 (ii)). This means that the first polariser is adjusted to transmit one linear polarisation state, while the second is oriented to transmit the orthogonal linear polarisation. For instance, the first polariser might transmit horizontally polarised light, while the second transmits vertically polarised light. Without the vapour cell, there is no transmission, as the light from the first polariser is completely blocked by the second due to the unchanged polarisation during propagation. However, introducing the cell between the crossed polarisers allows the light's polarisation to be modified near the transition resonances. As a result, multiple transmission features appear, corresponding to light whose polarisation has been altered by the cell and partially transmitted through the second polariser. The angle between the electric field vector of the light and the x-axis, θ_E, affects the interaction between atomic transitions and the light's polarisation modes. While the angle of the input polariser, θ_E, can
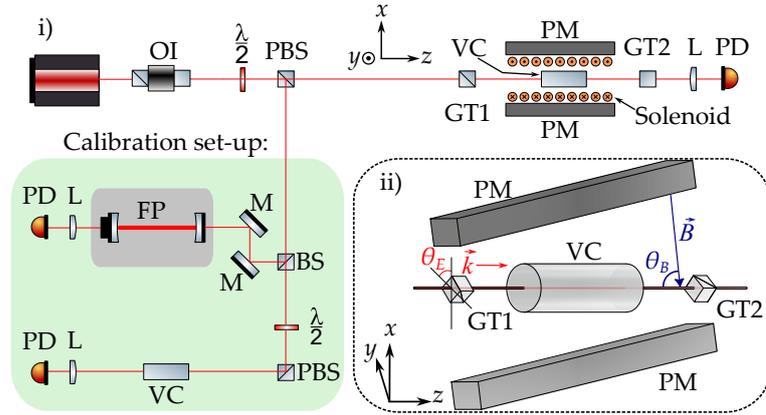
Figure 4.3: i) Schematic of the solenoid-plus-permanent magneto-optical filter set-up and geometry. The filter is an atomic vapour cell in an applied magnetic field ($\vec{B}$) due to two rectangular permanent magnets (PM) and a solenoid. The field strength is controlled by the separation of the magnets up to $190\,\text{G}$, and θ_{B} is controlled by the current through the solenoid. The inset ii) illustrates the magnet set-up for the rotated-permanent set-up. In both configurations, the magnetic field is orientated in the x-z-plane at an angle θ_{B} to the z-axis. An input high-extinction Glan-Taylor polariser (GT1) is placed at θ_E with respect to the x-axis. The output polariser (GT2) is crossed at $90°$ to the input polariser. The transmission of the filter is monitored through the lens (L) and photodetector (PD). Also shown are a Fabry-Pérot (FP) etalon which is necessary for linearising the laser scan and a natural abundance Rb reference vapour cell provides an absolute frequency reference [4, 126].

be adjusted, the relative angle between the two polarisers, GT1 and GT2, is fixed at $90°$.

Using the open-source software *ElecSus* [31, 76], we simulate the transmission of a weak laser beam [24] through an alkali-metal atomic vapour under specified conditions, including the input polarisation, magnetic field strength, and the field's orientation angle. We implement an extension to *ElecSus* to calculates the light's transmission after passing through a crossed polariser, positioned after the vapour cell and oriented orthogonally to the input polariser. This approach enables a more detailed analysis of the filter's performance. Additionally, a fitting routine can be incorporated to optimise key filter characteristics, such as peak transmission and linewidth. This is achieved by adjusting input parameters, including the vapour temperature, the strength of the magnetic field, and the angle of the magnetic field

ElecSus fit parameters:
$\theta_B = (86.7 \pm 0.5)°$
$\theta_E = (9.4 \pm 0.5)°$
$|B| = (191 \pm 1)$ G
$T = (368.2 \pm 0.1)$ K
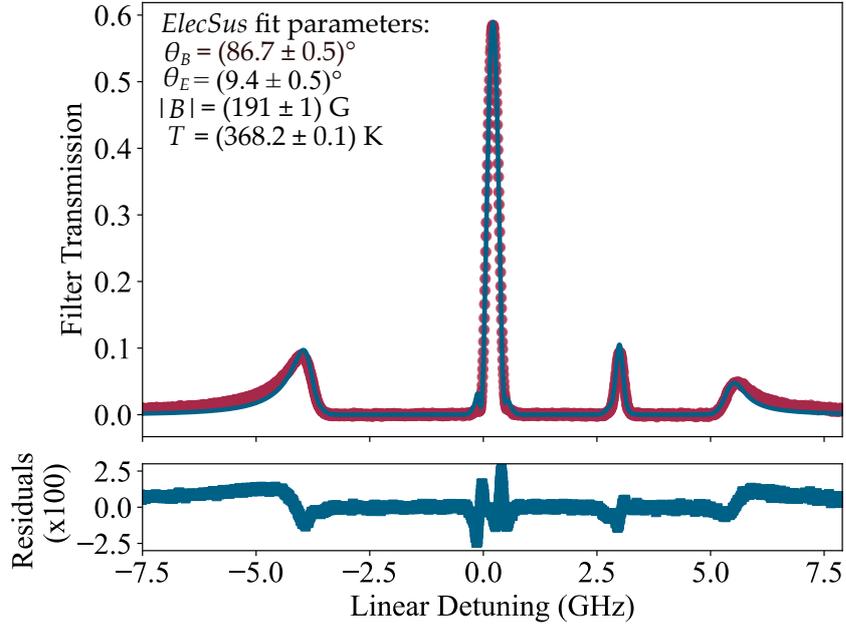
Figure 4.4: Experimental D2 transmission spectra of a 75 mm Rb vapour cell (blue data points) as a function of linear detuning of an arbitrary angle magneto-optical filter. The magnetic field angle θ_B was produced by rotating permanent magnets, as shown in Figure 4.3 (a) ii). A theoretical *ElecSus* fit (red solid line), with corresponding residuals, is shown. The four transmission peaks arise from hyperfine transitions of ^{85}Rb and ^{87}Rb isotopes, further split by the Zeeman effect under the applied magnetic field.

relative to the polarisation axis.

In previous research [56], the optimal magnetic field strength, angle, and atomic vapour temperature were determined for a rubidium (Rb) D2 line filter with natural isotopic abundance, using a 5 mm-long vapour cell. However, in this present work, the magneto-optical filter parameters were not fine-tuned for maximum performance. Instead, the parameters were systematically selected to ensure stable and reliable operation with a 75 mm-long vapour cell, as the primary objective of this research is to compare two methods of generating arbitrary magnetic fields, rather than optimising filter characteristics. Using *ElecSus*, we identified magnetic field parameters that produced a filter profile with a narrow peak and adequate transmission at the line centre for the longer vapour cell. Based on these simulations, a magnetic field strength of 190 G and an angle θ_B of 86° were chosen. These
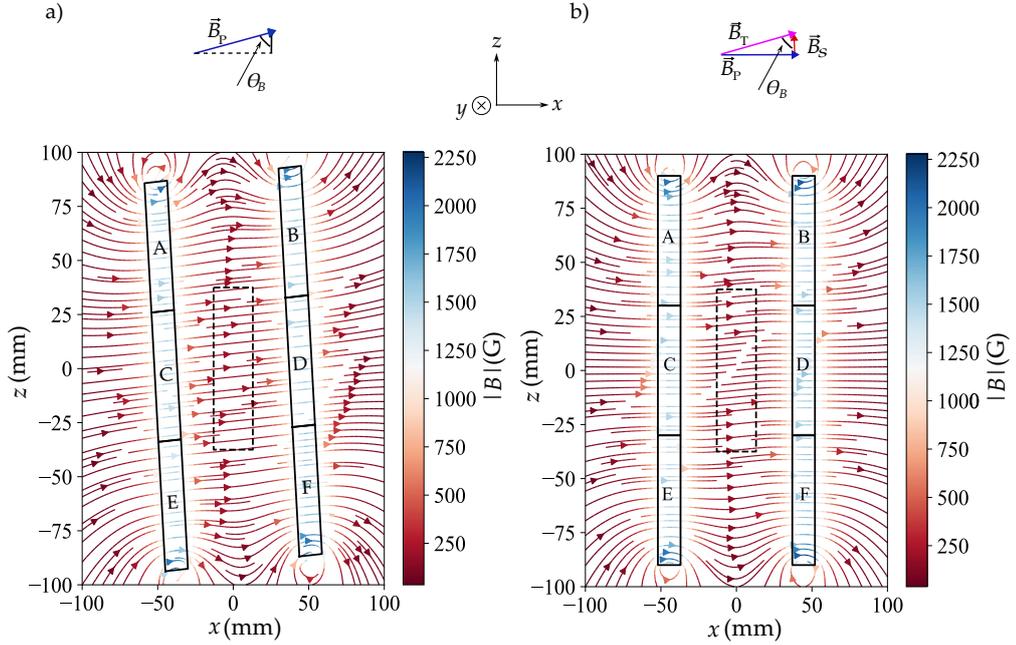
Figure 4.5: *Magpylib* magnetic field simulations for the magnetic field configurations shown in Figure 4.2 for six permanent magnets labelled A-F. The physical profile of each individual magnet is shown by a black solid line in the contour plots and the field strengths of each magnet, which vary by 5% between the weakest and strongest, are accounted for in the *Magpylib* model. The arrows indicate the magnetic field vector's direction, while the colour, and accompanying colour bar, represent the magnitude of the magnetic field. a) rotated-permanent configuration – Voigt permanent magnets rotated by an angle $\theta = 4°$. b) solenoid-plus-permanent configuration – Voigt configuration permanent magnets, and a solenoid current of 525 mA, which generates a B-field along z of 13 G. The physical profile of the solenoid wires are not displayed in the contour plot.

parameters not only deliver a well-defined filter profile but also conform to the allowable angle constraints imposed by the rotated-permanent magnet configuration used in this study.

We construct a magneto-optical filter using the rotated permanent magnet configuration, with its normalised transmission presented in Figure 4.4. The atomic vapour cell was maintained at a temperature of 368 K during the experiment. The experimental results are represented by red data points, while a theoretical fit to the data, generated using the *ElecSus* model, is depicted as a solid blue line. The fitting parameters used are indicated in the figure for reference. The residuals

are plotted below the transmission curve, illustrating excellent agreement between the theoretical model and experimental measurements. Consistent with prior findings [56, 124], the results confirm that the *ElecSus* model accurately captures the behaviour of the magneto-optical filter under these conditions. This agreement highlights the model's reliability in describing the system's response. Furthermore, we will use this model later in the study to evaluate the performance of our novel method for generating arbitrary-angle magnetic field.

4.3   Arbitrary-angle magnetic field control

In this section, we will analyse and compare the magnetic field profiles of two configurations: the rotational permanent magnet setup (Figure 4.2 (a)) and the solenoid-plus-permanent magnet setup (Figure 4.2 (b)). Assessment of field uniformity and tolerances will be of greater interest. Considering the configuration of a solenoid plus a permanent magnet, a $13\,\mathrm{G}$ axial magnetic field must be generated by the solenoid over a length of $l = 75$ mm in order to achieve an angle $\theta_\mathrm{B} = 86°$ of the magnetic field.

The simulation of the magnetic field geometry are performed using *Magpylib* [125], a free-to-use Python package for computing magnetic fields. To generate the required field strengths for the magneto-optical filter described in Section 4.2, we employed "off-the-shelf" commercially available strontium ferrite permanent magnets of grade Y30BH, as detailed in Section 3.2.

The simulation results for the rotated-permanent configuration done in *Magpylib* are shown in Figure 4.5 a). The arrows represent the direction of the magnetic field vectors while the field strength is represented by a colour which includes a colour bar. The black dashed lines between the Voigt magnets show the physical profile of the vapour cell ($l = 75$ mm).

Figure 4.5 (b) shows a *Magpylib* simulation of the solenoid-plus-permanent configuration, with a solenoid current of 525 mA. For both the lower and upper limits

of the vapour cell along the z-axis ($+37.5$ mm $> z > -37.5$ mm) where ($x = 0$, $y = 0$), the magnetic field magnitude and direction for this configuration is the same as for the rotated-permanent configuration. The theoretical curves in Figure 4.9 clearly demonstrate this alignment.

Using *Magpylib*, we additionally simulate how changes in θ_B affect the uniformity of the magnetic field magnitude along the axis of the vapour cell ($x = 0$, $y = 0$, $z = z'$) for both configurations. The results indicate that the solenoid-plus-permanent configuration is much better in terms of uniformity of $|B|$ along the length of the vapour cell. As an example, in the case that is presented in Figure 4.6, at $\theta_\mathrm{B} = 80°$, the contrast between the maximum and minimum magnitudes of the magnetic field for the solenoid-plus-permanent configuration had a value of 2.5 G, while for rotated-permanent setup it was 10 G.
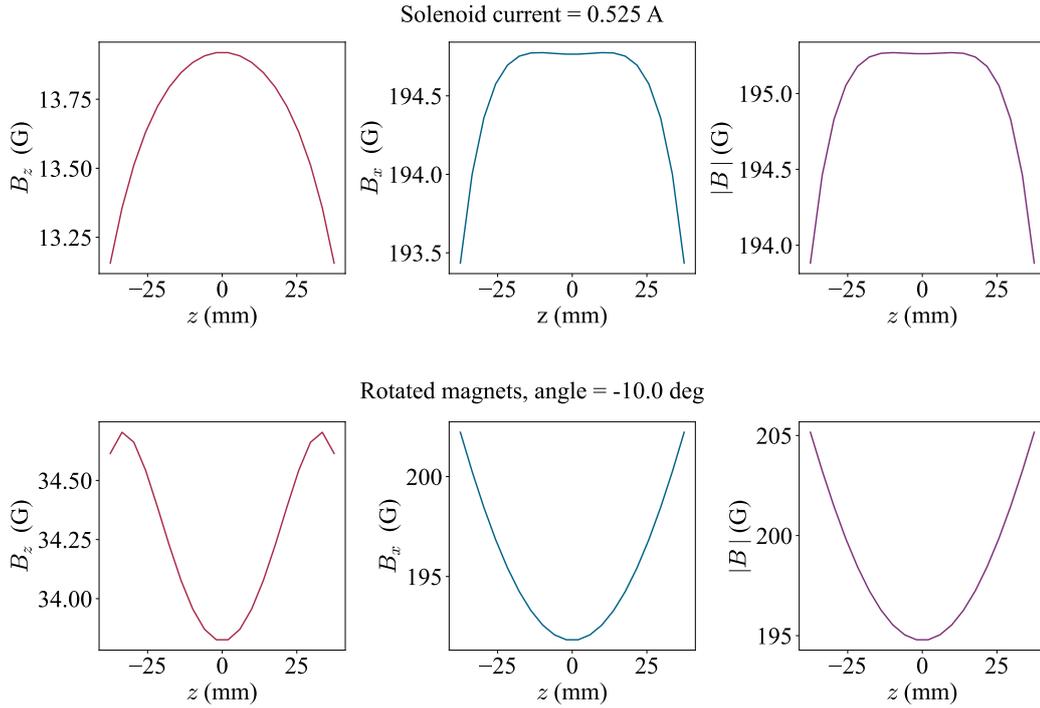
Figure 4.6: Comparative analysis of magnetic field extremes: solenoid-plus-permanent configuration with rotated-permanent configuration at large angle, $\theta_\mathrm{B} = 80°$, along the propagation axis ($x = 0$, $y = 0$, $z = z'$). The solenoid-plus-permanent setup shows better uniformity in $|B|$, with a variation of 2.5 G compared to 10 G in the rotated case.
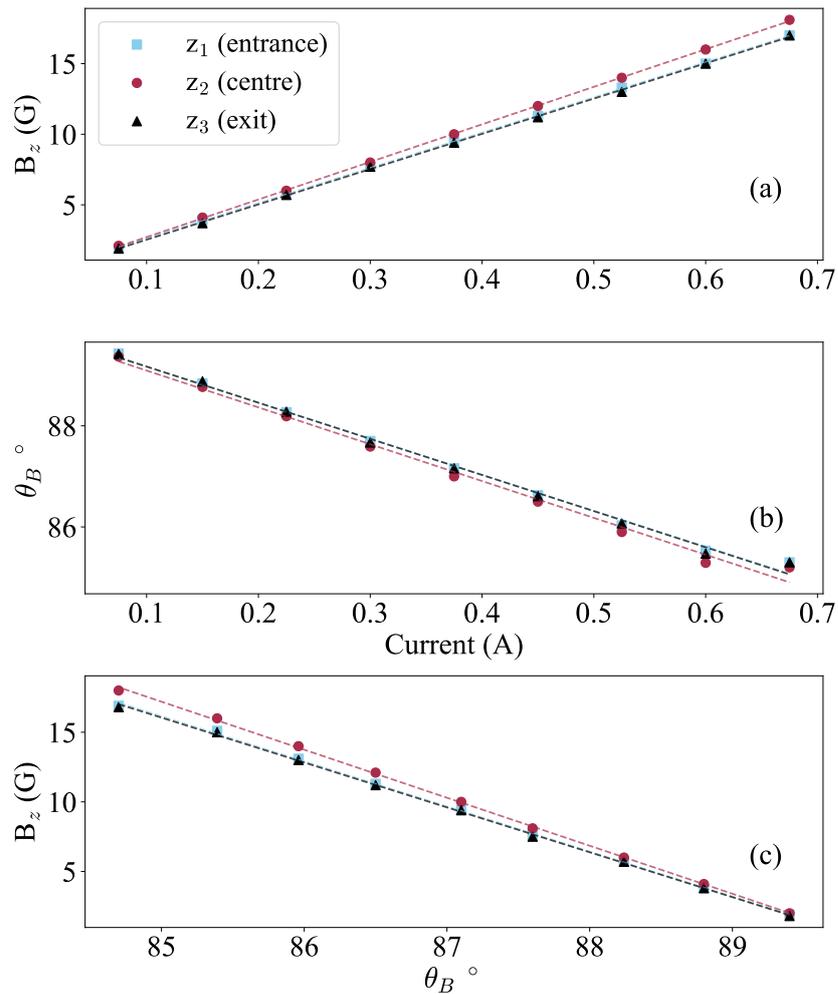
Figure 4.7: Magnetic field characterisation. (a) Solenoid currents vs. the axial magnetic fields at three positions, (b) solenoid currents vs. magnetic field angles, (c) rotated magnetic field angles vs. the axial magnetic field.

4.4 Results

In this section, we examine both approaches for generating an arbitrary-angle magnetic field using two methods. The first involves measuring the axial and transverse components of the magnetic field using a Hall probe, while the second uses atoms as magnetic field sensors within the magneto-optical filter.
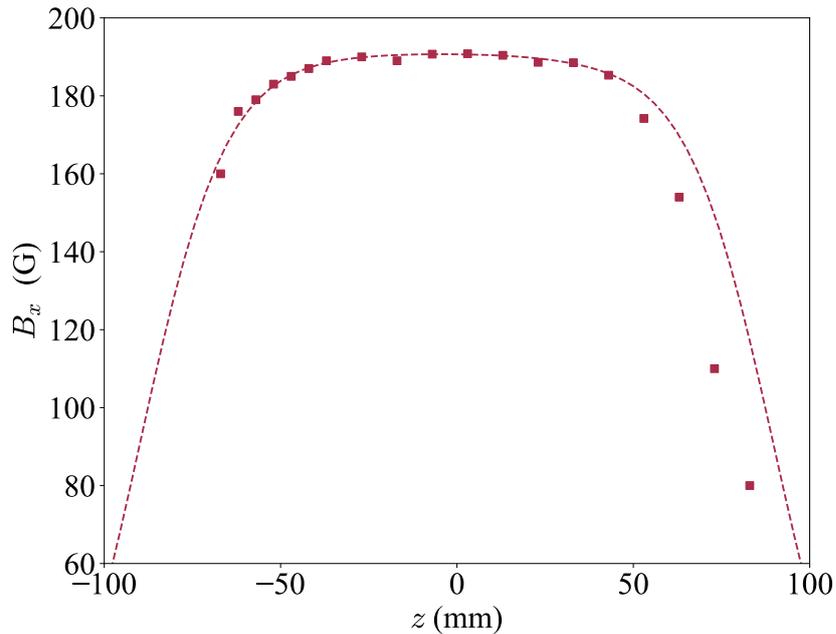
Figure 4.8: Comparison of modeled and measured values for (B_x) in the rotated-permanent setup when one magnet is significantly weaker than all the other magnets. There is a difference between the experimental results and predictions from the theoretical model.

4.4.1 Magnetic Field System Validation

Prior to optical measurements, the magnetic field system had been characterised to ensure reliable operation and to create calibration links. The axial magnetic field component (B_z) was measured at three points in the 75 mm cell (entrance, centre, exit) by a Hall probe, which exhibited good linearity within its current range of 0.075 A to 0.675 A and showed satisfactory uniformity along the cell's axis as shown in Figure 4.7 (a). Linear fits to the data yielded calibration factors of 25.0 ± 0.1 G/A, 26.6 ± 0.1 G/A, and 25.0 ± 0.2 G/A for the entrance, centre, and exit positions respectively, with an average of 25.5 ± 0.1 G/A for the solenoid magnetic field production. Angular response was determined by measuring both transverse and axial magnetic field components to determine $\theta_B = \tan^{-1}(B_z/B_x)$. Increasing solenoid current from 0.075 A to 0.675 A caused gradual angular variation from 89.5 ° to 84.5 °, thus showing effective control within the critical 5° range required for filter optimisation. The angular calibration yielded slopes of
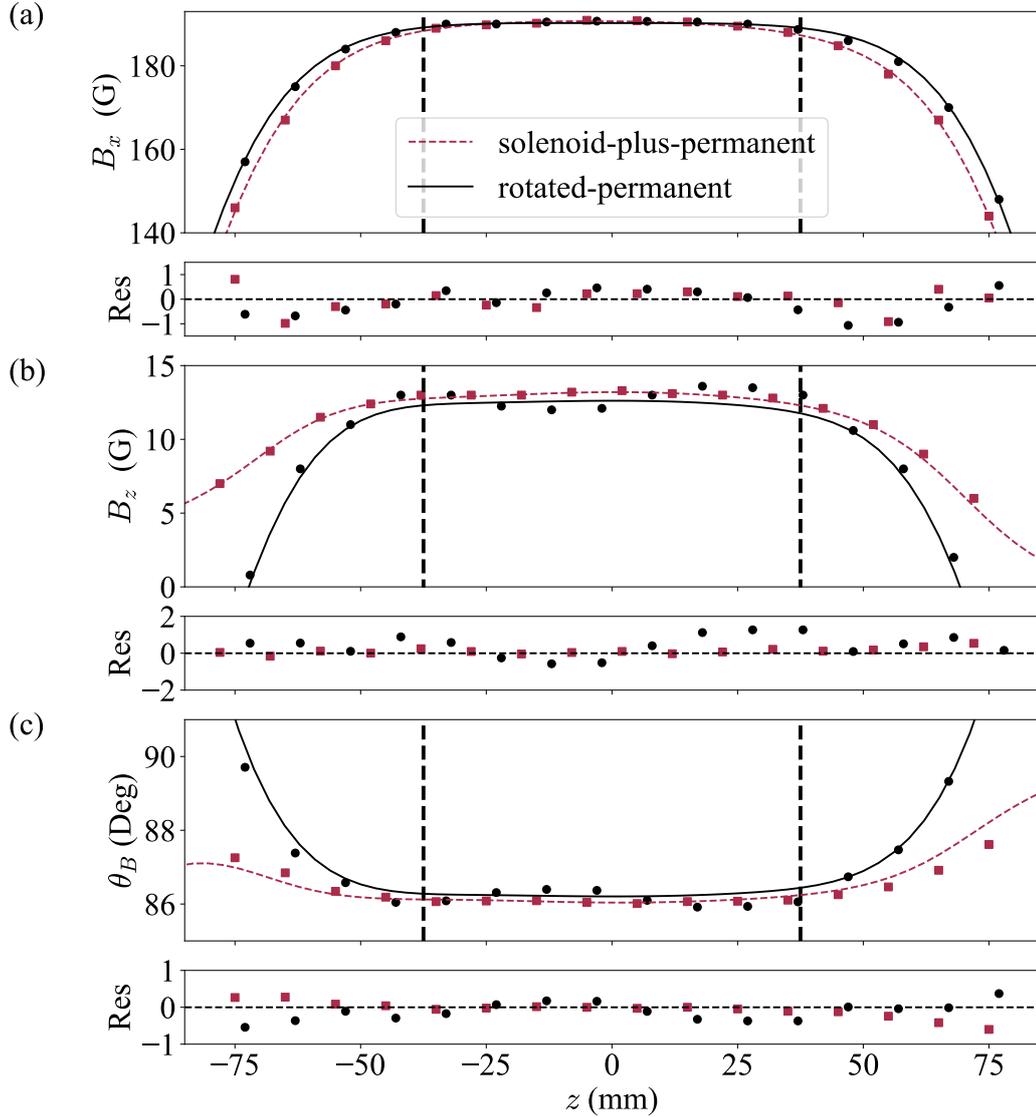
Figure 4.9: Comparison of measured magnetic field components: (a) The transverse magnetic field (B_x) is plotted for the two different methods: solenoid-plus-permanent (red squares), and rotated-permanent (black circles). Each configuration is accompanied by its theoretical model: red dashed line for solenoid-plus-permanent and black solid line for rotated-permanent geometry. Both methods yield comparable, uniform fields of 190 G over the position of the vapour cell, indicated by vertical black dashed lines. (b) The axial magnetic field (B_z) for the two configurations is plotted with a measure of 13 G over the length of the vapour cell. (c) θ_{B}, the angle of the magnetic field vector with respect to the z-axis. The values in (a) and (b) are used to calculate this angle. For both configurations, θ_{B} is approximately 86°. The residuals shown below each subplot demonstrate remarkable agreement between the measured data and theoretical model predictions [127].

-7.1 ± 0.2 °/A, -7.3 ± 0.2°/A, and -7.2 ± 0.2 °/A for the three positions, with an average of -7.2 ± 0.1 °/A, indicating that each ampere of current change produces approximately -7.2 ± 0.1 °/A of angular adjustment. From these measurements, we determined that a magnetic field angle of 86° with an axial field strength of 13 G could be achieved at a solenoid current of 0.5 A, providing an optimal operating point for subsequent filter measurements. Figure 4.7 (c) show comparative measurements carried out on a rotated permanent magnet's structure, where the x-axis represents the rotation angles of the permanent magnets and the y-axis shows the corresponding B_z. This configuration exhibited similar strength, uniformity of the magnetic field of the Faraday geometry, confirming the validating of the solenoid-plus-permanent-magnet approach. The rotated magnet calibration showed slopes of approximately -3.2 ± 0.05 G/°, -3.4 ± 0.05 G/°, and -3.2 ± 0.05 G/° for the three positions, with an average of -3.3 ± 0.04 G/°. These calibration measurements yielded reproducible current-angle correlations, which are needed to make precise filter adjustments. Also, they gave validation concerning the operation of the magnetic field arrangement for future optical measurements.

4.4.2 Hall probe measurements

A transverse Hall probe (Magnetic Instruments GM08 Gaussmeter) measures the transverse magnetic field profile, B_x, along the axis of the laser beam (z-axis). Variations between the experimental field data and the predicted field profile were observed with the rotated-permanent configuration in initial tests, as illustrated in Figure 4.8. To identify potential sources of error, a transverse Hall probe was employed to measure the strength of each magnet. One of the magnets was noted to have significantly lower field strength than the others. Replacing this weak magnet with one that matches the required strength improved agreement between experimental and theoretical data, resulting in a satisfactory experimental field profile aligned with the theoretical predictions.

Figure 4.9 (a) presents the magnetic field profiles measured experimentally for

both configurations, the rotated-permanent setup (black) and the solenoid-plus-permanent setup (red). The profiles are plotted as functions of z and the theoretical predictions calculated with $Magpylib$ are shown with solid and dashed lines in the respective colours. It is important to highlight that both configurations showed the same maximum transverse magnetic field of 190 G in the region of the vapour cell, as marked with black dashed lines. A small difference in field uniformity was observed for the two configurations. The solenoid-plus-permanent setup had an RMS variation of 1.5% in B_x whereas the rotated-permanent showed a lower RMS variation of 0.7%. Regardless of these variations, the residuals present good agreement between the experimental data and $Magpylib$ models.

The results in Figure 4.9 (b) are obtained using an axial Hall probe to measure the axial component of the magnetic field B_z. The two methods gave similar outcomes whereby the strongest field amplitude measured was 13 G, which was expected. In the case of the solenoid-plus-permanent configuration, the field RMS variation of the axial field along $x = 0$, $y = 0$, $z = z'$ was found to be less than 4% for the entire length of the vapour cell. In comparison, the rotated-permanent configuration showed an even larger RMS deviation of 13%. The residuals show agreement between the experimental measurements and the theoretical predictions, which confirms the uniformity of the magnetic field along the length of the vapour cell.

The magnetic field angle, θ_{B}, was obtained for both configurations with the formula $\tan^{-1}(B_x/B_z)$. The results in Figure 4.9 (c) show that for both configurations, approximately 86° was observed for θ_{B}. The corresponding values computed for the solenoid-plus-permanent configuration show that the RMS variation in θ_{B} is 0.2°, while the rotated-permanent configuration exhibits slightly greater variation, 0.6°. The magnetic field magnitude, $|B|$, was calculated using the equation $|B| = \sqrt{(B_x)^2 + (B_z)^2}$. In both configurations, $|B|$ is around 190 G, with solenoid-plus-permanent and rotated-permanent configuration having 1.5% and 0.7% RMS variations, respectively.
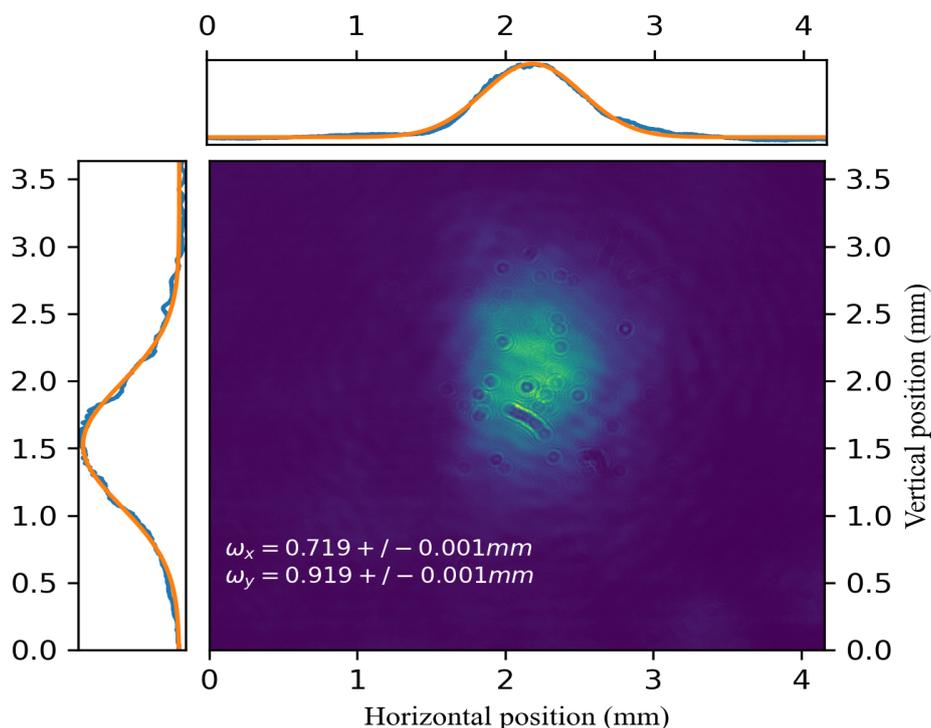
Figure 4.10: Experimentally measured beam profiles which is taken with the CCD camera. The image is taken at the position of the centre of the atomic vapour cell. We fit Gaussian profiles by integrating over each dimension of the image independently illustrate on the bottom and right panels. The orange lines are the lines of best fit, while the blue represent our data.

The slight differences in the transverse and axial magnetic fields are most probably caused by the small inhomogeneities within the individual magnets of the device. Exceeding 1% variation along the central axis ($x = 0$, $y = 0$, $z = z'$) for both transverse and axial fields does exist; however, that variability, which is critical for optimal magneto-optical filter performance as discussed in the Introduction, does not significantly impact the filter. The performance of the filter is still primarily determined by the strength and the angle of the magnetic field, assuming all other parameters are unchanged. In this case, variability of the RMS angle and magnitude of the magnetic field is considered irrelevant because the profile of the filter close to optimal θ_B is essentially insensitive to small deviations up to $0.5°$. This is illustrated in Figure 4.12.

Measurements of the transverse and axial magnetic fields with Hall probes were

confined to the central axis ($x = 0$, $y = 0$, $z = z'$) as the width of the laser beam in our magneto-optical filter is approximately (800 ± 1) μm in both directions x and y, as seen in Figure 4.10. Nonetheless, along a region where $+5$ mm $> x > -5$ mm ($y = 0$, $z = 0$), the *Magpylib* model estimates 3% RMS deviation in magnetic field strength for both configurations. The solenoid-plus-permanent showed 0.2° RMS variation of θ_B while less than 0.1° was observed for the rotated permanent configuration. Again, all these variations of magnetic field angle and magnitude are considered negligible for the current analysis.

4.4.3 Magneto-optical filter measurements

In the previous section 4.4.2, we noticed there are only small differences in the strength and angle of the magnetic field between the two configurations when measuring the strength and angle using a Hall probe. We anticipate the transmission profiles of the magneto-optical filters of these two configurations to be the same. However, since atoms are more sensitive to small deviations of magnetic field strength and angle, we investigate whether we can differentiate between the two configurations. Here, we design magneto-optical filters for both configurations and analyse their transmission profiles. The key experimental parameters for our magneto-optical filter measurements are summarised as follows: we use a Rb vapour cell with length $l = 75$ mm maintained at $T = 368$ K. The magnetic field configuration produces a transverse field component $B_x = 190$ G at $\theta_B = 86°$, and an axial component $B_z = 13$ G, achieved with solenoid current $I = 525$ mA.

Figure 4.11 shows the comparison of the arbitrary-angle magnetic field filter generated with the rotated-permanent magnet configuration and the one created with the solenoid-plus-permanent magnet setup. The difference between the two profiles is shown in the lower subplot. Both methods are shown to be in good agreement with each other in generating the arbitrary magnetic field angle as both methods produced all expected features of transmission [56]. There is some small disagreement at the edges of the central transmission peak, which is due to the narrow
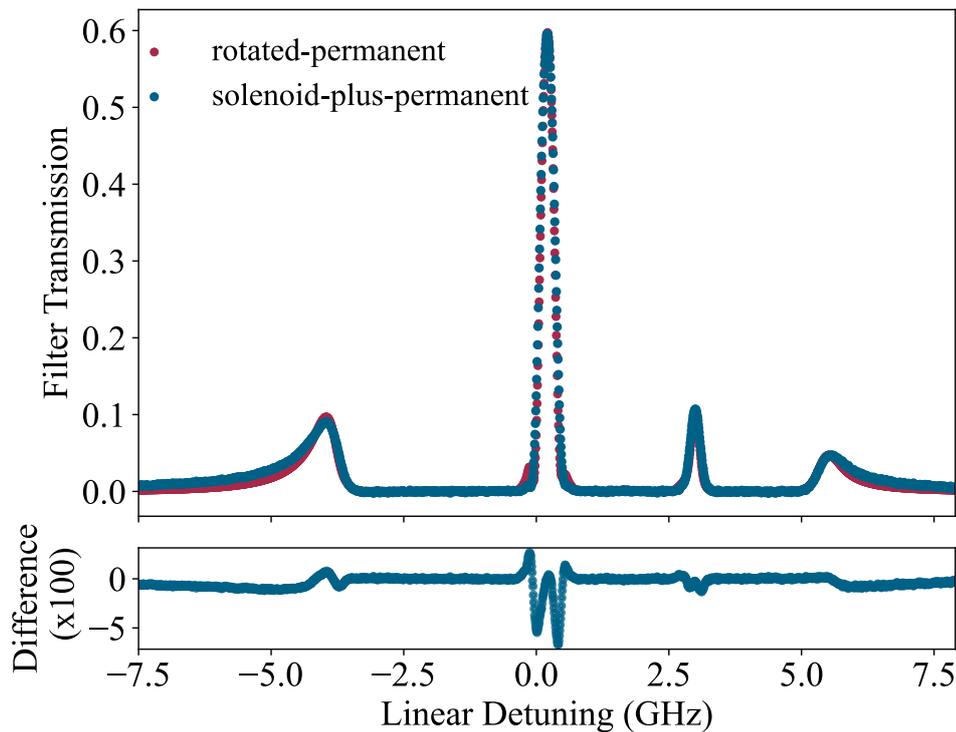
Figure 4.11: Comparison between rotated-permanent (red points) and solenoid-plus-permanent (blue points) filter profiles as a function of linear detuning. The measurements were performed using a 75 mm vapour cell in the weak probe regime at $T = 368$ K. Below is the plotted difference between the two experiments, which demonstrates excellent agreement.

filter transmission profiles. Since these profiles were obtained during separate experimental runs, the magnetic conditions subjected to the atoms were not exactly the same in every experiment. Therefore, the way in which the filter profiles are processed becomes sensitive to small changes such as the linearisation and normalisation procedure, magnetic field angle, or even the magnetic fields for different datasets [4].

The solenoid has a distinct benefit because it allows for quick and efficient tuning of the magnetic field angle. This is unlike the case of a rotated-permanent magnet configuration, where the magnets are physically rotated, which can be a slow process. With a solenoid, adjusting the magnetic field angles can be done quickly just by changing the current supplied to it. Moreover, the solenoid method is easier and more precise in choosing the angle to be set, removing the challenges that come
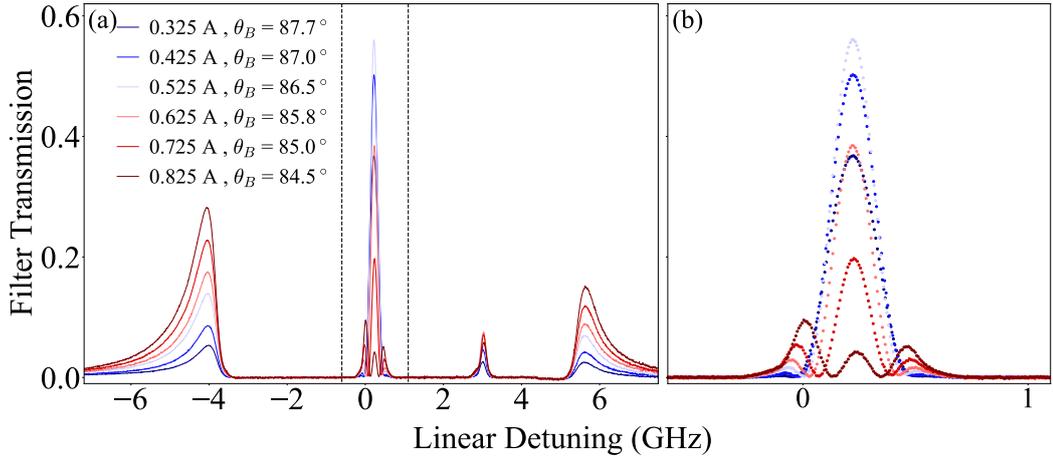
Figure 4.12: a) Experimental Rb D2 line magneto-optical filter transmission through Rb vapour cell of length $l = 75$ mm as a function of linear detuning in the weak probe regime. This plot demonstrates the impact of changing the value of the solenoid current and thus θ_B with respect to the total magnetic field on the filter spectra with the solenoid-plus-permanent configuration. The supplied angles are extracted from *ElecSus*. b) illustrates an expanded view of the central peaks of the spectra. The inset shows theoretical results based on *ElecSus* for FWHM and maximum values of central filter peak with varying angle of magnetic field.
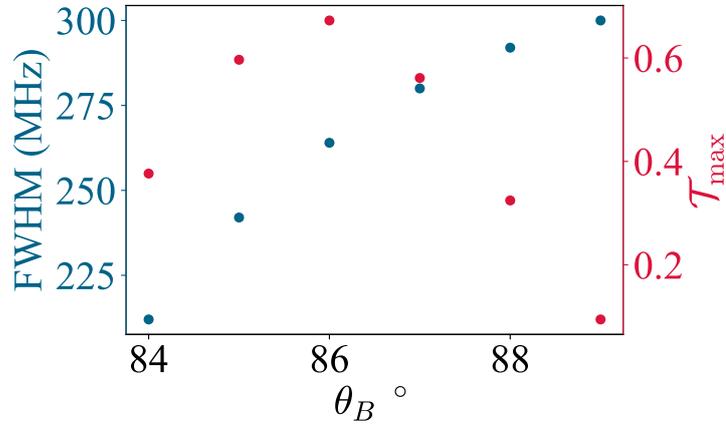
Figure 4.13: Theoretical results based on *ElecSus* for FWHM and maximum values of central filter peak with varying angle of magnetic field.

with trying to adjust the angle using rotated-permanent magnets. All of these improvements make the experimental setup more versatile and responsive.

Figure 4.12 (a) illustrates the varying filter spectra obtained with the solenoid-plus- permanent magnet setup under different solenoid currents, highlighting their
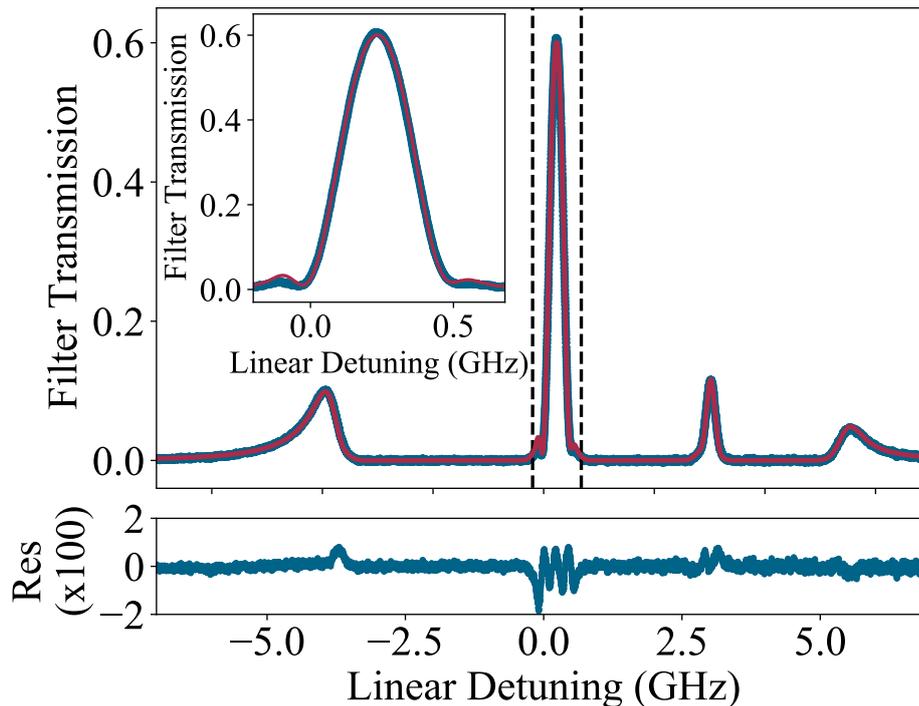
Figure 4.14: Comparison between experimental data for the solenoid-permanent magnet pair (blue line) and theory (red line) for the Rb D2 transitions through a 75 mm vapour cell as a function of linear detuning, $\Delta/2\pi$. The value obtained from the fit was $T = 369$ K, $|B| = 190.8$ G, $\theta_B = 86.6°$ and $\theta_E = 7.8°$. Residuals demonstrate a very good fit for the theory and experiment. The inset shows the zoomed feature of the main transmission peak, demonstrating how closely the properties of this peak track theoretical expectations.

impact on filter properties. The dark blue curve corresponds to the spectrum observed when the solenoid is supplied with a current of 0.325 A. Increasing current leads not only to the rise of the central peak, but also the height of the other peaks.

An interesting change is noted at a solenoid current of 0.625 A (where $\theta_B = 86°$) – the central peak's transmission, which was increasing, begins to decrease, while the wing peaks continue to rise — this is in accordance with theory [123]. The zoomed-in view of the central region shown in Figure 4.12 (b) illustrates the response of the central peak to the varied currents. It can also be observed that the central peak's width always increases as the current increases. Figure 4.13 shows how the central peak's height and width behave as the angle θ_B is changed.

The sensitivity of the magneto-optical filter to slight angle changes further verifies the benefits of using the solenoid-plus-permanent magnet configuration instead of the rotated permanent magnet method. Importantly, this solenoid plus permanent configuration has recently been reported to achieve a high peak transmission with narrow bandwidth recorded for a magneto-optical filter [123]. This measure is significant because high transmission with a narrow bandwidth ensures both efficiency and spectral selectivity, which are essential features for practical applications [122], such as solar monitoring [102, 103, 104, 105, 106], and atmospheric LIDAR [107, 108, 109]. As shown in Figure 4.12 (b), a small angular change in the direction of the magnetic field creates a great variation in the peak transmission, thus strengthening its capability to serve as the foundation for an optical switch [128, 129].

The largest magnetic field angle achieved in this study using the solenoid-plus-permanent magnet configuration was $\theta_B = 84.5°$. However, the available equipment has also been used to generate an angle of $\theta_B = 66°$, with this limitation arising from the specific solenoid characteristics and power supply constraints. A different combination of a solenoid and power supply can easily generate larger values of the axial field component B_z, allowing for smaller θ_B values. In fact, solenoids have been used to generate fields above 4 kG for use in magneto-optical filters, but these experiments require water cooling [49]. Therefore, any desired field orientation could be achieved by using a solenoid-permanent magnet arrangement. Note, however, that in the case of large magnetic field angles using this configuration, the resultant field becomes very sensitive to the field angle.

This large range of achievable angles is in contrast to the rotated-permanent magnet setup which has a physically limit of 70° for the given magnets. In addition, field non-uniformity across the vapour cell becomes a limiting factor well before this angle is reached.

Figure 4.14 demonstrates the results of the solenoid-permanent magnet pair experiment (blue line) with fit (red line). We employ *ElecSus* for the purpose of

predicting suitable parameters; the magnetic field strength and angle, temperature of the cell, and input polarisation angle are floating parameters, allowing for minor imperfections in the experimental configuration. We find excellent agreement between theory and experiment, with an RMS error of 0.3%. The fit parameters $T = 368.15$ K, $|B| = 190.8$ G, $\theta_\mathrm{B} = 86.6°$ and $\theta_\mathrm{E} = 7.8°$.

4.5 Conclusion

In this work, we proposed a new technique for achieving arbitrary magnetic field angles by adding a solenoid to a fixed Voigt geometry permanent magnet pair. This method is more flexible and precise in controlling the magnetic field angle when compared to the previously used method which involves physically rotating permanent magnet pair. We performed simulations using *Magpylib* in order to model the magnetic fields generated by both configurations so that a proper comparison can be made between the two methods. This helped us determine the solenoid-plus-permanent magnet configuration parameters which enabled us to replicate the field behaviour of the rotated-permanent-magnet technique. Experimental data showed strong agreement between both methods for the magnetic field strength and field angle, as well as the filter profiles of the magneto-optical filters.

The main disadvantages of the rotated permanent method arise from its restricted ability in accurately and quickly adjusting the field angle. Moreover, using an extended vapour cell, which is essential for enhancing filter performance, further constrains the range of achievable angles in the rotated-permanent configuration. These problems are fully solved in the solenoid-plus-permanent configuration where the permanent magnets do not move in respect to the cell. That enables the construction of larger angles and the use of longer vapour cells, which gives rise to more efficient magneto-optical filters [36]. In addition, in the solenoid-plus-permanent configuration, the field angle is easily changed by varying the solenoid current, hence providing a straightforward approach to high precision angle tuning. Our findings also indicate that noticeable changes in filter profiles can be observed

with slight changes in the magnetic field angle. The accurate control and flexibility offered by the new design allows for these variations to be utilised more easily.

CHAPTER 5

Influence of Buffer Gas on the Potassium D1 Line Profile

5.1   Introduction

Potassium (K) vapour magneto-optical filters, optimised for the D1 transition $(4S_{1/2} - 4P_{1/2})$ at 769.9 nm, play a significant role in "so-called" solar filters [50, 51, 52, 53, 54]. These solar filters integrate cascaded magneto-optical filters with a telescope for solar observation [55], with the transmission consisting of a single transmission peak centred on the atomic transition [19]. To achieve the necessary filter transmission profile for use in solar studies requires an understanding of how the different magneto-optical filter parameters come into play, as well as precise control over them. Unlike earlier work studying magneto-optical filters in

our group, magneto-optical filters for solar studies require a buffer gas presence to broaden the filter transmission peak. *ElecSus* helps in the theoretical modelling of these parameters [31, 76]. However, as discussed in Section 2.4.3, prior to this study, *ElecSus* was lacking considerations for buffer gas effects, which are crucial for practical filter implementations. To address this limitation, we have implemented a collisional model for buffer gases into *ElecSus*, allowing for accurate prediction of pressure broadening and spectral shifts in the potassium D1 line. This chapter investigates how the presence of neon buffer gas influences the potassium spectral line, particularly how it broadens and shifts the line, as well as how these effects depend on temperature (see Section 2.4.3 for more details).

The pressure broadening (Γ) and shift (S) for alkali-metal vapours has been studied quite extensively over the years [80, 130, 131, 132, 133], frequently employing gas handling techniques to study the dependence of pressure. In this study, we use a different approach by using pre-filled vapour cells, where the amount of gas is fixed at the time of sealing, permitting more detailed studies of the absorption spectra of the potassium D1 line as a function of temperature. We consider a special T-shaped vapour cell, as discussed in Section 3.1, with separate heaters for the body (T_c) and the stem (T_s), allowing independent control to assess the impact of T_c on Doppler broadening and the effect of T_s on vapour pressure and line depth. We also study the effect of neon which causes homogeneous broadening and shifts the frequency of absorption because of increased collision rates. The change from Gaussian to Voigt profile, which is a convolution of Gaussian and Lorentzian profiles, demonstrates the transition from a thermally dominated system to one where atoms collide, altering the width and centre of the absorption line most noticeably. Accuracy in the temperature of the atomic vapour and the magnetic field is critical for these measurements.

Moreover, we study the D1 line of potassium in the hyperfine Paschen-Back (HPB) regime. The strength of the field needed to achieve this regime for potassium is around 165 G [4, 88]. More details about HPB regime can be found in Section 2.6.

In this research, we examine magnetic fields of strengths 700–1200 G. This work is motivated by ongoing projects in our group which involve the development of solar filters and the advancement of potassium spectroscopy [19]. One of the main goals for us is measuring the degree of spectral line broadening and shifts caused by collisions with buffer gases, especially neon, and magnetic fields. It is our intention to further understand these effects in order to improve the design of the filters for magneto-optical instruments and exploit the applications in solar physics by enhancing the filtering and detection precision of the solar observation system.

5.2 *ElecSus* Modification

ElecSus plays an integral role in this thesis by providing a framework to model atomic absorption and polarimetry. The standard release of *ElecSus* allows spectra to be calculated and fitted to experimental data. In its original form, *ElecSus* performs the fit procedure and outputs the best-fit parameters (e.g. temperature, magnetic field, and Doppler width) [31, 76, 77, 78]. However, this functionality alone was insufficient to capture the effects of buffer gases that are central to this work. Therefore, modifications were implemented to extend *ElecSus* so that it could account for collisional effects.

Specifically, the code was modified in the `elecsus_methods.py` script. The fitting procedure was extended to extract the fit parameters and then to apply additional calculations using the approach of Pitz et al. [80]. This adjustment allows the fitted parameters to be converted into physically meaningful quantities such as buffer-gas-induced pressure broadening and line shifts. In particular:

- The **collisional broadening** was included by introducing an additional Lorentzian term (`GammaBuf`), representing the contribution from buffer-gas collisions. The gas broadening was adjusted using temperature scaling laws from Pitz et al. [80].

- The **collisional frequency shift** (`shift`) was incorporated in a similar way, again following the Pitz formalism, so that the total detuning of the line centre is correctly reproduced.

The relevant code excerpts are shown below, corresponding to Eqs. (2.13) and (2.14) in Chapter 2. These snippets demonstrate how the fit parameters are adjusted following the Pitz approach in order to determine the effective pressure and broadening rates.

```
1  # gas broadening (GammaBuf)
2  natwidth = 6.0  # FWHM for Potassium D1 in MHz
3  DoppT = optParams['DoppTemp'] # Doppler temperature
4  Gamma = optParams['GammaBuf'] - natwidth # gas broadening

6  # Values taken from Pitz et al. (2012)
7  RefGammaRateT = 328   # reference temperature
8  RefGammaRate = 6.14   # gas broadening rate at reference temperature
       (MHz/torr)
9  RefGammaRaten = 0.5   # temperature-dependent coefficient

11 GammaRate = RefGammaRate * (RefGammaRateT / (DoppT + 273.15))**
       RefGammaRaten # gas broadening rate
12 PressureGamma = Gamma / GammaRate # pressure
```

Listing 5.1: Implementation of buffer gas broadening in *ElecSus*.

```
2  Shift = optParams['shift']

4  # Values taken from Pitz et al. (2012)
5  RefShiftRateT = 328   # reference temperature
6  RefShiftRate = -1.27  # shift rate at reference temperature (MHz/torr
       )
7  RefShiftRaten = 0.5   # temperature-dependent coefficient

9  ShiftRate = RefShiftRate * (RefShiftRateT / (DoppT + 273.15))**
       RefShiftRaten # shift rate
```

```
10  PressureShift = Shift / ShiftRate
```

Listing 5.2: Implementation of buffer gas shift in *ElecSus*.

These additions mean that the currently available version of *ElecSus* not only performs the fit to experimental spectra but also takes the fitted parameters and adjusts them using the Pitz formalism to recover pressure broadening and shift values. *ElecSus* was modified as part of this thesis work (under supervision from Dr. S. Wrathmall), and this extended functionality was essential for the buffer-gas analysis presented in this chapter.

5.3   Experimental Details

The experimental set-up is shown in Figure 5.1. A laser beam resonant with the K-D1 line divided into two separate beams. One beam is used for laser scan linearisation and frequency calibration using a Fabry-Perot etalon and a 100 mm natural abundance K reference cell. To calibrate the laser scan, we follow the methods described in Section 3.3. The second beam is directed through the main experimental cell for investigating buffer gas effects and Zeeman splitting.

5.3.1   Buffer gas pressure investigation

This study examined the effects of buffer gas on shifts (S) and broadening (Γ) of the potassium D1 line, investigating the impact of vapour cell temperatures and initial buffer gas pressures on the parameters. The experimental vapour cells used in this study had a length of 75 mm.

The potassium vapour cell was heated to a minimum of 313 K in order to obtain measurable absorption of the probe beam with a good signal-to-noise ratio. At this temperature, the atomic vapour density is high enough to obtain significant absorption features. At 313 K, the Doppler width is approximately 800 MHz, which is much larger than the ground-state hyperfine splitting of potassium isotopes (^{39}K
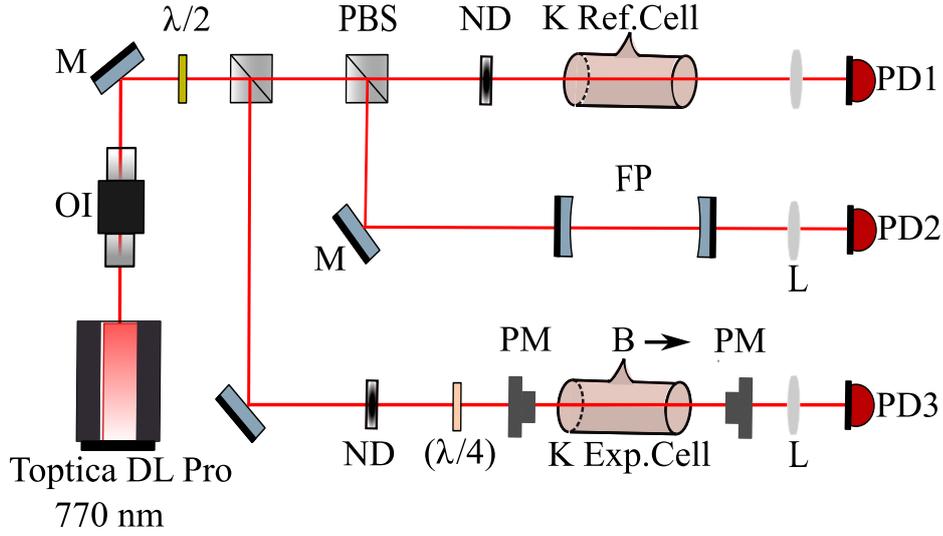
Figure 5.1: Schematic of the experimental apparatus. 770 nm light (K-D1) from a diode laser (DL) passes through an optical isolator (OI) and is split into two paths using a polarising beam splitter (PBS) cube. The first path is directed towards the reference optics includes Fabry-Pérot etalon for relative frequency calibration[4], and 100 mm length buffer-gas free potassium reference vapour cell (labelled "K Ref. Cell" in the figure) for absolute frequency calibration. The transmission through the reference vapour cell is detected on photodiode PD1, while the Fabry-Pérot etalon is detected on photodiode PD2. The other fraction of the beam is used to study the buffer-gas pressure within the vapour cell, the temperature of the vapour cell, and the magnetic field in which the vapour cell is located. This vapour cell is labelled as "K Exp. Cell" in the figure and the transmission is monitored on photodiode PD3. The magnetic field is produced by means of axially magnetised annular permanent magnets [92] which are shown as PM. M: Mirror; ND: Neutral Density filter; L: Lens; λ/2: Half Waveplate; λ/4: (optional) Quarter Waveplate are used for beam steering, size and power control.

at 461.7 MHz and ^{41}K at 254.0 MHz). Therefore, the hyperfine spectrum could not be resolved and only a single Doppler-broadened transmission spectrum is expected for the D1 line, reflecting contributions from the ground state [61]. The experimental results for both the uncoated cell and the anti-reflection coated cell are presented in Section 5.4.

5.3.2 Zeeman-splitting the spectral line

This study focused on the influence of a magnetic field. The field was generated using axially magnetised annular permanent magnets similar to those described in [92] and shown in Figure 3.6, within Faraday configuration, where the magnetic

field was parallel to the *k*-vector. In this configuration, $\sigma^{\pm}$ transitions are driven by left-hand and right-hand circularly polarised light [134]. Since there is no part of the electric field in the direction parallel to the magnetic field, π transitions cannot be excited.

The annular magnets were constructed to fit a vapour cell of length 25 mm (without a stem) and to exhibit an root-mean-square variation of the magnetic field along the length of the vapour cell of about 1-2% at a maximum field of 1.4 kG (a typical value used in solar magneto-optical filters [52]). With the addition of the 6 mm cylindrical stem on the vapour cells, the maximum magnetic field achievable by the annular magnets is about 1.1 kG, with a root-mean-square field variation of 3%.

Instead of using the 75 mm length vapour cell, 25 mm vapour cells (with a stem) were used to make sure that all of the atomic vapour was within the magnetic field. The permanent magnets were positioned on both sides of the vapour cell stem, and the magnetic field strength was reduced by increasing the distance between the magnets. Three different distances between the magnets, and thus three magnetic field strengths, were tested for a vapour cell containing neon gas at a pressure of 60 Torr; this provided a sufficient range of magnetic field strength required to characterise the Zeeman splitting of potassium D1 line.

5.4 Experimental Results

This section discusses the experimental results obtained from spectroscopic studies of the potassium D1 line, focusing on two key aspects: the influence of buffer gas and the impact of an applied magnetic field. Firstly, we examine the effects of neon buffer gas, specifically exploring the broadening, shift, and temperature dependence observed at varying buffer gas pressures. Secondly, we investigate the evolution of the spectral line shape in the presence of a magnetic field, revealing the Zeeman splitting and its dependence on polarisation and field strength. These investigations provide valuable insights into the collisional dynamics and magnetic

properties of the potassium vapour.

5.4.1 Probe intensity investigation

In order to test *ElecSus*, we started with an experimental determination of the weak-probe regime. As shown in Figure 5.2, the line-centre minimum of the spectral line, for a vapour cell at a temperature of $T_c = (358 \pm 5)$ K and $T_s = (341 \pm 5)$ K, is dependent on the incident probe intensity, which is measured relative to the saturation intensity of the D1 transition ($I_{sat} = 1.71$ mW/cm^2) [62]. The temperature was measured with a thermocouple located between the vapour cell and the surrounding metal heater. The results highlight the important effect of optical pumping. At low probe intensity levels, the beam is sufficiently weak to cause noticable optical pumping, meaning that variations in the probe's intensity do not effect the transmission. However, at around I_{sat}, the scattering rate is sufficiently high to noticeably alter the transmission. It is also crucial to highlight that with higher probe intensity, the absorption is lower compared to the weak probe limit. Experimental data, shown in Figure 5.2, indicate that the weak-probe regime lies at probe intensities below around $\sim 10^{-1} I/I_{sa}$, where the transmission is essentially invariant with respect to intensity. The greater uncertainty at lower values is due to the very weak light, which decreases the signal-to-noise ratio on the photodetector.

The blue trace in the inset of Figure 5.2 corresponds to a transmission spectrum within this weak-probe regime. A theoretical model (represented by the black dashed line) is fitted to this spectrum as well as to spectra obtained at higher intensities to demonstrate the effect of optical pumping. The four traces in the transmission plot represent different probe intensities: I_{blue}, I_{red}, I_{purple}, and I_{brown}, which are approximately $\sim (2.88 \times 10^{-3}, \ 7 \times 10^{-2}, \ 1.4 \times 10^{-1}, \ \text{and} \ 3.02) I_{sat}$ respectively. The residuals from the fit outlined in the weak-probe region (blue trace) shows good agreement between the experimental data and theoretical model.
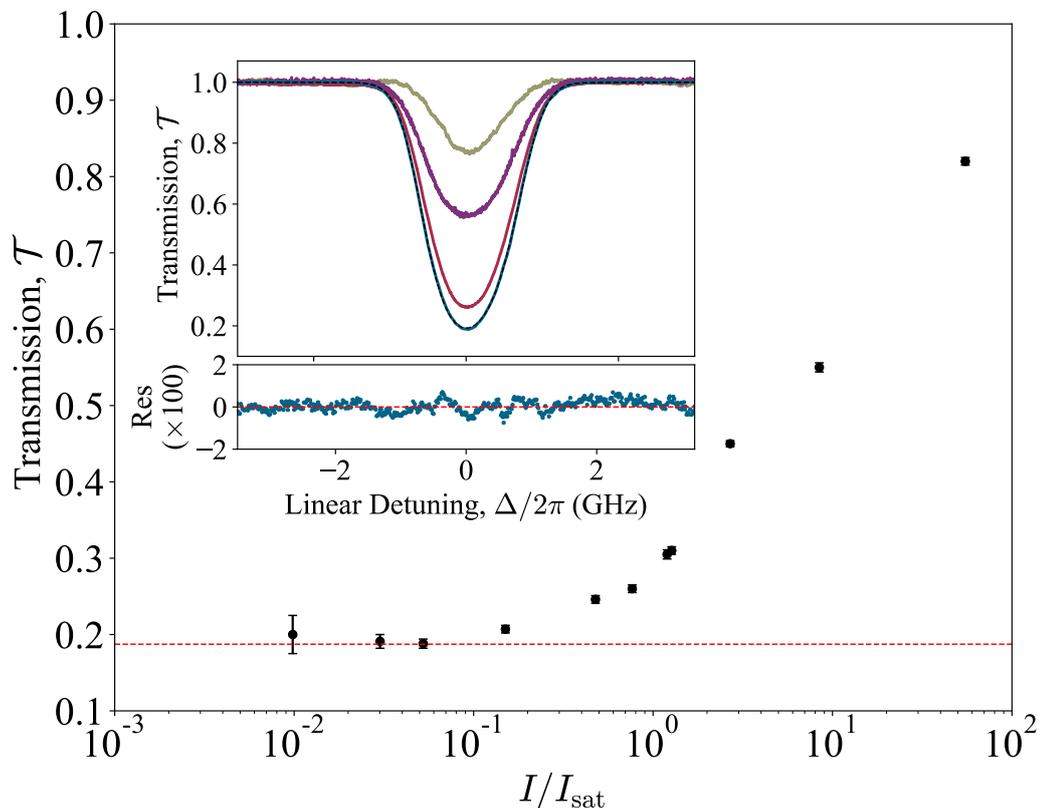
Figure 5.2: The main panel shows the minimum transmission transmission spectra of the potassium D1 line as a function of probe intensity, normalised to saturation intensity, in a 75 mm natural abundance potassium vapour cell. The measurements were taken at a $T_c = (358 \pm 5)\,\mathrm{K}$, and $T_s = (341 \pm 5)\,\mathrm{K}$ with probe beam waists of $(2.75 \pm 0.02)\,\mathrm{mm} \times (2.56 \pm 0.02)\,\mathrm{mm}$. A red dashed line indicates the theoretical prediction from *ElecSus*, and the inset depicts the transmission spectrum as a function of detuning from the centre of the line with the theoretical fit over it shown as a black dashed line. The four traces shown from bottom to top, correspond to different values of probe intensities where I_{blue}, I_{red}, I_{purple}, and I_{brown} representing approximate incident intensities of $\sim (2.88 \times 10^{-3},\ 7 \times 10^{-2},\ 1.4 \times 10^{-1},\ \text{and } 3.02\,)I_{\mathrm{sat}}$, respectively. The residuals for the case of weak probe are shown below the main graph.

5.4.2 Effects of buffer gas on the potassium D1 line: Broadening, shift, and temperature dependence

In this section, spectroscopy in non-AR coated cylindrical vapour cells and AR-coated T-shaped vapour cells are conducted.

5.4.2.1 Spectroscopy in cylindrical non-AR coated cells

We utilised *ElecSus* to fit the experimental spectra, incorporating a differential evolution algorithm to extract the relevant physical parameters. We allowed the temperature, collisional broadening (Γ), and frequency shift (S) to vary during the fit. In this investigation, the spectra were measured using a 25 mm cylindrical non-AR coated potassium vapour cells (described in Section 3.1). Figure 5.3 show measured and calculated transmission spectra of the potassium D1 line as a function of the linear detuning for three different fill pressures of the neon buffer gas: (a) 0 Torr (no buffer gas), (b) 60 Torr, and (c) 100 Torr. The normalised residuals shown below each fit indicate a good agreement between the theory and the experimental data. However, as expected from the cell characteristics discussed in Section 3.1, the interference effects from cells windows are evident in the slightly elevated residuals.

5.4.2.2 Spectroscopy in 75 mm T-shaped AR-coated vapour cells

Figure 5.4 show experimental transmission profiles of potassium D1 line that has been fit with *ElecSus* together with the normalised residuals of the fit shown beneath each main panel as a function of linear detuning. In this investigation, all measurements were taken with 75 mm potassium vapour cells with stem and anti-reflected coatings, under different buffer gas pressures conditions: (a) no buffer gas, (b) 60 Torr, and (c) 100 Torr of neon. During the fitting process, the stem temperature, cell temperature, frequency shift, and line broadening were floated. For each cell, the spectra were collected at six distinct T_s and T_c as shown in Figure 5.4. The stem temperature T_s and cell temperature T_c were both constrained by $\pm 5\,\mathrm{K}$
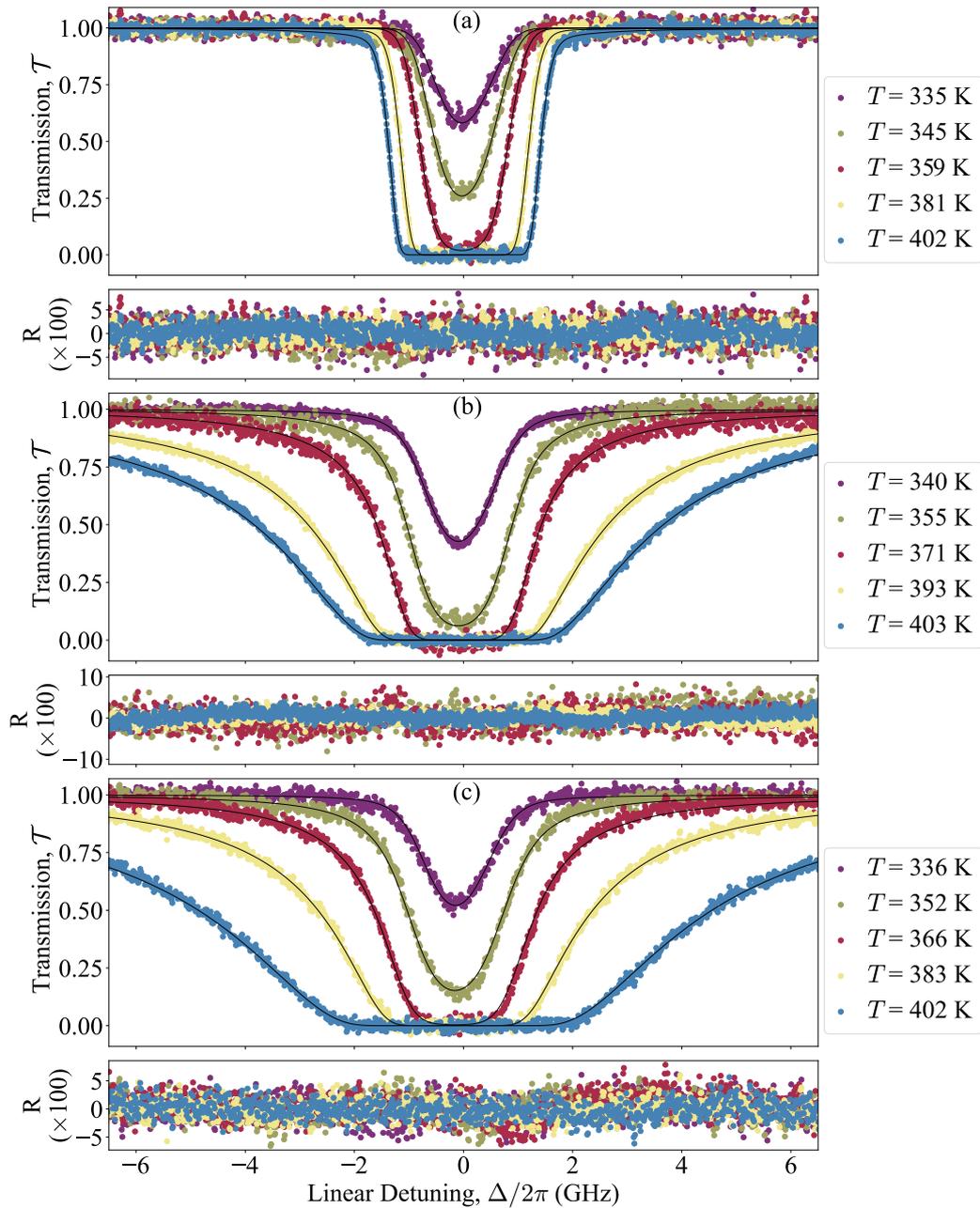
Figure 5.3: Transmission spectra of the potassium D1 line at different temperatures and different buffer gas conditions. Panel (a) for a potassium vapour cell with no buffer gas. Panel (b) for a cell with 60 Torr of neon, and panel (c) for a cell with 100 Torr of neon. In each case, experimental data (coloured markers) are plotted for several temperatures as indicated in the legends, with corresponding theoretical fits shown as solid lines. The presence of buffer gas increases pressure broadening and induces a red shift in the absorption profile, both of which become more pronounced at higher pressures. Residuals are plotted beneath each spectrum show good agreement between the theory prediction and the data.

to allow for determination of the uncertainties in these parameters.

As shown in Figure 5.4 (a), at zero buffer gas and low temperatures, the Voigt transmission profile is Doppler dominated. With increasing temperature, the medium becomes optically thick and the transmission through the medium at line centre is zero. At large detunings (at approximately 1 GHz), the transmission returns to 100%. The presence of neon buffer gas significantly broadened the transmission spectra, with the additional broadening increasing proportionally to the amount of buffer gas. This additional broadening results from collisional interactions of potassium with neon atoms, adding an extra Lorentzian broadening to the Voigt profile. It is clearly noticeable from Figure 5.4 that the Lorentzian broadening increases with increasing pressure and temperatures due to enhanced collision effects. The Gaussian component, determined by Doppler broadening, remained relatively constant. Moreover, the transmission spectra displayed also have a pressure-dependent shift, as shown in Figure 5.5.

From the above results, we confirm that the use of an AR-coated cell with a stem yields spectral results that are easier to analyse. It reduces spurious reflections and etalon fringes which lead to flatter baselines, and improves the fitting accuracy. These features are essential for obtaining the spectral line parameters, such as Doppler and collisional broadening as well as line shifts. This highlights the importance of careful optical design and cell preparation in spectroscopy experiments.

We compared the experimentally determined Γ and S values with theoretical simulations depicted in Figure 2.5, based on the manufacturer's quoted 60 Torr and 100 Torr fill pressures. To check these initial fill pressures, we extracted the broadening and shift parameters from *ElecSus* when we change the cell temperature T_c and applied Eqns. 2.17 and 2.18 with the gas broadening and shift rates (from Pitz *et al.* [80]).

Figures 5.5 (a) and (b) show the measured Γ (black dots) and S (red dots) as a function of T_c for (a) 60 Torr and (b) 100 Torr cells, with theoretical predictions
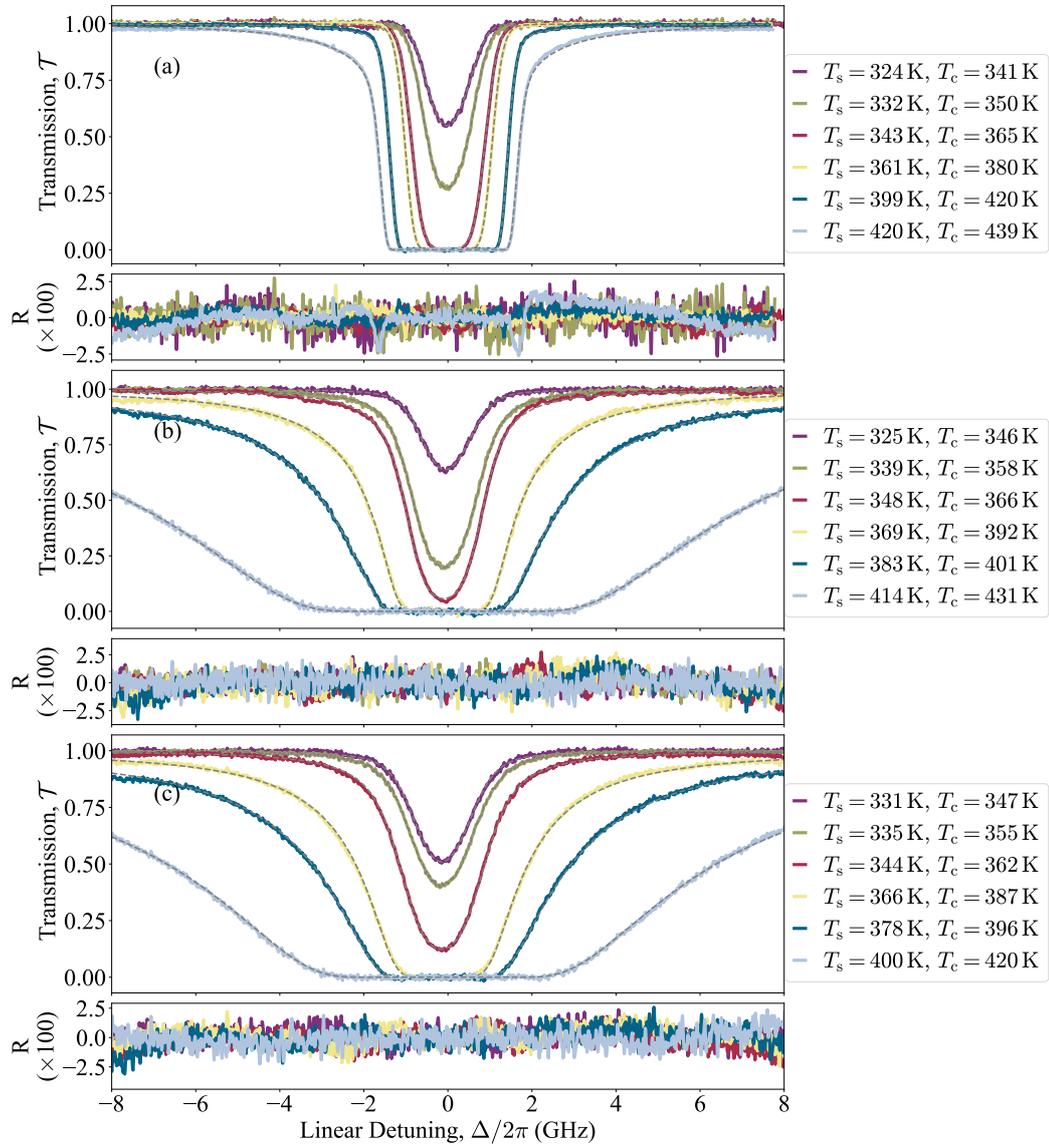
Figure 5.4: Transmission spectra of the potassium D1 line, measured in a 75 mm (AR coating) vapour cells, a at different temperatures and three different buffer gas conditions. Panel (a) for a potassium vapour cell with no buffer gas. Panel (b) for a cell with 60 Torr of neon , and panel (c) for a cell with 100 Torr of neon. In each case, experimental data (coloured markers) are plotted for several temperatures as indicated in the legends, with corresponding theoretical fits shown as solid lines. The presence of buffer gas increases pressure broadening and induces a red shift in the absorption profile, both of which become more pronounced at higher pressures. Residuals are plotted beneath each spectrum show good agreement between the theory prediction and the data.
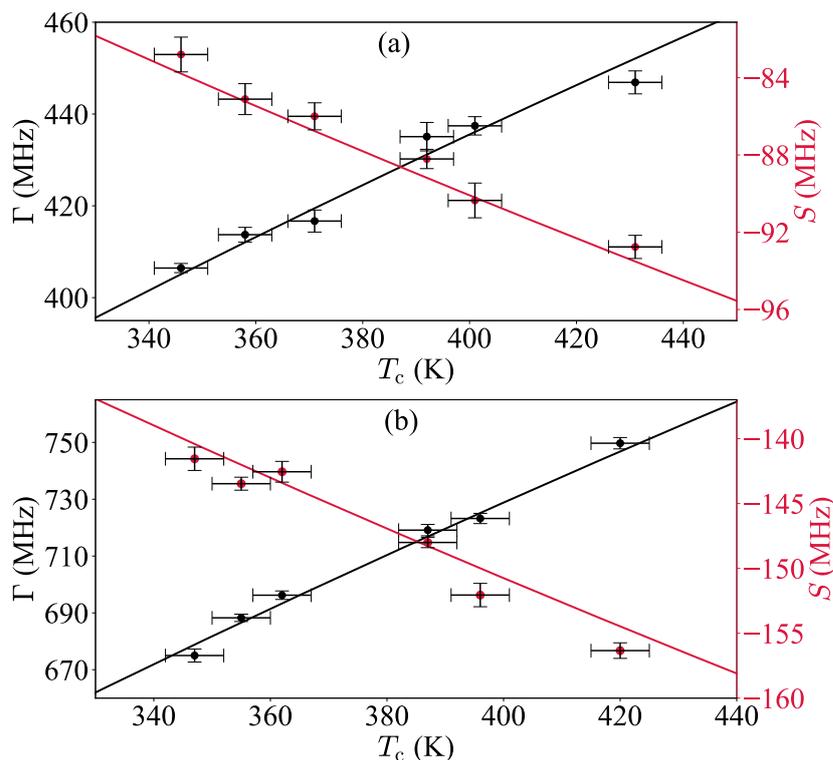
Figure 5.5: Measured Γ (black dots) and S (red dots) values as a function of T_c, with theoretical predictions shown as solid lines. The errors are less than 3% for cells with (a) 60 Torr of neon and (b) 100 Torr of neon.

shown as solid lines. In panel (a), Γ increases from approximately (406 ± 3) to (445 ± 3) MHz while S decreases from (-84 ± 2) to (-93 ± 2) for T_c between 346 to 431 K. In panel (b), measured Γ increases from (675 ± 3) to (750 ± 3) MHz while S decreased from (-141 ± 2) to (-156 ± 2) for the range of T_c between 347 to 420 K. These values show good agreement with the theoretically predicted broadening and shifts. All data points include a cell temperature uncertainty of $\pm$ 5 K.

As discussed in Chapter 2, the ground state hyperfine splitting of potassium is less than the Doppler and pressure width, and hence only one absorption profile is observed. In contrast, the heavier alkali metals rubidium and cesium exhibit more than one line. It is more challenging to extract the individual Gaussian and Lorentzian components to the lineshape in potassium. In these fits, we fix the cell temperature to the value measured by the thermocouple and also constrain the fit range to temperatures within ± 5 K of the thermocouple reading to account

for uncertain offsets between the cell and the thermocouple. In the literature, differences of a few degrees are noted between thermocouple readings and cell temperatures [62]. The calculated fill pressures are presented in Figure 5.6. The buffer gas initial fill pressure, P_i, calculated from the measured values of Γ (blue circles) and S (red squares) – extracted from *ElecSus* – using Eqns. 2.17 and 2.18, as a function of vapour cell temperature, T_c. The upper panel presents the measured initial fill pressure of the 60 Torr cell, while the lower panel shows the measured initial fill pressure of the 100 Torr cell. The mean value of the initial fill pressures were determined to be (57.4 ± 0.6) Torr and (96 ± 1) Torr of neon for 60 Torr and 100 Torr cells, respectively, These calculations assume that the vapour cells are sealed at a temperature of 293 K. These measurements are close to the expected values.

5.4.3 Evolution of the spectral line shape in the presence of a magnetic field

Once the influence of the buffer gas was investigated, we moved on to study the Zeeman splitting of the potassium D1 line. Initially, we studied the dependence of Zeeman splitting on the strength of the magnetic field using linearly polarised light. After that, we analysed the effects of different light polarisation states on the Zeeman spectra at a constant magnetic field. The understanding of the Zeeman shifts and interactions of the various polarisations of light with atomic transitions are essential for the design of magneto-optical filters that find extensive use in solar observations [19, 51] and in other narrowband filtering purposes [18].

5.4.3.1 Linear polarisation spectroscopy of Zeeman splitting at varying magnetic fields

Figure 5.7 demonstrates the transmission spectra of the potassium D1 line measured using a 25 mm vapour cell filled with 60 Torr of neon buffer gas at $T_c = (387 \pm 5)$ K and $T_s = (368 \pm 5)$ K. Spectra were obtained at three distinct mag-
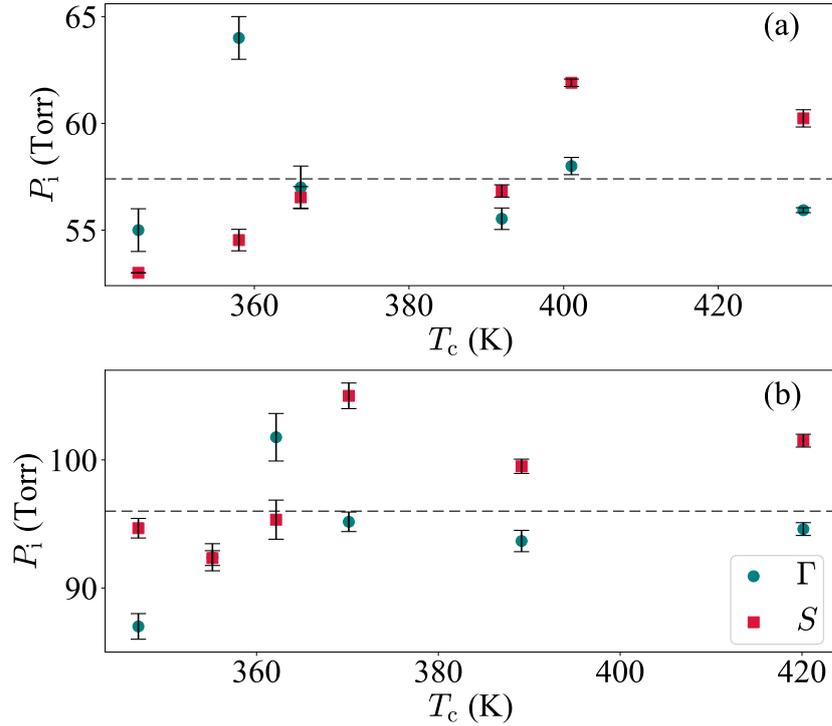
Figure 5.6: Buffer gas initial fill pressure, P_i, calculated from the measured values of Γ (blue circles) and S (red squares) – extracted from *ElecSus* – using Eqns. 2.17 and 2.18, as a function of vapour cell temperature, T_c. The top panel shows the measured initial fill pressure of the "60 Torr" cell, while the bottom panel shows the measured initial fill pressure of the "100 Torr" cell. The dashed lines correspond to the mean values of the initial fill pressures: (57.4 ± 0.6) Torr and (96 ± 1) Torr of neon for the 60 Torr and 100 Torr cells, respectively. Note that the upper and lower limits on T_c were ± 5 K and using these limits, the errors are on Γ and S were calculated.

.

netic field strengths which are determined by fitting the data with *ElecSus*. The extracted magnetic field values are (1200 ± 5) G; (970 ± 4) G; and (750 ± 5) G . The uncertainties in the magnetic field were determined by changing the input light polarisation at a constant field, and fitting the spectra using *ElecSus* accounting for each polarisation state (see Section 5.4.3.2). Theoretical modelling of the magnetic field profile at these three permanent magnet separations (see Section 5.3.2 for more details), yields average field values consistent with experimental results and estimates axial root mean square (RMS) field variations of 3%, 13%, and 23% along the length of the vapour cell, respectively. Despite these variations the spectral fits remained in very good agreement with *ElecSus* confirming with the residuals shown
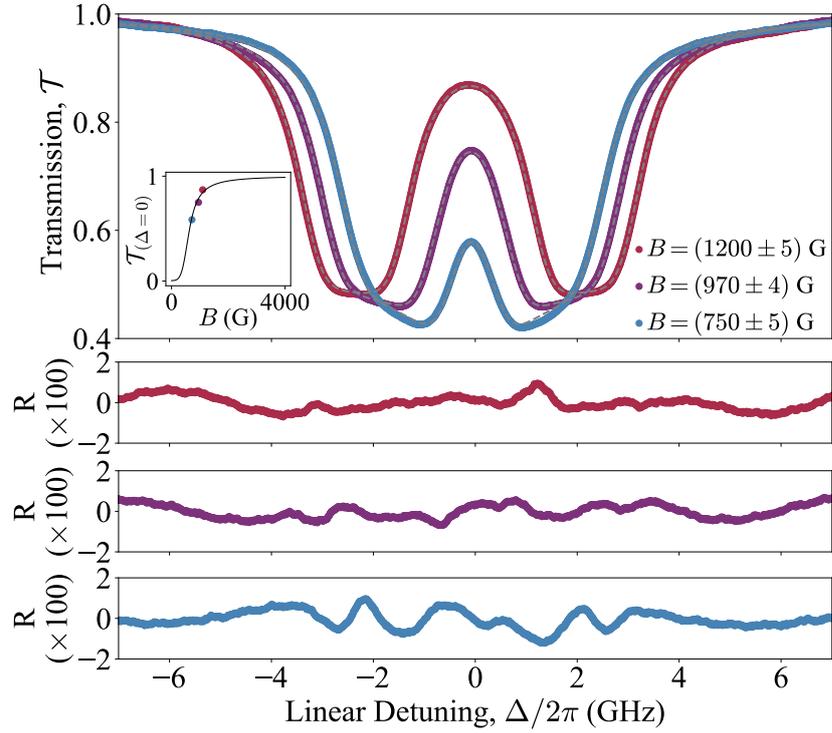
Figure 5.7: Transmission spectra of the potassium D1 line were taken at three varied magnetic field strengths: (1200 ± 5) G (red); (970 ± 4) G (purple); and (750 ± 5) G (blue). The data was acquired with a 25 mm vapour cell filled with 60 Torr of neon while maintaining temperatures at $T_c = (387 \pm 5)$ K and $T_s = (368 \pm 5)$ K. The inset shows the normalised transmission at zero detuning versus the magnetic field, where black solid line represent the theoretical transmission, and dotted marks indicate the experimental transmission values corresponding to the magnetic field strengths obtained from the main figure. The residuals, plotted under the given curves, demonstrate the agreement between the experimental results and the theoretical fits.

below each panel. Small but noticeable Zeeman splitting occurs at lower magnetic field strength, as does some overlap in the absorption features. Splitting becomes more pronounced as the field is increased to around 900 G, with the spectral features now clearly resolved. At the highest field, peak separation is greatest and the central absorption dip is less pronounced. The Doppler effects and pressure broadening combined lead to spectral line broadening.

The inset displays the normalised transmission at zero detuning as a function of the applied magnetic field. The black line is the theoretical transmission value with changing magnetic field strength with the dots being the experimentally mea-

sured values at the specific field strengths related to the main spectra. The rise in transmission observed at line centre is due to the increasing Zeeman splitting. The residuals shown in the lower panels indicate excellent agreement of the experimental data with the theoretical predictions.

5.4.3.2 Polarisation-dependent Zeeman spectra of potassium D1

In this section, we present the transmission spectra of the potassium D1 line for three distinct input polarisations: linear horizontal (purple), left-hand circularly polarised (which drives σ^+ transitions, red), and right-hand circularly polarised (which drives σ^- transitions, blue). The data were collected using a 25 mm T-shaped potassium vapour cell containing 60 Torr neon buffer gas at three different measured magnetic fields ~ 1200 G, ~ 970 G, and ~ 750 G and three different T_c temperatures for each B.

Figure 5.8 show the transmission spectra for the potassium D1 line at a magnetic field strength of (1200 ± 5) G with three different sets of cell and stem temperatures: $T_c = (361 \pm 5)$ K, $T_s = (340 \pm 5)$ K; $T_c = (381 \pm 5)$ K, $T_s = (361 \pm 5)$ K; and $T_c = (399 \pm 5)$ K, $T_s = (380 \pm 5)$ K. For linearly polarised light, the spectrum shows two nearly symmetric features of absorption which are due to the combined contributions of both σ^+ and σ^- transitions. The left and right hand circularly polarised spectra, on the other hand, show clear separation of absorption peaks that correspond to the Zeeman-shifted transitions of the m_J sublevels. These shifts appear contrary to each other as negative and positive detunings for right- and left-hand circularly polarised light and demonstrate the symmetry of the Zeeman effect. At this magnetic field strength, the separation of the circular features is greater than at lower fields, highlighting the stronger magnetic influence. With increasing temperature, the density of atoms increases which, in turn, deepens and broadens the absorption features because of increased optical density. The spectra are not perfectly symmetric due to the presence of more than one isotope. In particular, a
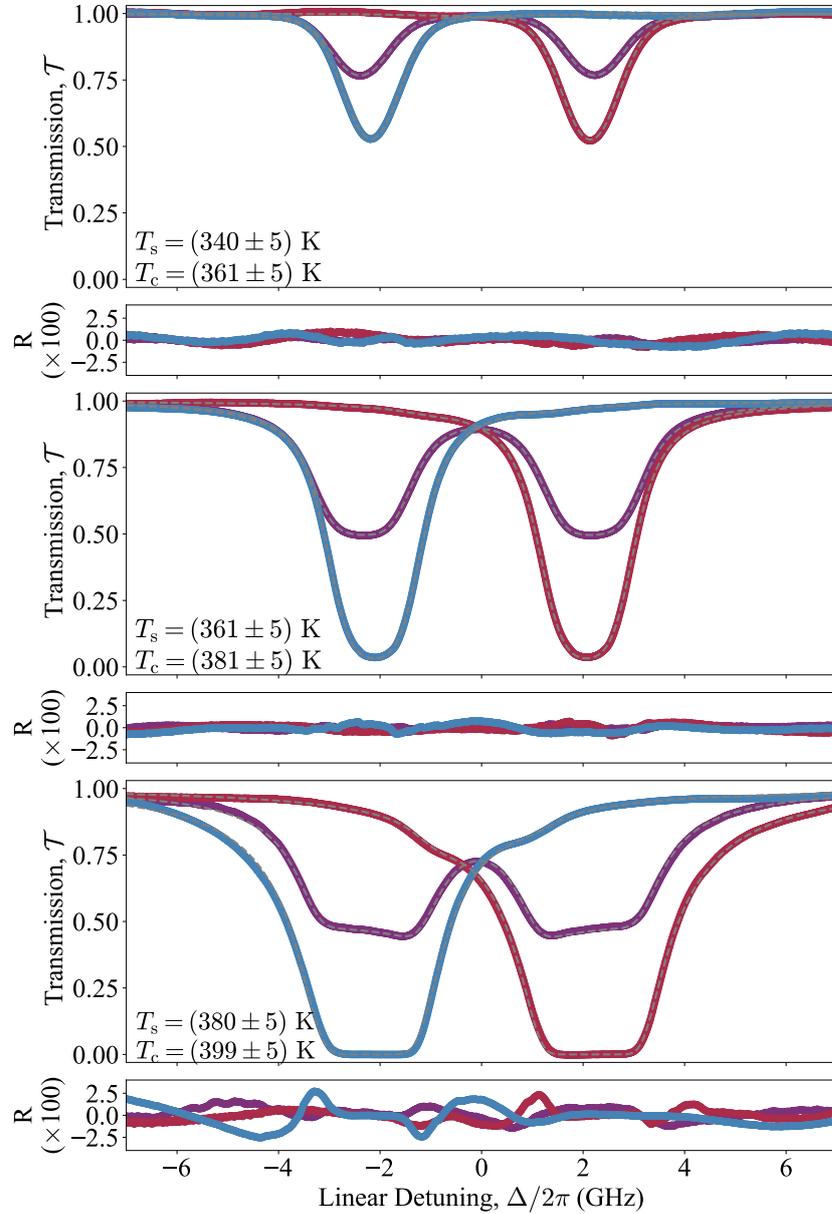
Figure 5.8: Transmission spectra for the potassium D1 line were recorded at a magnetic field strength of (1200 ± 5) G using a 25 mm vapour cell with 60 Torr of neon. The measurements were performed for three different sets of cell and stem temperatures, as indicated in the legend. Residuals show excellent agreement between the experimental data and the theoretical fits.

small absorption dip around ± 1 GHz is observable, which is due to the ^{41}K isotope.
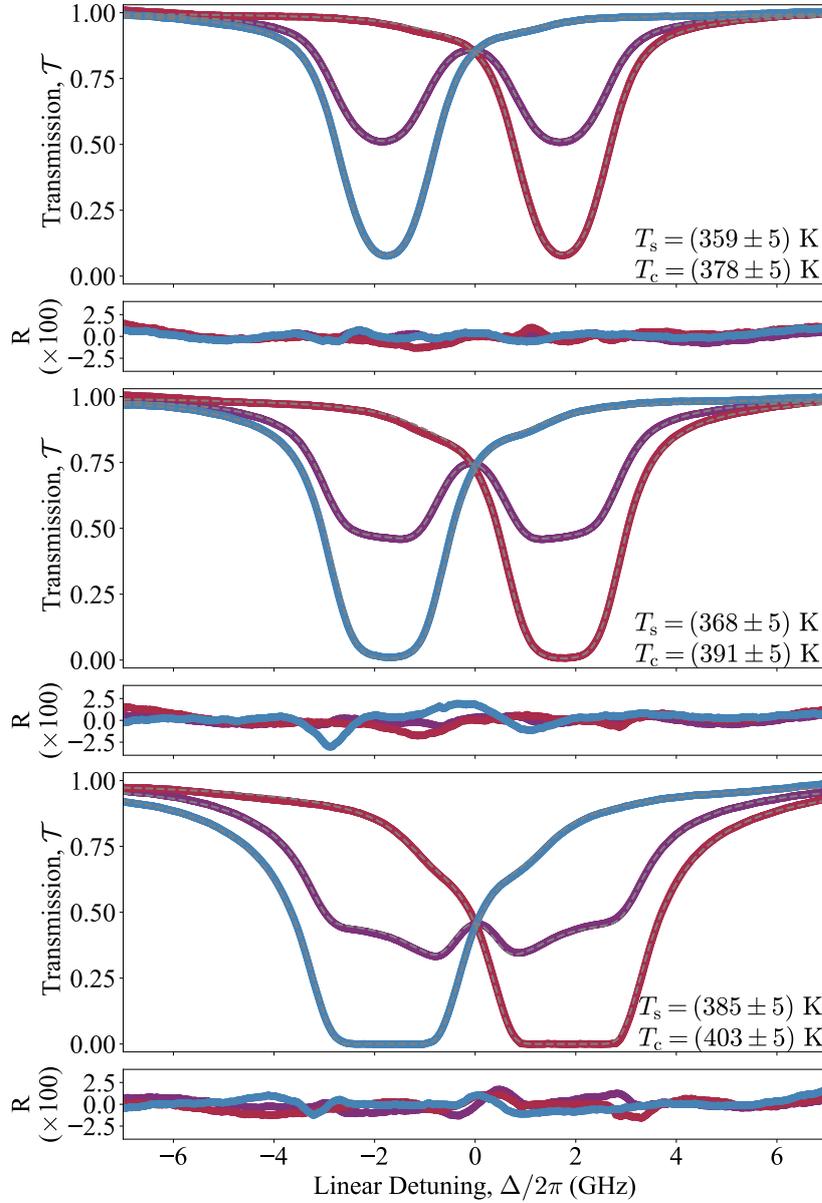
Figure 5.9: Transmission spectra of the potassium D1 line at a magnetic field of $B = (970 \pm 4)$ G, measured with linearly polarised light (purple), left-circularly polarised light (σ^+, red), and right-circularly polarised light (σ^-, blue). The data were obtained using a 25 mm vapour cell with 60 Torr of neon at three different sets of cell and stem temperatures, as indicated in the legend. Residuals show an excellent agreement between experimental data and theoretical fits.

Figure 5.9 present similar spectrum measurements taken at 900 G at three different sets of cell and stem temperatures: $T_c = (378 \pm 5)$ K, $T_s = (359 \pm 5)$ K;

$T_c = (391 \pm 5)$ K, $T_s = (368 \pm 5)$ K; and $T_c = (403 \pm 5)$ K, $T_s = (385 \pm 5)$ K. Compared to the 1200 G case, the Zeeman splitting is, in fact, a bit less pronounced, with σ^+ and σ^- features getting closer to each other. Still, they are relatively distinct from the central features in the linearly polarised spectra. Consistent with the 1200 G data, higher temperatures lead to greater absorption from the vapour which in turn increases vapour opacity. The characteristic dips from the ^{41}K isotope are still observable around ± 1 GHz.

Figure 5.10 shows the spectra at 700 G, acquired at three different sets of temperatures. The weaker magnetic field has a proportionately weaker Zeeman splitting. The σ^+ and σ^- features are now considerably closer together, and the linearly polarised spectrum becomes more smeared because of this overlap. As with the other datasets, raising the temperature enhances both the absorption strength and the broadening of spectral features. The small ^{41}K isotope dips are still observable, but at lower magnetic field values, they become more difficult to resolve. This is mainly due to the decreased Zeeman splitting causing greater spectral overlap between the ^{41}K and ^{39}K features, which reduces their visibility. Furthermore, the more blended and compact spectrum makes the signal of the less abundant ^{41}K even more indistinguishable.

The incident circularly-polarised light; be it left or right, can be extinguished completely due to the distinct interactions with the medium. However, linearly polarised light can be represented as an equal combination – or superposition – of the two circular components. With the application of the Zeeman effect, one of these components may couple strongly to the medium while the other does not, creating a minimum of around 50% transmission. This demonstrates the effect of polarisation state on the transmission of light near the potassium D1 transitions in the heated vapour cell subject to a magnetic field. To fully account for the transmission profile, especially in the spectral wings, one needs to consider the buffer
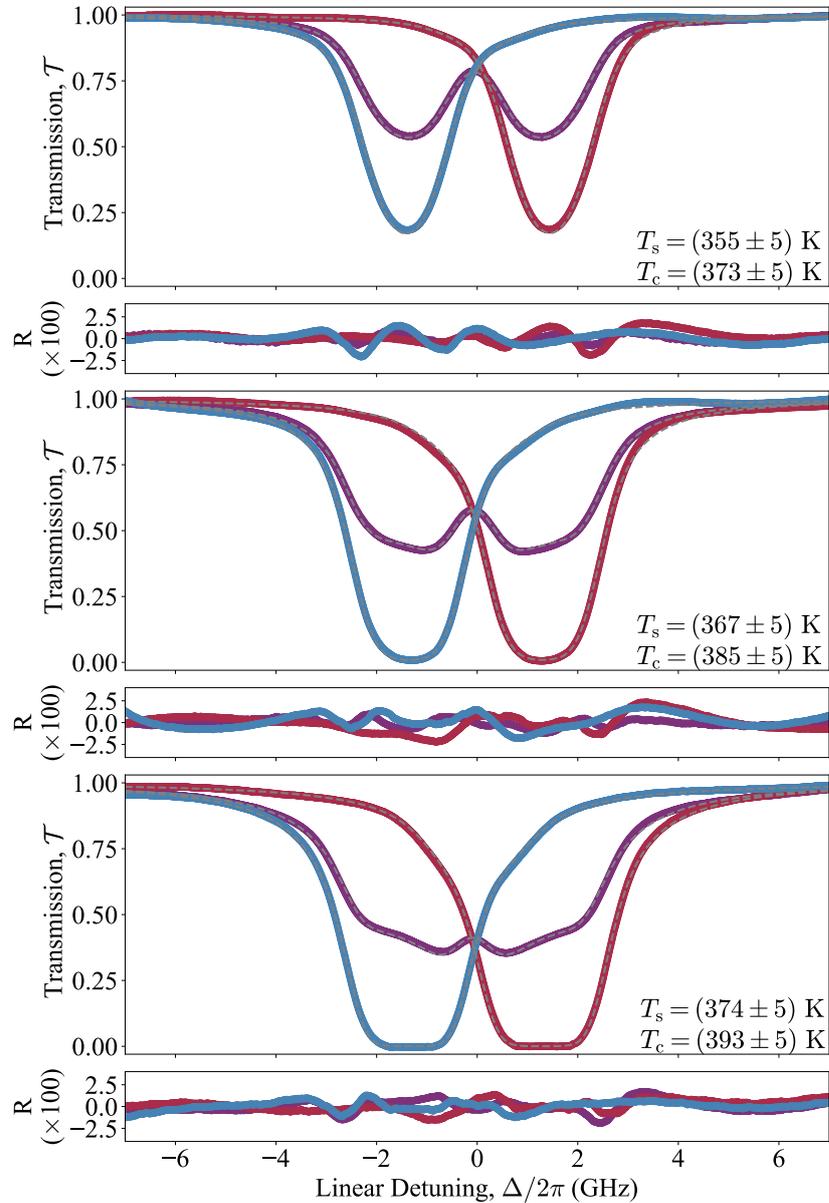
Figure 5.10: Transmission spectra of the potassium D1 line at a magnetic field of $B = (750 \pm 4)$ G, measured with linearly polarised light (purple), left-circularly polarised light (σ^+, red), and right-circularly polarised light (σ^-, blue). The data were obtained using a 25 mm vapour cell with 60 Torr of neon at three different sets of cell and stem temperatures, as indicated in the legend. Residuals show an excellent agreement between experimental data and theoretical fits.

gas broadening effects.

5.5 Conclusion and Outlook

This study provides an analysis of the potassium D1 transition with neon buffer gas regarding pressure-induced broadening and shift, as well as Zeeman splitting in an external magnetic field. Employing a dual-temperature control system, we were able to measure the absorption spectra at different temperatures and pressures of the buffer gas which allowed us to extract the broadening and shift values (Γ) and (S) respectively. Our data indicate that increasing buffer gas content results in significant line broadening and a shift to lower frequencies. Forthermore, measurements of the filling pressures resulted in values (57.4 ± 0.6) Torr and (96 ± 1) Torr, thus validating the bespoke request of 60 Torr and 100 Torr imposed on the vapour cell manufacturer. Additionally, our measurements agree well with the potassium-neon collisional values from Pitz *et al.* [80]. More importantly, this is the first time that buffer-gas effects have been integrated successfully into a modified Voigt profile on the *ElecSus* code, proving excellent agreement between the theoretical and experimental line profiles. Significant changes are seen for cells containing higher buffer gas at higher temperatures. The theoretical model of the evolution of the Voigt profile from Gaussian- to Lorentzian- dominated was successfully reproduced in the experiment.

Moreover, we focused on how an external magnetic field affects the pressure-broadened potassium D1 spectrum using a 25 mm vapour cell. We obtained the magnetic field strength and studied the Zeeman splitting of the hyperfine Paschen–Back regime by fitting the transmission spectra of the (σ^+) and (σ^-) circular components to *ElecSus*. The measured shifts of these components were observed to scale linearly with the magnetic field, which is in agreement with the expected Zeeman effect for this regime. The excellent agreement between the theoretical predictions and experimental data strongly confirms the implemented

Zeeman and collisional effects into our model for the alkali-metal vapour transmission.

Although the primary motivation of this study is the design of magneto-optical filters for applications in solar physics, this study contributes to the understanding of potassium spectroscopy, in addition to the interaction between alkali-metal atoms and buffer gases. The findings regarding line shape evolution under buffer gas effect will be extremely useful in developing other sensor technologies that utilise potassium vapour [107, 135, 136, 137, 138].

Choosing the right buffer gas and its partial pressure is always critically application-specific, requiring a careful balance of trade-off. For instance, argon broadens spectral lines (∼19 MHz/Torr) and shifts them more negatively by (∼6.5 MHz/Torr) than neon [80]. This property may allow the use of lower partial pressures to obtain a desired Voigt lineshape, potentially reducing unwanted fine-structure-changing collisions [87] and thus improving contrast in solar magnetograms. However, it is important to note that heavier gases such as argon cause larger shifts that vary with temperature, requiring tighter temperature control for stable operation.

On the other hand, helium broadens spectral lines about twice as much as neon but shifts them in the positive direction by similar amount (∼ +1.6 MHz/Torr). Beyond the use of single buffer gases, carefully designed buffer gas mixtures could reduce or even negate temperature-dependent shifts which is critical for stable atomic clocks [139]. As a result, modeling the influences of these gas mixtures, along with addressing practical concerns such as cell temperature control and buffer gas permeation (especially with lighter gases), is essential for ensuring reliable long-term operation.

This study provides a reliable computational tool for modeling potassium spectroscopy in the presence of neon buffer gas. Although this work provides a base understanding of the impact of buffer gases on absorption, it has also been important to investigate their effects on the real part of the susceptibility which influences optical rotation and dispersion. This provides a clear motivation for us

to use Stokes polarimetry to probe these effects. The next chapter discusses the Stokes polarimetry approach which allows polarisation-dependent investigation of the behaviour of light interacting with potassium vapour under the influence of a magnetic field and in the presence of buffer gas.

CHAPTER 6

Stokes Polarimetry of Potassium D1 Line with Neon Buffer Gas

This chapter is based on the following paper that is under peer review:

Sharaa A. Alqarni, Danielle Pizzey, Steven A. Wrathmall, and Ifan G. Hughes. "Experimental and theoretical characterisation of Stokes polarimetry of the potassium D1 line with neon buffer gas broadening". *arXiv Preprint*, 2507.18353, (2025). https://doi.org/10.48550/arXiv.2507.18353 [3]

6.1   Introduction

Stokes polarimetry is a technique which provides the complete characterisation of the polarisation state of electromagnetic waves with four parameters known as Stokes parameters (S_0, S_1, S_2, S_3). Using this technique on light that has interacted with an atomic vapour provides us with a very important diagnostic tool [140]. This technique can be applied to determine very small changes in the atomic medium induced by factors such as magnetic fields (i.e. Zeeman and Hanle effects, where

Hanle effect describes the modification of atomic polarisation in the presence of a magnetic field [141]), electric fields, or collision processes [142]. These polarisation properties exhibit dramatic sensitivity to the changes in the atomic medium, all of which make polarimetry a great tool to perform fundamental studies in atomic physics [44].

Alkali metal atoms provide a particularly interesting platform within both theoretical predictions and experimental investigations of atom-light interaction. For example, Stokes polarimetry has been successfully used to examine atom-light interactions in Rb vapour, even in extreme conditions with high density atomic vapour and strong external magnetic fields [96, 143]. However, the presence of buffer gases on the measured Stokes parameters have not been studied, in particular with regards to spectral broadening and line shifts, as discussed in Chapter 5 and in reference [2].

This chapter presents an experimental investigation of Stokes polarimetry with potassium atomic vapour in the presence of neon buffer gas. We measure the complete polarisation state of resonant D1 laser light after it has passed through the atomic medium. We compare these experimental results with theoretical predictions calculated using *ElecSus*. Potassium vapour cells filled with a buffer gas are used in solar observations to observe the Sun through the atomic medium from which the four Stokes parameters can be measured, enabling the extraction of solar magnetograms [19].

In this study, we apply magnetic fields between 750 G and 1200 G, which are generally well into the Hyperfine Paschen Back (HPB) regime as discussed in Chapter 2. This means the spectroscopy is carried out well within the HPB regime, where the results are easier to interpret. Similar fields, or stronger, have been used in magneto-optical filters and wing selectors for solar filter experiments [51, 52, 53, 54, 19].

In chapter 5 [2], we studied the effect of varying the amount of neon buffer gas, and

the magnetic field on potassium D1 transition. Our focus was on how Doppler and collisional contributions influence the spectrum. As mentioned in Chapter 2, the fraction of light absorbed as it passes through the atomic medium depends on the imaginary part of electric susceptibility, while how the light's speed is affected as it moves through is described by the real part. In the presence of an axial magnetic field (known as Faraday geometry), the two polarisation modes are left and right circular polarisation [78]. It is noted that the magnetic field renders the medium both birefringent and dichroic in that the polarisation state of the light will evolve as it propagates through the medium. Stokes polarimetry is an effective method to identify the polarisation state of the transmitted light after emerging from the cell. In order to get a complete description of the evolution in polarisation, both the real and imaginary part of susceptibility need to be considered. This is especially important when designing devices like magneto-optical filters. The purpose of this study is to expand on the earlier analysis of the imaginary part from Chapter 5 and experimentally determine both components as a function of the magnetic field and the temperature in areas where collisional broadening can not be ignored.

In the following sections we illustrate the experimental set-up and procedure used to perform potassium Stokes polarimetry as a function of temperature and magnetic field strength. After that, we present and discuss the experimental results obtained for the potassium D1 line and compare them with our theoretical predictions.

6.2 Theoretical Predictions for Potassium D1 Stokes Parameters

This section presents theoretical predictions for the potassium D1 Stokes parameters, calculated using the theoretical model outlined in Section 2.7. The computed spectra demonstrate the expected temperature and magnetic field dependencies that guide our experimental analysis and provide expected results to compare with our measurements.
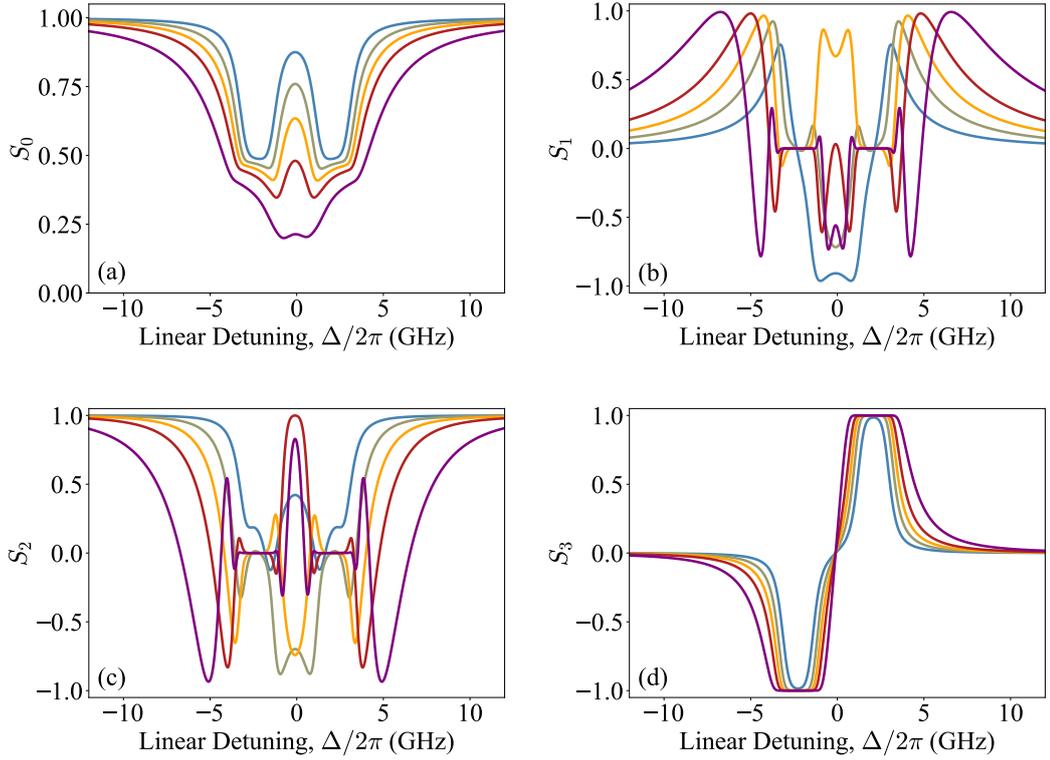
Figure 6.1: Theoretical normalised Stokes parameters (a) S_0, (b) S_1, (c) S_2, and (d) S_3 for a 25 mm potassium vapour cell filled with 60 Torr of neon buffer gas. The input light is diagonally linearly polarised before entering the cell. The applied magnetic field is 1160 G, with T_s increasing from 75°C (blue) to 135°C (purple), in 15°C increments. Zero of the detuning axis is the weighted line-centre of the respective D1 line.

6.2.1 Temperature-Dependent Behavior

Figure 6.1 shows the theoretical Stokes parameters (S_0, S_1, S_2, S_3) as a function of linear detuning. The vapour cell is 25 mm long, contains potassium vapour with 60 Torr of neon buffer gas subjected to a magnetic field of 1200 G in a Faraday configuration; the highest magnetic field allowed in our research [2]. The calculations were completed using *ElecSus* in the weak-probe regime and the temperature is increased from 75–135 °C, in 15 °C increments. The incident light is linearly polarised at an angle of 45° to the polarisation axis, meaning the wavelengths interacting with the atomic medium are composed of equal parts left- and right-circularly polarised light.

Figure 6.1 (a) shows S_0 which represents the total intensity of the light transmitted.
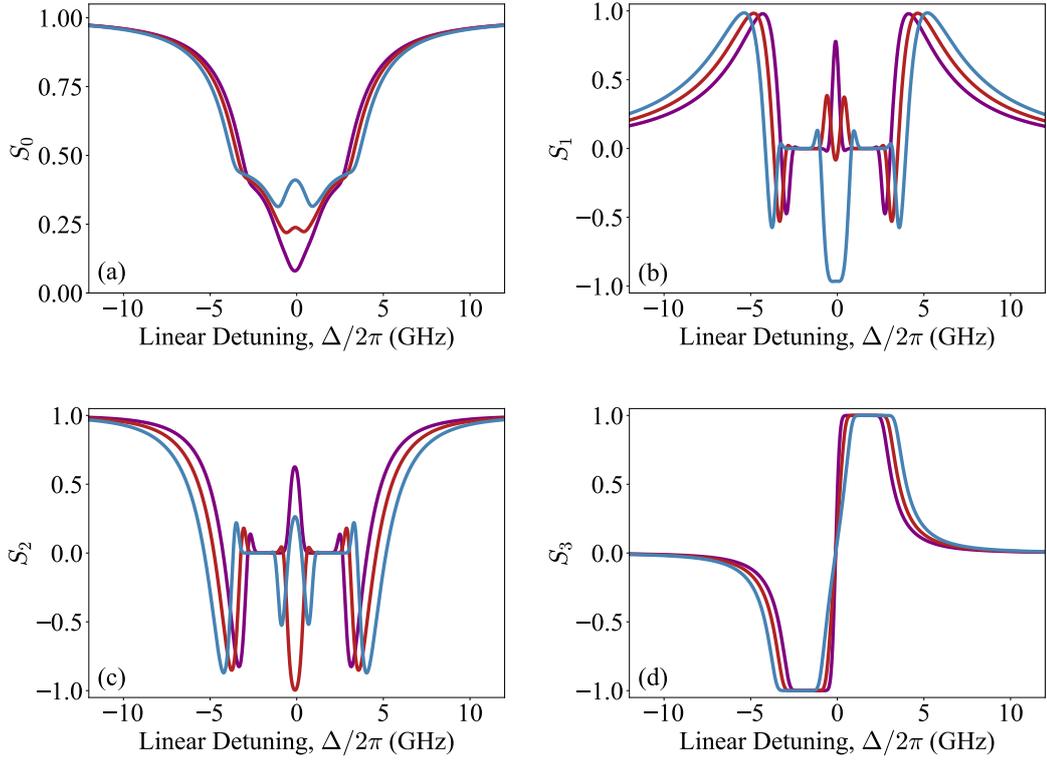
Figure 6.2: Theoretical normalised Stokes parameters (a) S_0, (b) S_1, (c) S_2, and (d) S_3 for a 25 mm potassium vapour cell filled with 60 Torr of neon buffer gas. The input light is diagonally linearly polarised before entering the cell. The applied magnetic field is 750 G (purple), 1000 G (red) and 1200 G (blue) with T_s sets to 120°C. Zero of the detuning axis is the weighted line-centre of the respective D1 line.

Since it is normalised to the intensity of the output light, its value never exceeds 1. As the temperature increases, the S_0 absorption profile has significant increases in terms of depth and width because of the increased atomic density, larger amounts of Doppler broadening and larger collisional broadening rate. As a result, $\sigma^\pm$ Zeeman absorption dips, occurring at detunings of around ± 2 GHz, are less resolved and merged into a broader feature centred at 0 GHz because of this increased spectral broadening; this is consistent with our finding in Chapter 5.

S_1 and S_2 in Figures 6.1 (b) and (c), respectively, quantify the linear polarisation state of the transmitted light. These parameters describe the rotation of the polarisation plane of the light as it propagates through the atomic medium. Their complex, often oscillatory, shapes around resonance (i.e. $\Delta/2\pi = 0$ GHz) comes

from the birefringence (and less so dichroism) in the vapour due to the external magnetic field. The Faraday angle of rotation is proportional to the difference in the refractive index (i.e. real component of χ) of the right- and left-handed polarisations [144]; as the number density of the vapour grows almost exponentially as a function of temperature [4], as we saw in Figure 2.6 of Chapter 2, there is a rapid evolution in the optical rotation with modest changes in temperature. In particular, at 0 GHz linear detuning (on resonance) S_1 and S_2 display distinct values which oscillate between +1 and -1 as a function of vapour cell temperature. Optical rotation changes rapidly with frequency, whereas the absorption spectrum changes much more slowly, and is well known for alkali-metal vapours [48, 72, 145]. In fact, the zero-crossings in the S_1 and S_2 spectra can be used for laser frequency stabilisation [146, 147].

The Stokes parameter S_3 shown in Figure 6.1 (d) describes the circular dichroism of the medium (the distinct absorption of the circular polarisation states) which is induced by the magnetic field. The extinction for each of the $\sigma^\pm$ transitions is described by the appropriate imaginary component of the susceptibility, χ. The real components of the susceptibility do not affect S_0 or S_3, so we notice that these two Stokes parameters do not have the same rapid temperature dependence as for S_1 and S_2.

When the Zeeman shift is similar or greater than the linewidth of the transition, S_3 has a characteristic dispersive shape with sharp transition through zero about 0 GHz linear detuning. The steepness of the slope provides a measure of the medium's sensitivity to the magnetic field; the slope steepens with increasing vapour density (i.e. at hotter temperatures). We also note that S_3 reaches a value of ± 1 at detunings centred about ± 2 GHz. This occurs because at a detunings of $+(-)2$ GHz, the light becomes resonant with the σ^+ (σ^-) transition due to the optically thick medium, the left-(right-) circular polarisation component is completely absorbed, leaving only the right-(left-) circular light component of the incident polarisation state. As a result, S_3 reaches a value of $+1(-1)$. The frequency-dependent char-

acteristics of this S_3 response provide the discriminating signal required for laser frequency locking using the DAVLL approach [46, 148].

Figure 6.2 shows the theoretical predictions for Stokes parameters as a function of linear detuning using a 25 mm potassium vapour cell filled with 60 Torr of neon buffer gas at a constant temperature of 120°C. The simulations were conducted at three different magnetic field strengths and in the Faraday configuration. The data shows trends that are similar to the data above in Figure 6.1: both S_0 and S_3 exhibited gradual, smooth spectral changes, in contrast to S_1 and S_2 which exhibited more complicated spectral behavior attributed to the dependence on the real part of susceptibility which causes optical rotation effect.

Figures 6.1 and 6.2 show how Stokes parameters vary with temperature and magnetic field strength in the presence of a known buffer gas filling pressure, allowing for profile characterisation. The figures did not clearly reflect the shift and broadening effects which present from the buffer gas. We provided this information in Figure 6.3, comparing all four Stokes parameters between three cases; vapour cells at 0 Torr, 60 Torr, and 100 Torr of neon buffer gas, examining their behaviour across varied vapour cell stem temperatures and magnetic field strengths.

Figure 6.3 presents the normalised Stokes parameter at resonant conditions (zero linear detuning) as a function of vapour cell stem temperatures at three magnetic field strengths (B = 700 G, 1000 G, and 1200 G). As one would expect, the results for both S_0 and S_3 values provide gradual continuous change with respect to both temperature and magnetic field strength, with opposite trends (i.e. as the temperature rises $S_0 \rightarrow 0$, and $S_3 \rightarrow 1$). Furthermore, the vapour cell with most buffer gas approaches 0 and 1 for S_0 and S_3, respectively, at lower temperatures than a vapour cell with no buffer gas. The buffer gas causes a line shift, and since the S_3 value is measured at $\Delta/2\pi = 0$ GHz, the diagram in Figure 6.3 (d) shows that it has a greater accuracy in measuring this than the other Stokes parameter measurements.
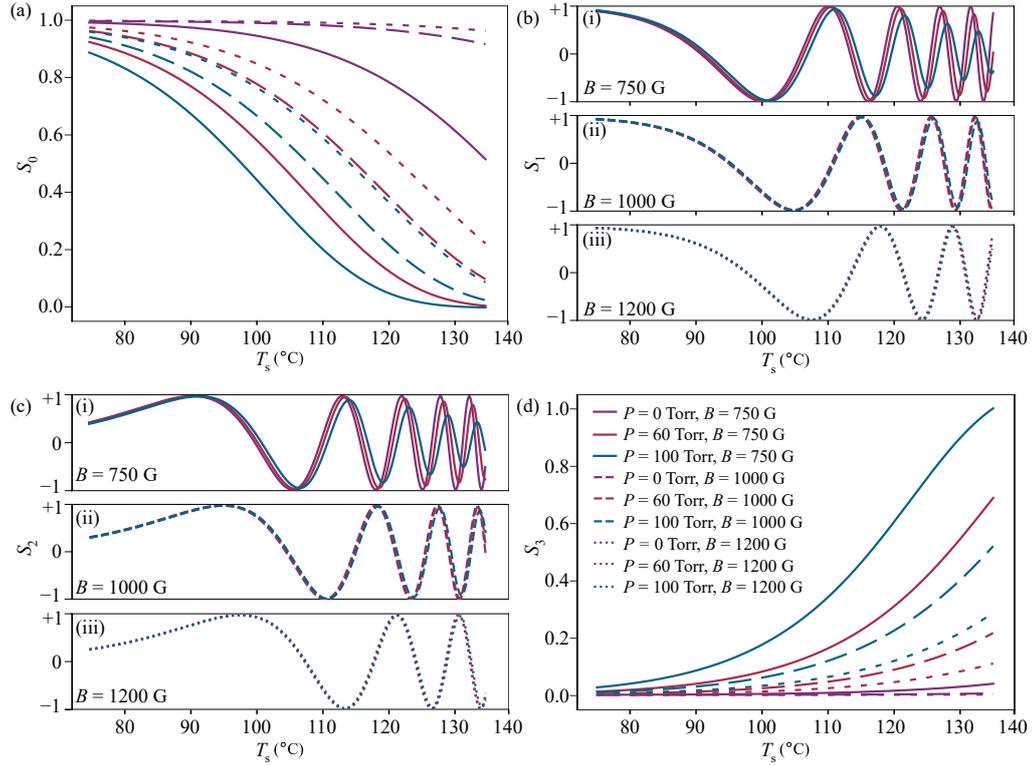
Figure 6.3: Theoretical *ElecSus* simulations showing the magnitude of the normalised Stokes parameter at resonance (i.e. $\Delta/2\pi = 0$ GHz) for (a) S_0, (b) S_1, (c) S_2 and (d) S_3. The calculations cover a stem temperature range between 75–135°C in a vapour cell, with magnetic fields in Faraday geometry set at 750 G (solid lines), 1000 G (dashed lines), and 1200 G (dotted lines), for three neon buffer gas filling pressures of 0 Torr (purple), 60 Torr (red), and 100 Torr (blue).

In contrast, there is oscillatory behaviour in both S_1 and S_2, with fewer oscillations in the given temperature range, as the strength of the magnetic field increases. When looking at vapour cells filled with buffer gas, both S_1 and S_2 values decay to zero, with higher-pressure buffer gas cells showing much more rapid decay for moderate magnetic field strengths (this can be seen in Figure 6.3 (b)(i) and (c)(i)). There also appears to be a temperature difference from when the medium decays to zero. One might be inclined to think that there is no optical rotation occur when the values of S_1 and S_2 are zero. However, it is evident from S_0 - Figure 6.3 (a) - that there is an optically thick medium, there is no transmission and this occurs at a lower temperature when there is more buffer gas due to pressure broadening. By increasing magnetic field, we can decrease ($B = 1000$ G) or eliminate ($B =$

1200 G) these decays at the temperature range considered. As the magnetic field is increased, the atomic $\sigma^{\pm}$ transitions drift apart, leading to a small difference in refraction index (the medium's birefringence) at resonance. Once Zeeman splitting exceeds pressure broadening, we can recover optical transmission and rotation, as seen in Figure 6.3 (b)(iii) and (c)(iii), where the three traces are in phase. The results in Figure 6.3 (b) and (c) support that off-resonance laser stabilisation systems must have a stable temperature, otherwise even small temperature changes, or temperature drift, lead to large shifts of the zero-crossing points [149, 150].

Overall, these plots show the detailed and complex ways that light polarisation changes when it passes through potassium vapour in the presence of magnetic fields and buffer gas. This theoretical understanding provides the essential foundation scientists need to properly interpret their experimental results.

6.3 Experimental Results

Herein we present the experimental results from potassium D1 line spectroscopy. This section examines two of our main results: how the Stokes parameters vary with temperature in the presence of a buffer gas; and how the Stokes parameters vary with the magnetic field. The experimental spectra were fitted using the *ElecSus* model, with a differential evolution algorithm. The fitting used the stem temperature (T_s), cell temperature (T_c), spectral shift (S), and broadening (Γ) as free parameters. We constrained T_c and T_s to $\pm 5°$C.

6.3.1 Temperature dependence of Stokes parameters

Figure 6.4 shows the measured Stokes parameters as a function of linear detuning for a 25 mm potassium vapour cell containing 60 Torr of neon buffer gas, with the magnetic field held constant at 1160 G. Measurements were taken at five different temperatures. The figure also includes theoretical fits generated using *ElecSus*, and for one dataset, the residuals defined as the difference between experimental and theoretical transmission are shown below, scaled by a factor of 100 to enhance
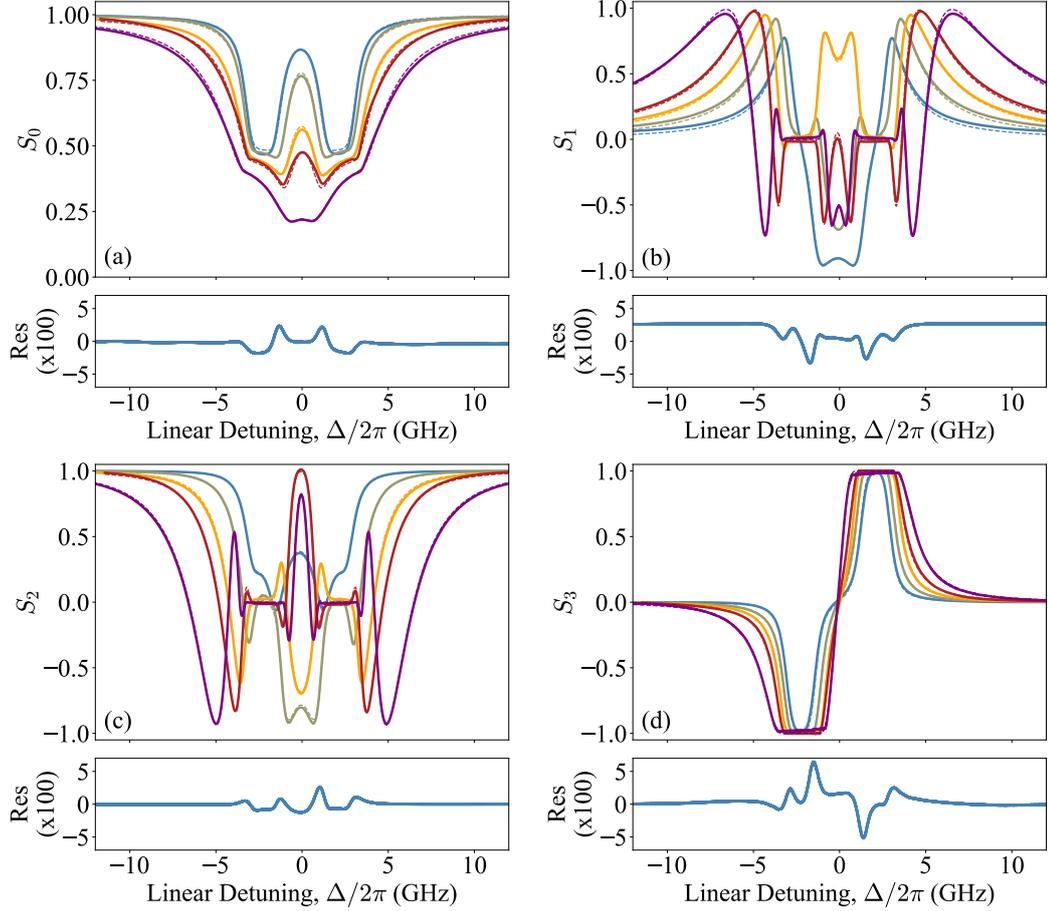
Figure 6.4: The experimental and theoretical Stokes parameters for the potassium D1 line plotted as a function of linear detuning $\Delta/2\pi$, measured in a 25 mm potassium vapour cell (natural abundance, 60 Torr neon buffer gas). The solid lines correspond to the experimental data and the dotted lines correspond to the fits from the *ElecSus* model. The four Stokes parameters S_0, S_1, S_2, and S_3 (from panels (a)–(d)), are shown for the five vapour cell temperatures of 93°C (blue), 103°C (green), 110°C (yellow), 118°C (red), and 129°C (purple). The residuals shown at the bottom of each subplot, corresponding to the 93°C dataset, clearly indicate the excellent agreement between the experiment and theory.
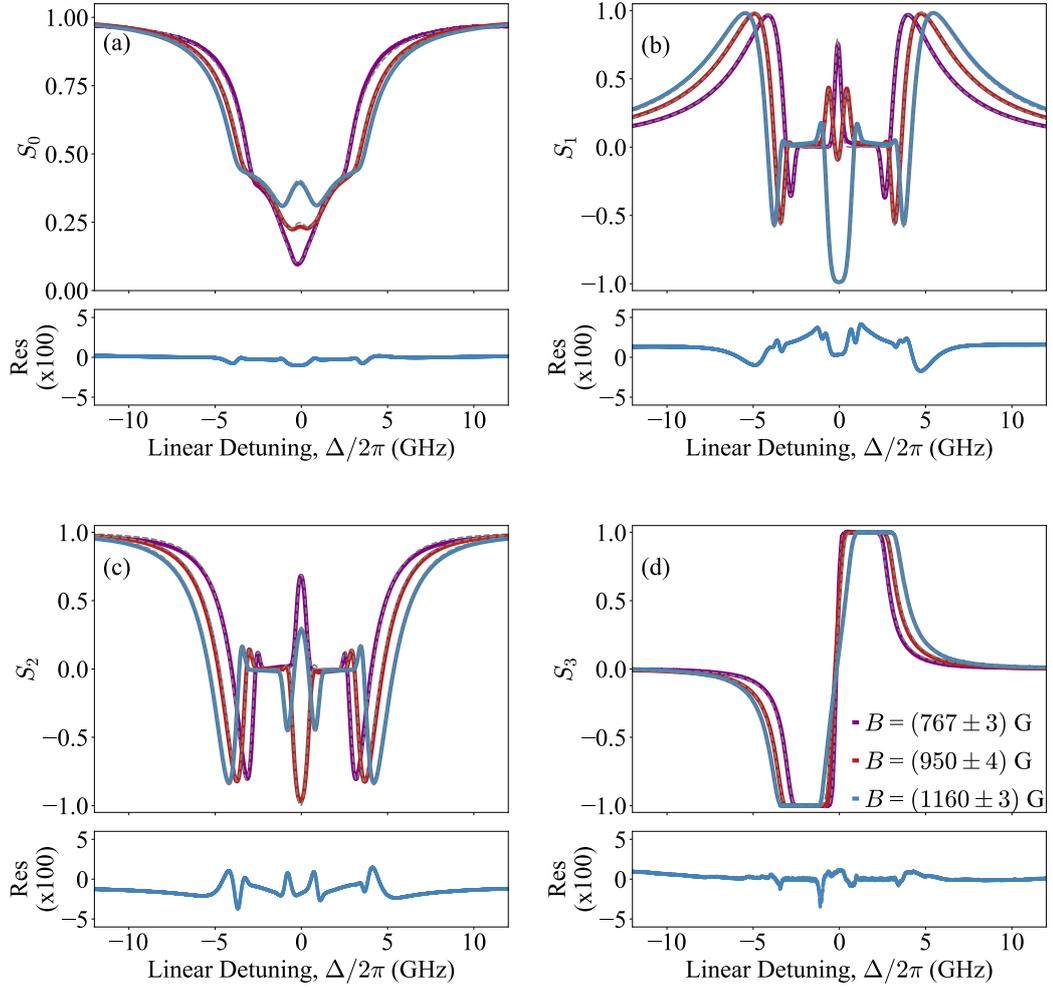
Figure 6.5: Magnetic field dependence of the four Stokes parameters (a) S_0, (b) S_1, (c) S_2, and (d) S_3 measured at a fixed (T_s) of 120 °C. The plots show the experimental data and theoretical fits from *ElecSus* at three different magnetic field strengths: 767 G, 950 G, and 1160 G.

visibility. The size and pattern of these residuals help assess how well the model fits the data [127].

The theoretical model successfully reproduces all major features of the measured Stokes parameters, including the effects of the buffer gas. Both the absorption features seen in S_0 and S_3 and the sharp dispersive features in S_1 and S_2 are well captured by the model.

6.3.2 Magnetic field dependence of Stokes parameters

Figure 6.5 shows the measured Stokes parameters of the potassium D1 line at a stem temperature of $(120 \pm 5)°$C for a 25 mm vapour cell filled with 60 Torr of neon buffer gas. Spectra for each experimental measurement were measured at three magnetic field strengths, determined by fitting the data with *ElecSus*, yielding values of (767 $\pm$3) G, (950 $\pm$3) G, and (1160 $\pm$4) G. The uncertainty in the magnetic fields were calculated using the method described in [31], which involve varying the input polarisation at a fixed magnetic field and fitting each spectrum with *ElecSus* to estimate the field strength.

Theoretical simulation of the magnetic field distributions for these three permanent magnets separations yields average field strengths in agreement with the measurement, and predicts axial root-mean-square field variations of 23%, 13%, and 3% along the length of the vapour cell, respectively. In general, the experimental spectra demonstrates good agreement with the *ElecSus* fits, evident from the residuals.

As in temperature-dependent measurements, all the significant spectral features of the Stokes parameters are accurately replicated in the theoretical model including both absorptive components and the rapidly varying dispersive features observed in S_1 and S_2.

6.4 Conclusion and Outlook

This chapter represented an extensive experimental and theoretical investigation of Stokes polarimetry of potassium (K) atomic vapour in the presence of a neon buffer gas on the D1 transition with a particular emphasis on temperature and magnetic fields related effects. Our aim was to understand how these parameters affected the absorption and polarisation behavior of the atomic medium, while simultaneously testing theoretical predictions against measured data. Using weak-probe measurement system we systematically tracked changes in all four Stokes parameters (S_0, S_1, S_2 and S_3) as a function of the temperature and magnetic field strengths. We

noticed that increasing temperatures yield deeper absorption features and broadened spectral line widths in S_0, causing Zeeman splitting components to be less observed. Consequently, at elevated temperatures, the linear polarisation signals (S_1 and S_2) displayed enhanced complexity, amplitude, and spectral widths. The unique dispersive shape of S_3 (which corresponds to circular polarisation), which reflects Faraday rotation effects, had expected dependencies on temperature and strength of an applied magnetic field.

A significant achievement of this study is that we were able to validate and implement the established *ElecSus* software package as an approach to represent these complex phenomena. By modeling the temperature dependent atomic concentrations, Doppler line broadening, integrated with observable buffer gas effects including pressure broadening, and shifts, the theoretical spectra generated by *ElecSus* demonstrated remarkable agreements with the experimental measurements over a range of conditions. This marks the first application of *ElecSus* to buffer gas polarimetry investigations of the potassium D1 transition, representing significant reference calculations for future theoretical work, and exhibiting a thorough treatment of both real and imaginary electric susceptibility components in the model.

The data provided in this work represent a considerable advance to our comprehension of light-atom interactions in the buffer gas configuration. This enhanced understanding not only develops the accuracy of a theoretical model like *ElecSus* with other complex alkali vapour systems, but it will also support other practical applications utilising these vapours such as precision magnetometry and advanced optical filters.

Future work could comprise extending the ranges of neon pressure and temperature, examining the effects on the potassium D2 transition, or investigating the effects of other noble buffer gases to build the understanding of collisional interactions. Further improvements to the theoretical models to account for more detailed collisional dynamics, such as velocity-changing [151] and spin-exchange collisions [152], may also be feasible. Incorporating these effects would allow the models to make more

accurate predictions of line shapes and frequency shifts, which are very beneficial in developing and optimising quantum technologies such as atomic clocks [139], magnetometers [74, 75], and narrow-band atomic filters [40].

CHAPTER 7

Conclusions and Outlook

Here we provide a brief summary of the work investigated in this thesis. We will also comment on possible future investigations that could follow on from the work presented here.

Chapter 4: Magnetic-Field Angle Control in Rubidium Magneto-Optical Filters. [1] This chapter presented a novel method for creating arbitrary magnetic field angles based on the configuration formed by combination of a pair of permanent magnets in a Voigt geometry with a soleniod. This new method had the potential to control the magnetic field angle accurately and flexibly more than the traditional method, which relied on physically rotating the permanent magnets. To replicate the field produced by a rotated permanent magnet pair with our new method, we utilised *Magpylib* to simulate the magnetic fields for the two configurations and then selected solenoid-plus-permanent magnet parameters accordingly, such that the old and new methods could be directly compared. Experimental results confirmed excellent agreement with comparable strength and orientation of the magnetic field and performance of the magneto-optical filter between the two methods. A key limitation of the previous method was the difficulty in quickly and accurately determining the rotation angle. In addition, using longer vapour cells (which improve filter performance) limited the achievable range of angles when the

magnets are rotated.

These challenges were overcome with the solenoid-plus-permanent configuration as the permanent magnets did not rotate with the cell. This allowed for creating large angles and using longer vapour cells which will allow for better magneto-optical filters to be realised [56]. Another benefit to the new configuration is that we can easily and quickly tune the magnetic field angle by adjusting the current through the solenoid. Furthermore, we demonstrated how small changes in angle can produce relatively large discrepancies to shape of the filter profile which is an effect that is much easier to explore using our more controllable and adaptable design.

One of the most effective extensions would be to develop a miniaturised arbitrary-angle magnetic field generator for high-speed optical switching. The switch speed in the current system is limited by large solenoid inductance, but miniaturisation to micro-solenoids with small permanent magnets would decrease inductance considerably and enable microsecond switch times. This miniaturised structure would find ideal application for chip-scale integration in telecommunication and photonics circuits.

Chapter 5: Influence of Buffer Gas on the Potassium D1 Line Profile. [2] This study investigated the potassium D1 transition in the presence of neon buffer gas, in particular the pressure induced broadening and frequency shift, and the Zeeman splitting under an external magnetic field. By employing a dual temperature control, we measured the absorption spectra at several temperatures and pressures which allowed us to extract broadening (Γ) and shift (S) values. We found that increasing the concentration of buffer gas induced a large amount of broadening and observed red-shift for the resonance lines. The measured filling pressures of (57.4 ± 0.6) Torr and (96 ± 1) Torr were very close to the manufacturer's pressures of 60 Torr and 100 Torr respectively. Also, our results showed good comparison with potassium-neon collisional parameters reported by Pitz et al. [80]. Most importantly, it is the first time effects of buffer gas conditions have been successfully

incorporated into a modified Voigt profile within the *ElecSus* code. We found excellent agreement between the predicted and measured line profiles, in particular for cell with high buffer gas at high-temperature cells, especially in the wings of the profile. The theoretical prediction of the evolution of the Voigt profile from Gaussian- to Lorentzian- dominated was successfully reproduced in the experiment.

We also explored the effects of magnetic fields on the broadened spectra, used a 25 mm cell for this study. By fitting the two circularly polarised components σ^+ and σ^- to the *ElecSus*, we were able to extract magnetic field strengths, and showed that the Zeeman shifts scaled linearly with magnetic field strength, confirming we were in the hyperfine Paschen–Back regime. The good agreement between the theory and the experiments confirmed a properly implemented consideration of Zeeman and collisional effects in the model. Although the primary motivation of this study was the design of magneto-optical filters for applications in solar physics, it also enhanced our understanding of potassium spectroscopy and interaction between alkali-metal atoms and buffer gases. The findings will be useful in developing other sensor technologies that utilise potassium vapour [107, 135, 136, 137, 138]. Choosing the right buffer gas and its partial pressure is always critically application-specific, requiring a careful balance of trade-off. This study provided a reliable computational tool for modeling potassium spectroscopy in the present of neon buffer gas. Future work will extend this framework to include other buffer gases with potassium and to heavier alkali-metals like rubidium and caesium to thoroughly test and refine the *ElecSus* model for alkali-metal vapour transmission.

Chapter 6: Stokes Polarimetry of Potassium D1 Line with Neon Buffer Gas. [3] This chapter conducted a comprehensive experimental and theoretical study of the Stokes polarimetry on the D1 line of potassium (K) atomic vapour with neon buffer gas. The primary focus of this study was characterising how temperature and magnetic field affect the absorption and polarisation properties of the atomic medium, and validating a theoretical model against experimental measure-

ments. The evolution of the Stokes parameters (S_0, S_1, S_2, S_3) in the weak-probe regime was systematically mapped against vapour temperature and magnetic field strength. We observed that increasing temperature led to an increase in absorption depth and spectral broadening in S_0, with the Zeeman-split components becoming less resolved. The linear polarisation signals (S_1 and S_2) also increased in complexity, amplitude, and width with temperature. The characteristic dispersive profile of S_3 (circular polarisation), indicative of Faraday rotation, was found to change systematically with temperature and magnetic field. A key result of this work has been both the successful use and validation of the eastablished *ElecSus* which had been developed for modelling these complex processes. Accounting for temperature dependent atomic density, Doppler broadening, and, importantly the effect of neon buffer gas (which contributed pressure broadening and shifts) *ElecSus* predictions presented excellent agreement with our experimental spectra over the range of varying conditions. This study marks the first time that *ElecSus* has been used to model buffer gas polarimetry of the potassium D1 line, and it provides some helpful benchmark data for future theoretical studies and confirms that both the real and imaginary components of the electric susceptibility are thoroughly accounted for in the model. The results produced in this chapter represented a significant advancement in our understanding of atom-light interactions when using buffer gases. This enhanced understanding not only augmenting the predictive ability of theoretical approaches like *ElecSus* when dealing with complex alkali vapour systems but also has implications for other areas of alkali vapour applications, particularly precision magnetometry and advanced optical filters.

Future work can broaden the scope of this study to a larger range of neon pressures and temperatures, explore the influence on the potassium D2 line, or also look into the effect of other noble buffer gases to build a complete picture of collisional interactions. One can pursue further development of the theoretical model to intrinsically account for more complicated collisional dynamics which may lead to greater predictive capacity of advanced quantum technologies.

Bibliography

[1]   S. A. Alqarni, J. D. Briscoe, C. R. Higgins, F. D. Logue, D. Pizzey, T. G. Robertson-Brown, and I. G. Hughes. A device for magnetic-field angle control in magneto-optical filters using a solenoid-permanent magnet pair. Review of Scientific Instruments, 95(3), 2024.

[2]   S. A. Alqarni, D. Pizzey, S. A. Wrathmall, and I. F. Hughes. The role of buffer gas in shaping the d1 line spectrum of potassium vapour. Journal of Physics B: Atomic, Molecular and Optical Physics, 58, 2025.

[3]   S. A.Alqarni, D. Pizzey, S. A. Wrathmal, and I. G. Hughes. Experimental and theoretical characterisation of stokes polarimetry of the potassium d1 line with neon buffer gas broadening. arXiv preprint arXiv:2507.18353, 2025.

[4]   D. Pizzey, J. D. Briscoe, F. D. Logue, F. S. P. Ojeda, S. A. Wrathmall, and I. G. Hughes. Laser spectroscopy of hot atomic vapours: from'scope to theoretical fit. New Journal of Physics, 2022.

[5]   M. Fleischhauer, A. Imamoglu, and J. P. Marangos. Electromagnetically induced transparency: Optics in coherent media. Reviews of Modern Physics, 77(2):633, 2005.

[6]   Y. Wang, S. Zhang, D. Wang, Z. Tao, Y. Hong, and J. Chen. Nonlinear optical filter with ultranarrow bandwidth approaching the natural linewidth. Optics letters, 37(19):4059–4061, 2012.

[7]   Q. Glorieux, T. Aladjidi, P. D. Lett, and R. Kaiser. Hot atomic vapors for nonlinear and quantum optics. New Journal of Physics, 25(5):051201, 2023.

[8]   B. Julsgaard, J. Sherson, J. I. Cirac, Jaromír Fiurášek, and Eugene S Polzik. Experimental demonstration of quantum memory for light. Nature, 432(7016):482–486, 2004.

[9]   K. F. Reim, P. Michelberger, K. C. Lee, J. Nunn, N. K. Langford, and I. A. Walmsley. Single-Photon-Level Quantum Memory at Room Temperature. Physical Review Letters, 107(5):053603, Jul 2011.

[10]   G. Walker, A. Arnold, and S. Franke-Arnold. Trans-spectral orbital angular momentum transfer via four-wave mixing in rb vapor. Physical review letters, 108(24):243601, 2012.

[11]   R. F. Offer, A. Daffurn, E. Riis, P. F. Griffin, A. S. Arnold, and S. Franke-Arnold. Gouy phase-matched angular and radial mode conversion in four-wave mixing. Physical Review A, 103(2):L021502, 2021.

[12]   A. Vernier, S. Franke-Arnold, E. Riis, and A. Arnold. Enhanced frequency up-conversion in rb vapor. Optics Express, 18(16):17020–17026, 2010.

[13]   M. Harris, C. Adams, S. Cornish, I. McLeod, E. Tarleton, and I. Hughes. Polarization spectroscopy in rubidium and cesium. Physical Review A—Atomic, Molecular, and Optical Physics, 73(6):062509, 2006.

[14]   P. Burdekin, S. Grandi, R. Newbold, R. A. Hoggarth, K. D. Major, and A. S. Clark. Single-photon-level sub-doppler pump-probe spectroscopy of rubidium. Physical Review Applied, 14(4):044046, 2020.

[15] D. Budker and M. Romalis. Optical magnetometry. Nature physics, 3(4):227–234, 2007.

[16] M. Auzinsh, A. Sargsyan, A. Tonoyan, C. Leroy, R. Momier, D. Sarkisyan, and A. Papoyan. Wide range linear magnetometer based on a sub-microsized k vapor cell. Applied optics, 61(19):5749–5754, 2022.

[17] L. A. Downes, A. R. MacKellar, D. J. Whiting, C. Bourgenot, C. S. Adams, and K. J. Weatherill. Full-field terahertz imaging at kilohertz frame rates using atomic vapor. Physical Review X, 10(1):011027, 2020.

[18] I. Gerhardt. How anomalous is my faraday filter? Optics letters, 43(21):5295–5298, 2018.

[19] R. Erdélyi, M. B. Korsós, X. Huang, Y. Yang, D. Pizzey, S. A. Wrathmall, I. G. Hughes, M. J. Dyer, V. S. Dhillon, B. Belucz, et al. The solar activity monitor network–samnet, 2022.

[20] R. Dicke. The effect of collisions upon the doppler width of spectral lines. Physical Review, 89(2):472, 1953.

[21] N. Allard and J. Kielkopf. The effect of neutral nonresonant collisions on atomic spectral lines. Reviews of modern physics, 54(4):1103, 1982.

[22] B. Olsen, B. Patton, Y. Jau, and W. Happer. Optical pumping and spectroscopy of cs vapor at high magnetic field. Physical Review A—Atomic, Molecular, and Optical Physics, 84(6):063410, 2011.

[23] M. Erhard and H. Helm. Buffer-gas effects on dark resonances: Theory and experiment. Physical Review A, 63(4):043813, 2001.

[24] B. E. Sherlock and I. G. Hughes. How weak is a weak probe in laser spectroscopy? American Journal of Physics, 77(2):111–115, 2009.

[25] S. Seltzer and M. Romalis. High-temperature alkali vapor cells with antirelaxation surface coatings. Journal of Applied Physics, 106(11), 2009.

[26] M. D. Rotondaro and G. P. Perram. Collisional broadening and shift of the rubidium d1 and d2 lines (52s12→ 52p12, 52p32) by rare gases, h2, d2, n2, ch4 and cf4. Journal of Quantitative Spectroscopy and Radiative Transfer, 57(4):497–507, 1997.

[27] L. Weller. Absolute Absorption and Dispersion in a Thermal Rb Vapour at High Densities and High Magnetic Fields. PhD thesis, Durham University, 2013.

[28] M. A. Zentile, D. J. Whiting, J. Keaveney, C. S. Adams, and I. G. Hughes. Atomic faraday filter with equivalent noise bandwidth less than 1 ghz. Optics Letters, 40(9):2000–2003, 2015.

[29] D. Whiting et al. Nonlinear optics in a thermal Rb vapour at high magnetic fields. PhD thesis, Durham University, 2017.

[30] L. Weller, K. S. Kleinbach, M. A. Zentile, S. Knappe, C. S. Adams, and I. G. Hughes. Absolute absorption and dispersion of a rubidium vapour in the hyperfine Paschen-Back regime. Journal of Physics B: Atomic, Molecular and Optical Physics, 45(21):215005, oct 2012.

[31] M. A. Zentile, J. Keaveney, L. Weller, D. J. Whiting, C. S. Adams, and I. G. Hughes. ElecSus: A program to calculate the electric susceptibility of an atomic ensemble. Comput. Phys. Commun., 189:162–174, apr 2015.

[32] C. Higgins. Quantum optics with 87Rb vapour in the hyperfine Paschen-Back regime. PhD thesis, Durham University, 2023.

[33] L. Weller, K. Kleinbach, M. A. Zentile, S. Knappe, I. Hughes, and C. Adams. Optical isolator using an atomic vapor in the hyperfine paschen–back regime. Optics letters, 37(16):3405–3407, 2012.

[34] M. A. Zentile, D. J. Whiting, J. Keaveney, C. S. Adams, and I. G. Hughes. Atomic Faraday filter with equivalent noise bandwidth less than 1 GHz. Optics Letters, 40(9):2000, 2015.

[35] J. Keaveney, W. J. Hamlyn, C. S. Adams, and I. G. Hughes. A single-mode external cavity diode laser using an intra-cavity atomic faraday filter with short-term linewidth< 400 khz and long-term stability of< 1 mhz. <u>Review of Scientific Instruments</u>, 87(9), 2016.

[36] I. I. Sobelman. <u>Atomic Spectra and Radiative Transitions</u>, volume 12. Springer Science & Business Media, 2012.

[37] F. S. Ponciano-Ojeda, F. D. Logue, and I. G. Hughes. Absorption spectroscopy and Stokes polarimetry in a ^{87}Rb vapour in the Voigt geometry with a 1.5 T external magnetic field. <u>Journal of Physics B: Atomic, Molecular and Optical Physics</u>, 54(1):015401, 2020.

[38] L. Weller, K. S. Kleinbach, M. A. Zentile, S. Knappe, C. S. Adams, and I. G. Hughes. Absolute absorption and dispersion of a rubidium vapour in the hyperfine Paschen–Back regime. <u>Journal of Physics B: Atomic, Molecular and Optical Physics</u>, 45(21):215005, Oct 2012.

[39] A. Sargsyan, G. Hakhumyan, C. Leroy, Y. Pashayan-Leroy, A. Papoyan, D. Sarkisyan, and M. Auzinsh. Hyperfine paschen–back regime in alkali metal atoms: consistency of two theoretical considerations and experiment. <u>JOSA B</u>, 31(5):1046–1053, 2014.

[40] M. Faraday. I. Experimental researches in electricity.—Nineteenth series. <u>Philosophical Transactions of the Royal Society of London</u>, (136):1–20, 1846.

[41] I. Caltzidis, Harald Kübler, Tilman Pfau, Robert Löw, and Mark A Zentile. Atomic faraday beam splitter for light generated from pump-degenerate four-wave mixing in a hollow-core photonic crystal fiber. <u>Physical Review A</u>, 103(4):043501, 2021.

[42] C. R. Higgins and I. G. Hughes. Electromagnetically induced transparency in a v-system with 87rb vapour in the hyperfine paschen-back regime. <u>Journal of Physics B: Atomic, Molecular and Optical Physics</u>, 54(16):165403, 2021.

[43] J. D. Siverns, J. Hannegan, and Q. Quraishi. Demonstration of slow light in rubidium vapor using single photons from a trapped ion. Science Advances, 5(10):eaav4651, 2019.

[44] D. Budker, W. Gawlik, D. Kimball, S. Rochester, V. Yashchuk, and A. Weis. Resonant nonlinear magneto-optical effects in atoms. Reviews of modern physics, 74(4):1153, 2002.

[45] J. Kitching. Chip-scale atomic devices. Applied Physics Reviews, 5(3), 2018.

[46] W. Nagourney. Quantum electronics for atomic physics and telecommunication. OUP Oxford, 2014.

[47] L. Aplet and J. W. Carson. A faraday effect optical isolator. Applied Optics, 3(4):544–545, 1964.

[48] S. L. Kemp, I. G. Hughes, and S. L. Cornish. An analytical model of off-resonant faraday rotation in hot alkali metal vapours. Journal of Physics B: Atomic, Molecular and Optical Physics, 44(23):235004, 2011.

[49] W. Kiefer, Robert Löw, Jörg Wrachtrup, and Ilja Gerhardt. Na-faraday rotation filtering: the optimal point. Scientific reports, 4(1):6552, 2014.

[50] S. J. Hale, R. Howe, W. J. Chaplin, G. R. Davies, and Y. P. Elsworth. Performance of the birmingham solar-oscillations network (bison). Solar Physics, 291:1–28, 2016.

[51] S. J. Hale, W. J. Chaplin, G. R. Davies, and Y. P. Elsworth. Modelling the response of potassium vapour in resonance scattering spectroscopy. Journal of Physics B: Atomic, Molecular and Optical Physics, 53(8):085003, 2020.

[52] R. Speziali, A. Di Paola, M. Centrone, M. Oliviero, D. B. Calia, L. Dal Sasso, M. Faccini, V. Mauriello, and L. Terranegra. The first light of the solar activity mof monitor telescope (samm). J. Space Weather Space Clim., 11:22, 2021.

[53] R. Forte, F. Berrilli, D. Calchetti, D. Del Moro, B. Fleck, C. Giebink, W. Giebink, L. Giovannelli, S. M. Jefferies, A. Knox, M. Magrì, N. Murphy, G. Nitta, M. Oliviero, E. Pietropaolo, W. Rodgers, S. Scardigli, and G. Viavattene. Data reduction pipeline for mof-based synoptic telescopes. J. Space Weather Space Clim., 10:63, 2020.

[54] L. Giovannelli, F. Berrilli, D. Calchetti, D. Del Moro, G. Viavattene, E. Pietropaolo, M. Iarlori, V. Rizi, S. M. Jefferies, M. Oliviero, et al. The tor vergata synoptic solar telescope (tsst): A robotic, compact facility for solar full disk imaging. Journal of Space Weather and Space Climate, 10:58, 2020.

[55] B. Gelly. Detection of solar eigenmodes. In The Sun's Surface and Subsurface: Investigating Shape and Irradiance, pages 68–105. Springer, 2003.

[56] J. Keaveney, S. A. Wrathmall, C. S. Adams, and I. G. Hughes. Optimized ultra-narrow atomic bandpass filters via magneto-optic rotation in an unconstrained geometry. Optics Letters, 43(17), Sep 2018.

[57] M. A. Zentile, J. Keaveney, R. S. Mathew, D. J. Whiting, C. S. Adams, and I. G. Hughes. Optimization of atomic faraday filters in the presence of homogeneous line broadening. Journal of Physics B: Atomic, Molecular and Optical Physics, 48(18):185001, aug 2015.

[58] P Kusch, S Millman, and II Rabi. The nuclear magnetic moments of n 14, na 23, k 39 and cs 133. Physical Review, 55(12):1176, 1939.

[59] J. H. Manley. The nuclear spin and magnetic moment of potassium (41). Phys. Rev., 49:921, 1936.

[60] C. H. Wu, I. Santiago, J. W. Park, P. Ahmadi, and M. W. Zwierlein. Strongly interacting isotopic bose-fermi mixture immersed in a fermi sea. Physical Review AŽ014Atomic, Molecular, and Optical Physics, 84(1):011601, 2011.

[61] A. Bruner, A. Arie, M. A. Arbore, and M. M. Fejer. Frequency stabilization of a diode laser at 1540 nm by locking to sub-doppler lines of potassium at 770 nm. Applied optics, 37(6):1049–1052, 1998.

[62] R. K. Hanley, P. D. Gregory, I. G. Hughes, and S. L. Cornish. Absolute absorption on the potassium d lines: theory and experiment. Journal of Physics B: Atomic, Molecular and Optical Physics, 48(19):195004, 2015.

[63] U. Gustafsson, J. Alnis, and S. Svanberg. Atomic spectroscopy with violet laser diodes. American Journal of Physics, 68(7):660–664, 2000.

[64] C. J. Foot. Atomic physics. Oxford Master Series in Physics, 7, 2005.

[65] K. Blum. Density matrix theory and applications, volume 64. Springer Series on Atomic, Optical, and Plasma Physics. Spring Berlin Heidelberg, , 3rd edition. [Cited on pages 10 and 11], 2012.

[66] B. H. Bransden and C. J. Joachain. Physics of atoms and molecules. Pearson Education, 2006.

[67] D. J. Whiting. Nonlinear Optics in a Thermal Rb Vapour at High Magnetic Fields. PhD thesis, Durham University, 2017.

[68] R. Loudon. The quantum theory of light. Oxford University Press, Oxford. [Cited on pages 13, 15, 94, 116, and 117], 2000.

[69] F. E. Becerra, R. T. Willis, S. L. Rolston, H. J. Carmichael, and L. A. Orozco. Nondegenerate four-wave mixing in rubidium vapor: Transient regime. Physical Review A—Atomic, Molecular, and Optical Physics, 82(4):043833, 2010.

[70] D. A. Steck. Rubidium 87 d line data. Rubidium 87 D line data. available online at http://steck.us//alkalidata, 2024.

[71] T. Tiecke. Properties of potassium. University of Amsterdam, The Netherlands, Thesis, pages 12–14, 2010.

[72] P. Siddons, C. S. Adams, and I. G. Hughes. Off-resonance absorption and dispersion in vapours of hot alkali-metal atoms. Journal of Physics B: Atomic, Molecular and Optical Physics, 42(17):175004, 2009.

[73] L. Weller, R. J. Bettles, P. Siddons, C. S. Adams, and I. G. Hughes. Absolute absorption on the rubidium d1 line including resonant dipole–dipole interactions. Journal of Physics B: Atomic, Molecular and Optical Physics, 44(19):195006, 2011.

[74] M. Fleischhauer, A. B. Matsko, and M. O. Scully. Quantum limit of optical magnetometry in the presence of ac stark shifts. Physical Review A, 62:013808, 2000.

[75] D. Budker and M. Romalis. Optical magnetometry. Nature Physics, 3(4):227–234, Apr 2007.

[76] J. Keaveney, C. S. Adams, and I. G. Hughes. Elecsus: Extension to arbitrary geometry magneto-optics. Computer Physics Communications, 224:311–324, 2018.

[77] F. D. Logue, J. D. Briscoe, D. Pizzey, S. A. Wrathmall, and I. G. Hughes. Better magneto-optical filters with cascaded vapor cells. Optics Letters, 47(12):2975–2978, 2022.

[78] J. D. Briscoe, D. Pizzey, S. A. Wrathmall, and I. F. Hughes. Indirect measurement of atomic magneto-optical rotation via hilbert transform. Journal of Physics B: Atomic, Molecular and Optical Physics, 57(17):175401, 2024.

[79] N. D. Zameroski, G. D. Hager, W. Rudolph, C. J. Erickson, and D. A. Hostutler. Pressure broadening and collisional shift of the rb d2 absorption line by ch4, c2h6, c3h8, n-c4h10, and he. Journal of Quantitative Spectroscopy and Radiative Transfer, 112(1):59–67, 2011.

[80] G. A. Pitz, A. J. Sandoval, N. D. Zameroski, W. L. Klennert, and D. A. Hostutler. Pressure broadening and shift of the potassium d1 transition by the

noble gases and n2, h2, hd, d2, ch4, c2h6, c3h8, and n-c4h10 with comparison to other alkali rates. Journal of Quantitative Spectroscopy and Radiative Transfer, 113(5):387–395, 2012.

[81] R. Li, Y. Li, L. Jiang, W. Quan, M. Ding, and J. Fang. Pressure broadening and shift of kd 1 and d 2 lines in the presence of 3 he and 21 ne. The European Physical Journal D, 70:1–7, 2016.

[82] G. A. Pitz, A. J. Sandoval, T. B. Tafoya, W. L. Klennert, and D. A. Hostutler. Pressure broadening and shift of the rubidium d1 transition and potassium d2 transitions by various gases with comparison to other alkali rates. Journal of Quantitative Spectroscopy and Radiative Transfer, 140:18–29, 2014.

[83] G. A. Pitz, D. E. Wertepny, and G. P. Perram. Pressure broadening and shift of the cesium d 1 transition by the noble gases and n_2, h_2, hd, d_2, ch_4, c_2h_6, cf_4, and h_3e. Physical Review A, 80(6):062718, 2009.

[84] C. Alcock, V. Itkin, and M. Horrigan. Vapour pressure equations for the metallic elements: 298–2500k. Canadian Metallurgical Quarterly, 23(3):309–313, 1984.

[85] H. Noh and H. Seb Moon. Four-wave mixing in a ladder configuration of warm 87rb atoms: a theoretical study. Optics Express, 29(5):6495–6508, 2021.

[86] G. K. Woodgate. Elementary Atomic Structure. Oxford University Press, 1980.

[87] C. R. Higgins, D. Pizzey, and I. G. Hughes. Fine-structure changing collisions in 87rb upon d2 excitation in the hyperfine paschen-back regime. Journal of Physics B: Atomic, Molecular and Optical Physics, 57(23):235002, 2024.

[88] A. Sargsyan, E. Klinger, A. Tonoyan, C. Leroy, and D. Sarkisyan. Hyperfine paschen–back regime of potassium d2 line observed by doppler-free spec-

troscopy. Journal of Physics B: Atomic, Molecular and Optical Physics, 51(14):145001, 2018.

[89] G. G. Stokes. On the composition and resolution of streams of polarized light from different sources. Transactions of the Cambridge Philosophical Society, 9:399, 1851.

[90] B. Schaefer, E. Collett, R. Smyth, D. Barrett, and B. Fraher. Measuring the stokes polarization parameters. American Journal of Physics, 75(2):163–168, 2007.

[91] J. Keaveney, D. A. Rimmer, and I. G. Hughes. Self-similarity of optical rotation trajectories around the poincare sphere with application to an ultra-narrow atomic bandpass filter. arXiv preprint arXiv:1807.04652, 2018.

[92] D. Pizzey. Tunable homogeneous kg magnetic field production using permanent magnets. Review of Scientific Instruments, 92(12):123002, 2021.

[93] M. Harris, S. Cornish, A. Tripathi, and I. Hughes. Optimization of sub-doppler davll on the rubidium d2 line. Journal of Physics B: Atomic, Molecular and Optical Physics, 41(8):085401, 2008.

[94] P. Siddons, C. S. Adams, C. Ge, and I. G. Hughes. Absolute absorption on rubidium D lines: comparison between theory and experiment. J. Phys. B, 41(15):155004, aug 2008.

[95] K. B. MacAdam, A. Steinbach, and C. Wieman. A narrow-band tunable diode laser system with grating feedback, and a saturated absorption spectrometer for cs and rb. American Journal of Physics, 60(12):1098–1111, 1992.

[96] L. Weller, T. Dalton, P. Siddons, C. S. Adams, and I. G. Hughes. Measuring the Stokes parameters for light transmitted by a high-density rubidium vapour in large magnetic fields. Journal of Physics B: Atomic, Molecular and Optical Physics, 45(5):055001, feb 2012.

[97] D. Dick and T. M. Shay. Ultrahigh-noise rejection optical filter. Optics letters, 16(11):867–869, 1991.

[98] H. Chen, C. She, P. Searcy, and E. Korevaar. Sodium-vapor dispersive faraday filter. Optics letters, 18(12):1019–1021, 1993.

[99] P. Yeh. Dispersive magnetooptic filters. Applied optics, 21(11):2069–2075, 1982.

[100] J. A. Zielińska, F. A. Beduini, N. Godbout, and M. W. Mitchell. Ultranarrow faraday rotation filter at the rb d 1 line. Optics letters, 37(4):524–526, 2012.

[101] I. Gerhardt. How anomalous is my faraday filter? Optics Letters, 43(21):5295–5298, Nov 2018.

[102] Y. Ohman. On Some New Auxilliary Instruments In Astrophysical Research. Stock. Obs. Ann., 19(4):3, 1956.

[103] M. Cimino, A. Cacciani, and N. Sopranzi. An Instrument to measure Solar Magnetic Fields by an Atomic-Beam Method. Solar Physics, 3(4):618–622, April 1968.

[104] A. Cacciani and M. Fofi. The magneto-optical filter. Sol. Phys., 59(1):179–189, sep 1978.

[105] A. Cacciani, D. Ricci, P. Rosati, E. Rhodes, E. Smith, S. Tomczyk, and R. Ulrich. Solar magnetic fields measurements with a magneto-optical filter. Il Nuovo Cimento C, 13:125–130, 1990.

[106] R. Erdelyi, M. B. Korsos, X. Huang, Y. Yang, D. Pizzey, S. A. Wrathmall, I. Hughes, and et al. The solar activity monitor network - samnet. Journal of Space Weather and Space Climate, June 2021. © 2021 The author(s). This is an author-produced version of a paper subsequently published in Journal of Space Weather and Space Climate. Uploaded in accordance with the publisher's self-archiving policy.

[107] C. Fricke-Begemann, M. Alpers, and J. Höffner. Daylight rejection with a new receiver for potassium resonance temperature lidars. Opt. Lett., 27(21):1932–1934, Nov 2002.

[108] A. Popescu, K. Schorstein, and T. Walther. A novel approach to a Brillouin–LIDAR for remote sensing of the ocean temperature. Applied Physics B, 79(8):955–961, Dec 2004.

[109] Y. Yang, X. Cheng, F. Li, X. Hu, X. Lin, and S. Gong. A flat spectral faraday filter for sodium lidar. Optics Letters, 36(7):1302, apr 2011.

[110] L. Yin, D. Qian, Z. Geng, H. Zhan, and G. Wu. Using fadof to eliminate the background light influence in ghost imaging. Optics Express, 30(20):36297–36306, 2022.

[111] S. D. Harrell, C. She, T. Yuan, D. A. Krueger, H. Chen, S. Chen, and Z. Hu. Sodium and potassium vapor faraday filters revisited: theory and applications. JOSA B, 26(4):659–670, 2009.

[112] F. Schuller, M. J. D. Macpherson, D. N. Stacey, R. B. Warrington, and K. P. Zetie. The Voigt effect in a dilute atomic vapour. Optics Communications, 86(2):123–127, 1991.

[113] M. W. Kudenov, B. Pantalone, and R. Yang. Dual-beam potassium voigt filter for atomic line imaging. Applied Optics, 59(17):5282–5289, 2020.

[114] J. Menders, P. Searcy, K. Roff, and E. Korevaar. Blue cesium faraday and voigt magneto-optic atomic line filters. Optics Letters, 17(19):1388–1390, 1992.

[115] L. Yin, B. Luo, J. Xiong, and H. Guo. Tunable rubidium excited state voigt atomic optical filter. Optics Express, 24(6):6088–6093, 2016.

[116] J. Keaveney, F. S. Ponciano-Ojeda, S. M. Rieche, M. J. Raine, D. P. Hampshire, and I. G. Hughes. Quantitative optical spectroscopy of 87rb vapour in

the voigt geometry in dc magnetic fields up to 0.4 t. *Journal of Physics B: Atomic, Molecular and Optical Physics*, 52(5):055003, 2019.

[117] T. Pyragius, H. M. Florez, and T. Fernholz. Voigt-effect-based three-dimensional vector magnetometer. *Physical Review A*, 100(2):023416, Aug 2019.

[118] K. Muroo, T. Matsunobe, Y. Shishido, Y. Tukubo, and M. Yamamoto. Resonant Voigt-effect spectrum of the rubidium D_2 transition. *Journal of the Optical Society of America B*, 11(3):409–414, 1994.

[119] J. D. Briscoe, F. D. Logue, D. Pizzey, S. A. Wrathmall, and I. G. Hughes. Voigt transmission windows in optically thick atomic vapours: a method to create single-peaked line centre filters. *Journal of Physics B: Atomic, Molecular and Optical Physics*, 56(10):105403, 2023.

[120] N. H. Edwards, S. J. Phipp, and P. E. G. Baird. Magneto-optic rotation for an arbitrary field direction. *Journal of Physics B: Atomic, Molecular and Optical Physics*, 28(18):4041, 1995.

[121] G. Nienhuis and F. Schuller. Magneto-optical effects of saturating light for arbitrary field direction. *Optics Communications*, 151(1-3):40–45, May 1998.

[122] M. D. Rotondaro, B. V. Zhdanov, and R. J. Knize. Generalized treatment of magneto-optical transmission filters. *Journal of the Optical Society of America B*, 32(12):2507, Dec 2015.

[123] F. Logue. *Improving Magneto-Optical Filter Performance: Cascading and Oblique B-fields*. PhD thesis, Durham University, 2023.

[124] C. R. Higgins, D. Pizzey, R. S. Mathew, and I. G. Hughes. Atomic line versus lens cavity filters: a comparison of their merits. *OSA Continuum*, 3(4):961–970, Apr 2020.

[125] M. Ortner and L. G. C. Bandeira. Magpylib: A free python package for magnetic field computation. SoftwareX, 11:100466, 2020.

[126] J. Keaveney. Collective atom–light interactions in dense atomic vapours. Springer, 2014.

[127] I. Hughes and T. Hase. Measurements and their uncertainties: a practical guide to modern error analysis. OUP Oxford, 2010.

[128] E. V. Raevsky and V. L. Pavlovitch. Stabilizing the output of a pockels cell q-switched nd: Yag laser. Optical Engineering, 38(11):1781–1784, 1999.

[129] H. Jelínková, J. Šulc, P. Koranda, M. Němec, M. Čech, M. Jelínek, and V. Škoda. Linbo3 pockels cell for q-switch of er: Yag laser. Laser Physics Letters, 1(2):59, 2004.

[130] Ch. Ottinger, R. Scheps, G. W. York, and A. Gallagher. Broadening of the rb resonance lines by the noble gases. Physical Review A, 11(6):1815, 1975.

[131] M. V. Romalis, E. Miron, and G. D. Cates. Pressure broadening of rb d 1 and d 2 lines by 3 he, 4 he, n 2, and xe: Line cores and near wings. Physical Review A, 56(6):4569, 1997.

[132] N. Lwin and D. G. McCartan. Collision broadening of the potassium resonance lines by noble gases. Journal of Physics B: Atomic and Molecular Physics, 11(22):3841, 1978.

[133] E. L. Lewis. Collisional relaxation of atomic excited states, line broadening and interatomic interactions. Physics Reports, 58(1):1–71, 1980.

[134] C. S. Adams and I. G. Hughes. Optics f2f: from Fourier to Fresnel. Oxford University Press, 2018.

[135] T. Schwartz, P. M. Finch, C. L. Strand, R. K. Hanson, Y. Luo, W. M. Yu, J. M. Austin, and H. G. Hornung. Laser absorption sensor targeting

potassium for hypersonic velocity, temperature, and enthalpy measurements. AIAA Journal, 61(8):3287–3297, 2023.

[136] Y. Zhang, X. Jia, Z. Ma, and Q. Wang. Potassium Faraday optical filter in line-center operation. Optics Communications, 194(1):147–150, Jul 2001.

[137] H. Jöffner and C. Fricke-Begemann. Accurate lidar temperatures with narrowband filters. Optics Letters, 30(8):890–892, Apr 2005.

[138] K. M W, P. B, and Y. R. Dual-beam potassium Voigt filter for atomic line imaging. Applied Optics, 59(17):5282–5289, Jun 2020.

[139] E. Kroemer, M. Abdel Hafiz, V. Maurice, B. Fouilland, C. Gorecki, and R. Boudot. Cs vapor microcells with Ne-He buffer gas mixture for high operation-temperature miniature atomic clocks. Opt. Express, 23(14):18373–18380, Jul 2015.

[140] D. Pizzey I. G. Hughes S. Svensson, C. R. Higgins and S. Franke-Arnold. Visualizing strongly focused 3D light fields in an atomic vapor. arXiv preprint arXiv:2506.01680, 2025.

[141] A. López Ariste. Hanle and zeeman effects: from solar to stellar diagnostics. In P. Petit, M. Jardine, and H. Spruit, editors, Magnetic Fields throughout Stellar Evolution, Proceedings of the IAU Symposium No. 302. International Astronomical Union, 2013.

[142] E. Landi Degl'Innocenti and M. Landolfi. Polarization in Spectral Lines. Springer Nature Link, 2004.

[143] F. S. Ponciano-Ojeda, F. D. Logue, and I. G. Hughes. Absorption spectroscopy and stokes polarimetry in a 87rb vapour in the voigt geometry with a 1.5 t external magnetic field. Journal of Physics B: Atomic, Molecular and Optical Physics, 54(1):015401, 2020.

[144] C. S. Adams and I. G. Hughes. Optics f2f - From Fourier to Fresnel. Oxford University Press, Oxford, UK, 2019.

[145] P. Siddons, N. C. Bell, Y. Cai, C. S. Adams, and I. G. Hughes. A gigahertz-bandwidth atomic probe based on the slow-light faraday effect. Nature Photonics, 3(4):225–229, 2009.

[146] M. Mäusezahl, F. Munkes, and R. Löw. Tutorial on laser locking techniques and the manufacturing of vapor cells for spectroscopy. New Journal of Physics, 26(10):105002, 2024.

[147] H. Krelman, O. Nefesh, K. Levi, D. G. Bopp, S. Kang, J. E. Kitching, and L. Sternro. Laser offset stabilization with chip-scale atomic diffractive elements. Physical Review Applied, 23(3):034011, 2025.

[148] B. Chéron, H. Gilles, J. Hamel, O. Moreau, and H. Sorel. Laser frequency stabilization using zeeman effect. Journal de Physique III, 4(2):401–406, 1994.

[149] Anna L Marchant, Sylvi Händel, Timothy P Wiles, Stephen A Hopkins, Charles S Adams, and Simon L Cornish. Off-resonance laser frequency stabilization using the faraday effect. Optics letters, 36(1):64–66, 2010.

[150] M. A. Zentile, R. Andrews, L. Weller, S. Knappe, C. S. Adams, and I. G. Hughes. The hyperfine Paschen–Back Faraday effect. Journal of Physics B: Atomic, Molecular and Optical Physics, 47(7):075005, mar 2014.

[151] R. Marsland, B. H. McGuyer, B. A. Olsen, and W Happer. Spin-velocity correlations of optically pumped atoms. Phys. Rev. A, 86:023404, 2012.

[152] M. Kelley et al. Theoretical models of spin-exchange optical pumping. Journal of Applied Physics, 129(15):154901, 2021.

Colophon